Progress in NMR Spectroscopy, Vol. 23, pp. 43–92, 1991.
Printed in Great Britain.

0079–6565/91 $0.00+.50

APPLICATIONS OF THREE- AND FOUR-DIMENSIONAL HETERONUCLEAR NMR SPECTROSCOPY TO PROTEIN STRUCTURE DETERMINATION

G. MARIUS CLORE and ANGELA M. GRONENBORN

Laboratory of Chemical Physics, Building 2, National Institute of Diabetes and Digestive and Kidney Diseases, National Institutes of Health, Bethesda, MD 20892, U.S.A.

(*Received* 27 *December* 1990)

CONTENTS

ABBREVIATIONS

NMR	Nuclear Magnetic Resonance
NOE	Nuclear Overhauser Effect
NOESY	Nuclear Overhauser Enhancement Spectroscopy
COSY	Correlated Spectroscopy
HOHAHA	Homonuclear Hartmann–Hahn Spectroscopy
TOCSY	Total Correlated Spectroscopy
HMQC	Heteronuclear Multiple Quantum Coherence Spectroscopy
FID	Free Induction Decay

2D	Two-dimensional
3D	Three-dimensional
4D	Four-dimensional
TPPI	Time Proportional Phase Incrementation
rf	radiofrequency

1. INTRODUCTION

The last few years have seen tremendous advances in the NMR methodology for determining protein structures in solution.[1-5] Indeed, it is now possible to obtain structures of small proteins (<100 residues) in solution at an accuracy equivalent to that of a 2.0–2.5 Å resolution crystal structure, with atomic rms distributions about the mean coordinate positions of 0.3–0.4 Å for the backbone atoms and 0.4–0.5 Å for internal side chains.[6] Typically such structures are based on 15–20 NOE interproton distance restraints per residue (calculated by simply dividing the total number of restraints by the number of residues), stereospecific assignments and a large number of ϕ, ψ and χ_1 torsion angle restraints derived from analysis of coupling constant and NOE data in conjunction with conformational grid searches. Examples of high resolution NMR structures solved to date are the C-terminal domain of cellobiohydrolase,[7] the Antennapedia homeodomain,[8] interleukin-8,[9] a zinc finger domain from a human enhancer binding protein[10] and human thioredoxin.[11]

Solving the structures of larger proteins (140–250 residues) presents a formidable challenge.[12] First, the chemical shift overlap and degeneracy, in all but exceptional cases, is so extensive that conventional assignment strategies based on 2D ^{1}H-NMR experiments can no longer be applied successfully. Second, the larger linewidths associated with increasing molecular weight make it difficult to apply ^{1}H correlation experiments that rely on the small homonuclear couplings which are invariably $\leq$12 Hz. These problems are dramatically illustrated in Fig. 1 which shows the amide NH–aliphatic regions of the ^{1}H 2D NOESY and HOHAHA spectra of interleukin-1β (IL-1β), a protein of 153 residues and molecular mass 17.4 kDa, which plays a key role in the immune and inflammatory response. It is clear from these two spectra that while there are some resolved cross peaks, there is also extensive cross peak overlap and chemical shift degeneracy. Indeed, the NOESY spectrum looks almost as if 'someone had spilled ink on it'. Further, the number of relayed connectivities observed in the HOHAHA spectrum is rather limited, thereby complicating the process of spin system assignment.

An obvious solution lies in increasing the resolution of the spectra. In this regard, there are two fundamentally different approaches that can be employed.[13] The conventional approach seeks to improve the 2D NMR spectra by increasing the digital resolution and by using strong resolution enhancement digital filtering functions at the expense of sensitivity. An alternative approach improves resolution by increasing the dimensionality of the spectrum by separating the individual proton resonances according to the chemical shifts of the directly bonded heteronuclei and simultaneously yields important additional information about the system (i.e. ^{15}N and ^{13}C chemical shifts). As this method employs large one-bond heteronuclear couplings for the magnetization transfer steps, it is much less sensitive to wide linewidths associated with larger proteins than any method that relies on small proton couplings. Because the resolution in 3D and 4D spectra is limited by digitization, spectra with equivalent resolution can be recorded at magnetic field strengths significantly lower than 600 MHz (e.g. the resolution quality of 500 MHz multi-dimensional spectra is essentially the same as those recorded at 600 MHz although the signal-to-noise ratio is somewhat better at 600 MHz than at 500 MHz).

The present review focuses on 3D and 4D double and triple resonance heteronuclear NMR experiments, all of which have been developed in the last two years with the aim of extending the application of NMR as a method for determining solution structures of proteins up to 30–40 kDa.

2. BASIC PRINCIPLES OF MULTI-DIMENSIONAL NMR

Any 2D experiment can be reduced to the same basic scheme comprising a preparation pulse, an evolution period (t_1), a mixing period (M), and a detection period (t_2) (Fig. 2).[14] During the evolution

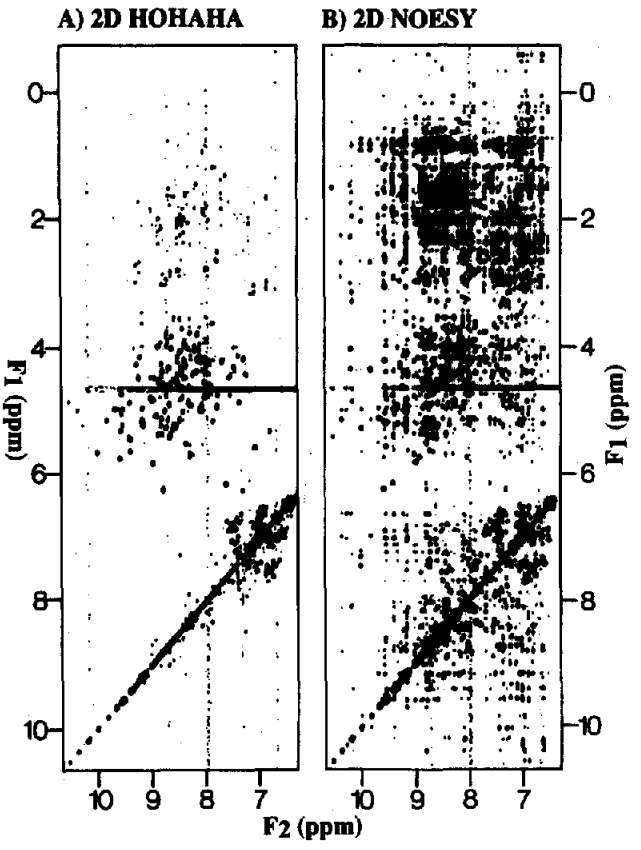

FIG. 1. NH(F_2)–^{1}H(F_1) regions of the 600 MHz 2D ^{1}H–^{1}H HOHAHA and NOESY spectra of IL-1β (1.7 mM) in 90% H_2O/10% D_2O.[12]

2D NMR P_a - $E_a(t_1)$ - M_a - $D_a(t_2)$

3D NMR P_a - $E_a(t_1)$ - M_a - $E_b(t_2)$ - M_b - $D_b(t_3)$

4D NMR P_a - $E_a(t_1)$ - M_a - $E_b(t_2)$ - M_b - $E_c(t_3)$ - M_c - $D_c(t_4)$

FIG. 2. Relationship between the pulse sequences for recording 2D, 3D and 4D NMR spectra. Abbreviations: P, preparation; E, evolution; M, mixing; and D, detection.

period spins are labeled according to their chemical shifts in the indirectly detected dimension, and in the mixing period the spins are correlated with each other. The experiment is repeated several times with successively incremented values of the evolution period t_1 to generate a data matrix $s(t_1, t_2)$. Fourier transformation in the t_2 dimension yields a set of n 1D spectra in which the intensities of the resonances are modulated sinusoidally as a function of the t_1 duration. Subsequent Fourier transformation in the t_1 dimension yields the desired 2D spectrum $S(\omega_1, \omega_2)$.

The relationship between 2D and higher dimensional NMR experiments is shown in Fig. 2. A 3D pulse sequence is simply constructed by combining two 2D sequences, leaving out the detection period of the first experiment and the preparation pulse of the second.[15,16] Similarly, a 4D pulse sequence is made up of three 2D sequences, leaving out the detection periods of the first and second experiments,

and the preparation pulse of the second and third experiments.[13] Thus, in the 3D experiment, two evolution periods are incremented independently to yield a data matrix $s(t_1, t_2, t_3)$, while in the 4D experiment, there are three independently incremented evolution periods and the resulting data matrix has the form $s(t_1, t_2, t_3, t_4)$.

2.1. *Homonuclear 3D NMR*

The first 3D NMR experiments on proteins were of the homonuclear variety in which a HOHAHA sequence was combined with a NOESY one, using either selective[16-18] or non-selective[19,20] pulses. Figure 3 shows an example of the 3D HOHAHA–NOESY spectrum of purothionin in H_2O.[17] This particular spectrum employed a selective pulse centered around the NH and $C^{\alpha}H/C^{\beta}H$ regions in the F_1 and F_2 dimensions, respectively, and cross peaks arise from the pathway

$$\mathrm{NH} \xrightarrow{J+\text{relayed } J} \mathrm{C^{\alpha}H/C^{\beta}H} \xrightarrow{\mathrm{NOE}} \mathrm{NH/aliphatics}.$$

While these homonuclear experiments are conceptually elegant, their applicability to larger proteins is very limited as the efficiency of the scalar correlation step is severely reduced with increasing linewidths. As a result the sensitivity for experiments of this kind drops off rapidly as the molecular weight rises above ~10 kDa. Another difficulty with 3D homonuclear experiments is that they are difficult to analyze as the number of peaks present in the 3D spectrum is much larger than in the corresponding 2D experiments. This is due to the presence of single (A→A→B and A→B→B) and back transfer (A→B→A) peaks which contain no new information, in addition to genuine 3D (A→B→C) peaks.

2.2. *Heteronuclear 3D and 4D NMR*

All the deficiencies of the homonuclear experiments can be overcome by heteronuclear methods using uniformly (>95%) labeled ^{15}N and/or ^{13}C proteins. In these experiments the large resolved

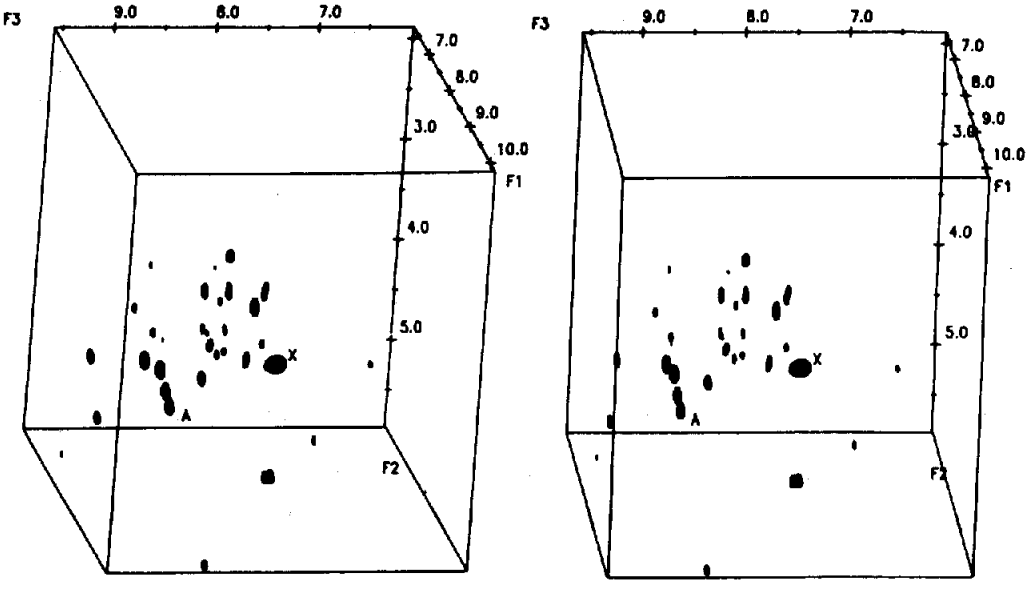

FIG. 3. Stereoview of the $NH(F_1)$–$C^{\alpha}H/C^{\beta}H(F_2)$–$NH(F_3)$ subvolume of the 500 MHz 3D ^1H–^1H HOHAHA–NOESY spectrum of the 45 residue protein α1-purothionin (6.7 mM) in 90% H_2O/10% D_2O.[17] The spectrum was recorded in 55 h.

heteronuclear couplings permit efficient transfer of magnetization through bonds. A further key advantage over homonuclear methods is that the heteronuclear methods allow one to increase the spectral resolution by extending the dimensions without increasing the spectral complexity.[12,13] That is to say the number of cross peaks present in the entire spectrum remains unchanged, irrespective of the dimensionality of the spectrum.

As an example, Fig. 4 illustrates the progression and relationship between $^{15}N/^{13}C$ edited 2D, 3D and 4D NOESY experiments.[13] In the 2D experiment, NOEs between NH protons (in the F_2 dimension) and aliphatic protons (in the F_1 dimension) are observed in a single plane. In the schematic example shown in Fig. 4 there are cross peaks from 11 aliphatic protons to three NH protons at a single NH chemical shift. In the 3D spectrum these NOEs are spread within a 3D cube over a series of $F_3(NH)$–$F_1(^1H)$ planes according to the chemical shift of the directly bonded ^{15}N atoms in the F_2 dimension. In the example shown, these peaks are located in three planes, indicating that these 11 NOEs involve three different NH protons, thus resolving ambiguities associated with NH chemical shift degeneracy. The aliphatic protons involved in these NOE effects, however, are still only identified by their ^1H chemical shifts. As the chemical shift overlap in the aliphatic region is far more extensive than in the NH region of the spectrum, the assignment of the originating aliphatic protons is difficult. These ambiguities can readily be resolved by extending the dimensionality of the experiment to four, introducing the chemical shift of the directly attached ^{13}C nuclei for these aliphatic protons. Thus, each plane at a particular ^{15}N chemical shift in the 3D spectrum constitutes a cube in the 4D spectrum and each cube is subdivided into a further series of planes based on the ^{13}C chemical shift of the ^{13}C atoms directly bonded to the aliphatic protons indicated in F_1. Thus, in the 4D experiment, the identity of the originating aliphatic protons can be established unambiguously on the basis of their ^1H and associated ^{13}C chemical shifts, while the identity of the destination NH protons is provided by the ^1H and associated ^{15}N chemical shifts.

2.3. *The Building Blocks of 3D and 4D Heteronuclear NMR Experiments*

In order to exploit the heteronuclear methods to maximum advantage, indirect detection methods have to be employed. In such pulse sequences, magnetization residing on protons is first transferred to the heteronucleus and then back again so that ^1H magnetization is detected. The gain in sensitivity compared to an experiment which employs X nucleus detection is given by $n(\gamma_H/\gamma_X)^{3/2}$ where γ_H and γ_X are the gyromagnetic ratios of the ^1H and X-nucleus, respectively, and n is the number of protons attached to the X nucleus.[21] For ^{13}C–^1H correlation the gain in sensitivity is 24 for methyl groups, 16 for methylene protons, and 8 for methine protons, while for ^{15}N–^1H correlation of backbone amides it is about 30. The practical consequence is that high quality heteronuclear 3D and 4D experiments can easily be recorded on 1–2 mM samples,of uniformly labeled protein.

In general two types of transfer mechanisms are employed, the first makes use of single quantum INEPT transfer,[22] while the second uses multiple quantum coherence.[23–25]

The INEPT building block is given by

$$\begin{array}{lccccccc} ^1H(I) & 90_x & & \tau & 180_x & \tau & 90_y \\ X(S) & & & & 180_x & & 90_x. \end{array}$$

The simultaneous 180° pulses on the ^1H and X nuclei refocus chemical shifts but not heteronuclear couplings, so that $^1H - I_y$ magnetization is converted into the antiphase term $2I_xS_z$ after a duration $2\tau = 1/(2J_{HX})$. The subsequent pair of 90° pulses transform the $2I_xS_z$ term into $2I_zS_y$ magnetization.

The heteronuclear multiple quantum coherence (HMQC) building block, on the other hand, is given by

$$\begin{array}{lccccc} ^1H(I) & 90_x & & 2\tau & & \\ X(S) & & & & 90_x. & \end{array}$$

As in the INEPT sequence, $-I_y$ magnetization is transformed into $2I_xS_z$ after the period 2τ. However, the single 90° pulse applied to the X nucleus generates the two spin order term $-2I_xS_y$. Subsequent

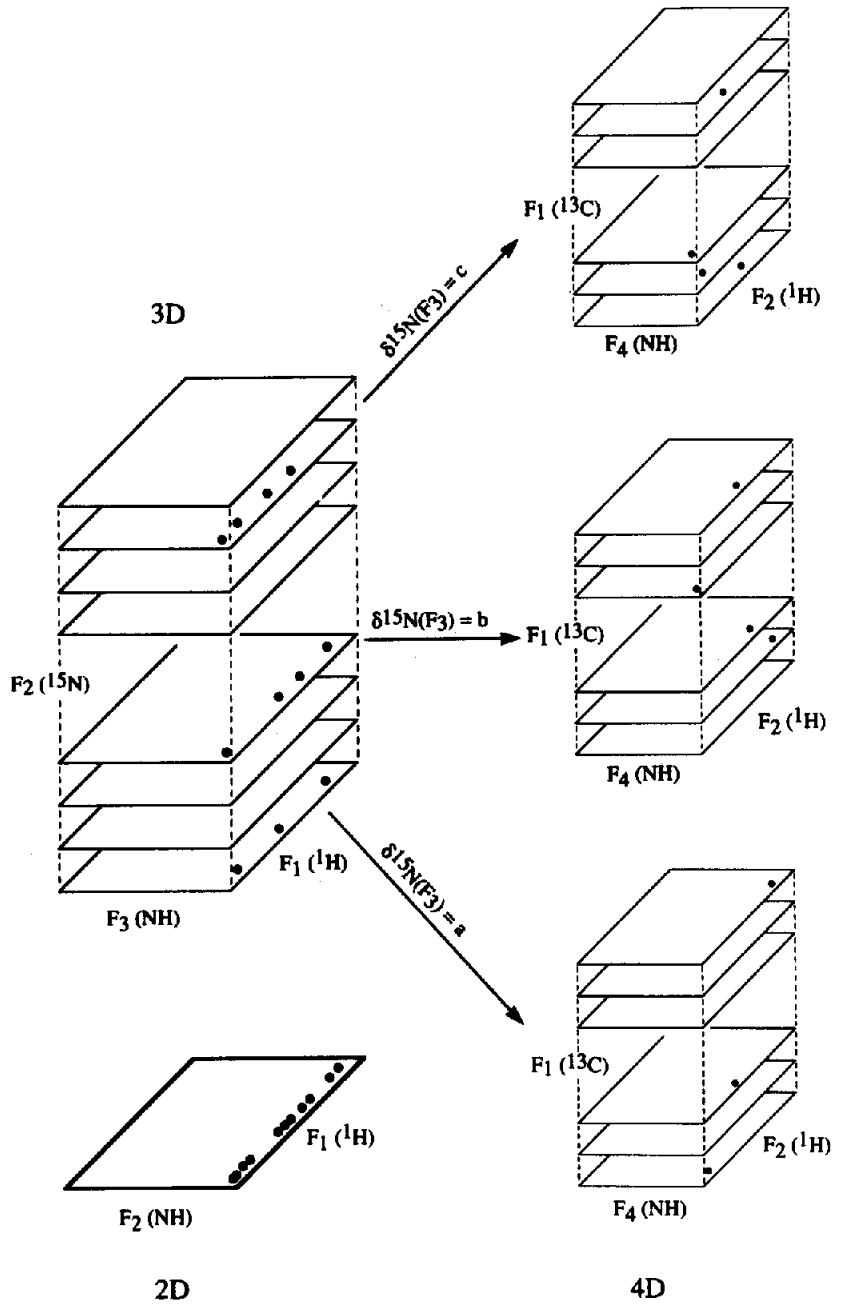

FIG. 4. Schematic illustration of the progression and relationship between heteronuclear $^{13}C/^{15}N$-edited 2D, 3D and 4D NOESY spectra.[13] The closed circles represent NOE cross peaks between NH and aliphatic protons. Typically for 3D experiments we record a data set comprising 32 complex points in the heteronuclear dimension(s), 128 complex points in the indirectly detected ^1H dimension and 512–1024 real points in the ^1H acquisition dimension. For 4D experiments, we typically record 8–16 complex points in the heteronuclear dimensions, 64 complex points in the indirectly detected ^1H dimension and 256–512 real points in the ^1H acquisition dimension. The data are then processed with one zero-filling in all dimensions, and, when appropriate, the time domain data in the severely truncated dimensions can be extended by linear prediction. The heteronuclear 3D experiments typically take 2–3 days to record while the 4D ones take 3–4 days. High quality heteronuclear 3D and 4D spectra can easily be obtained on 1 to 2 mM samples of uniformly (>95%) ^{15}N and/or ^{13}C-labeled protein.

exclusive evolution of the heteronuclear chemical shift can be simply accomplished by placing a ^1H 180° pulse in the middle of the evolution period. Under special circumstances, it is desirable to retain magnetization of protons not attached to the X nucleus along the y axis. This can be achieved by inserting a pair of simultaneous 180°_x pulses on the ^1H and X nucleus in the middle of the interval 2τ. It is then possible to apply a ^1H trim pulse along the x axis to effectively remove all magnetization along the y axis, particularly H_2O magnetization, by randomization, thereby avoiding the necessity for presaturation of the H_2O resonance.

One of the problems associated with pulse schemes incorporating INEPT transfer is the presence of numerous 180° pulses which invariably result in significant sensitivity losses. This can be circumvented by concatenation.[14,26] Consider for example, the pulse scheme

$$\begin{array}{lccccccccc} ^1H(I) & 90_x & t_1/2 & & t_1/2 & \tau & 180_x & \tau & 90_y \\ X(S) & & & 180_x & & & 180_x & & 90_x \end{array}$$

where ^1H chemical shifts evolve during the period t_1 and magnetization is subsequently transferred to the X nucleus by an INEPT sequence. This can be reduced to

$$\begin{array}{lccccccccc} ^1H(I) & 90_x & t_1/2 & \tau & & t_1/2 & 180_x & \tau & 90_y \\ X(S) & & & & 180_x & & & & 90_x \end{array}$$

thereby eliminating one 180° pulse. By expressing this scheme as

$$\begin{array}{lccccccc} ^1H(I) & 90_x & A & & B & 180_x & C & 90_y \\ X(S) & & & 180_x & & & & 90_x \end{array}$$

it is readily appreciated that ^1H chemical shifts evolve during the period $A+B-C=t_1$, while the heteronuclear couplings evolve during the period $A-B+C=2\tau$.[27]

The concatenation of 180° pulses can be generalized to two basic rules. First, a single 180° pulse with a fixed delay τ_I preceding it and a fixed delay τ_{II} following it

$$\tau_I \quad 180 \quad \tau_{II}$$

can often be replaced by a single delay given by

$$(\tau_I - \tau_{II}).$$

Second, any scheme involving two nuclei, which is of the type

$$\begin{array}{lccccccc} I & t_1/2 & & t_1/2 & \tau_I & 180 & \tau_I \\ S & & 180 & & & 180 & \end{array}$$

where ^1H chemical shifts evolve during the evolution period t_1 and ^1H–X couplings evolve during the period $2\tau_I$, can be simplified to a pulse scheme with only two 180° pulses

$$\begin{array}{lccccccc} I & t_1/2 & \tau_I & & t_1/2 & 180 & \tau_I \\ S & & & 180 & & & \end{array}$$

With these two rules in hand, even the most complex combination of 180° pulses can be extensively shortened, by applying these rules in a successive and independent manner. Consider the following set of six 180° pulses in a triple resonance experiment:

$$\begin{array}{lccccccccc} I & & 180 & & & & & & 180 & \\ S & & 180 & & & 180 & & & & \\ N & t_1/2 & & t_1/2 & \tau_I & 180 & \tau_I & \tau_{II} & 180 & \tau_{II}. \end{array}$$

In this sequence the N nucleus chemical shift evolves during the evolution period t_1, the S–N J coupling is focused during the period $2\tau_I$, and the I–N J coupling is defocused during the period $2\tau_{II}$. This can be simplified via three steps, each of which eliminates one 180° pulse, to yield a final pulse

sequence containing only three 180° pulses. In the first step rule 2 is applied to give:

$$\begin{array}{lccccccccc} I & & & 180 & & & & & & \\ S & & & 180 & & & 180 & & & \\ N & t_1/2 & \tau_{II} & & t_1/2 & \tau_I & 180 & \tau_I & 180 & \tau_{II}. \end{array}$$

Rule 2 is applied again in the second step to give

$$\begin{array}{lccccccccc} I & & & 180 & & & & & & \\ S & & & & & 180 & & & & \\ N & t_1/2 & \tau_{II} & & \tau_I & & t_1/2 & 180 & \tau_I & 180 & \tau_{II}. \end{array}$$

Finally, rule 1 is applied in the third step to yield

$$\begin{array}{lccccccc} I & & & 180 & & & & \\ S & & & & & 180 & & \\ N & t_1/2 & \tau_{II} & & (\tau_I-\tau_{II}) & & t_1/2 & 180 \quad \tau_I. \end{array}$$

An alternative approach can also be used by hypothesizing that the six pulse scheme can be reduced to three pulses with delays A, B, C and D.[27]

$$\begin{array}{lccccccc} I & & 180 & & & & & \\ S & & & & & 180 & & \\ N & A & & B & & C & 180 & D \end{array}$$

The N nucleus chemical shift evolves during the time $A+B+C-D=t_1$, the S–N coupling evolves during the time $A+B-C+D=\tau_I$, and the I–N coupling evolves during the period $A-B-C+D=\tau_{II}$. One solution to these equations is simply $A=t_1/2+\tau_{II}$, $B=\tau_I-\tau_{II}$, $C=t_1/2$ and $D=\tau_I$, which is exactly the result found by the reductionist approach outlined above.

2.4. *Some Experimental Considerations for the Implementation of 3D and 4D Experiments*

The following section outlines some experimental considerations that should be borne in mind for the optimal design of 3D and 4D pulse sequences, taking into account the limitations imposed by resolution and measurement time.

2.4.1. *Quadrature Detection in the Indirectly Detected Dimensions.* In general it is advisable to record spectra in the pure phase absorption mode in order to obtain as high a sensitivity and resolution as possible. To achieve this it is necessary to obtain quadrature detection in the indirectly detected dimension which in the case of 2D NMR is the F_1 dimension. Four different methods may be used as summarized in Table 1. For conventional 2D NMR, the time proportional phase incrementation (TPPI) method[28] is probably the most commonly used, and has the advantage that axial peaks are only observed at the edge of the spectrum.[29] The States method[30] however, has the advantage that the carrier position in the F_1 dimension can be shifted after data collection by applying a linear phase correction to the FIDs. Although axial peaks in the States method are observed in the center of the spectrum,[29] this does not present a problem in conventional 2D NMR as usually sufficient scans per increment are recorded to permit appropriate phase cycling for the suppression of axial peaks. In 3D NMR, on the other hand, it is essential to use as few scans per increment as possible to ensure that the measuring time is confined to reasonable limits. Thus, in this case, a hybrid combination of the TPPI and States methods is the most desirable,[29] offering the best of both methods, and is the approach routinely used in our laboratory.

In the case of all the pulse schemes discussed in this review, quadrature detection using the TPPI–States method[29] is achieved by incrementing the phases ψ_i independently by 90° in each dimension t_i to generate complex data. In addition, every time t_i is incremented, the receiver phase and ψ_i are also incremented by 180°.

TABLE 1. Comparison of methods used to obtain quadrature detection in the indirectly detected dimension(s) in multi-dimensional NMR experiments*[29]

Method	Phase of preparation Pulse ψ*	Acquisition receiver phase	Fourier transform	Axial peak
Redfield	$x(t_1)$	x	Real	Center
	$y(t_1+\Delta)$	x		
	$x(t_1+2\Delta)$	−x		
	$y(t_1+3\Delta)$	−x		
TPPI	$x(t_1)$	x	Real	Edge
	$y(t_1+\Delta)$	x		
	$-x(t_1+2\Delta)$	x		
	$-y(t_1+3\Delta)$	x		
States	$x(t_1)$	x	Complex	Center
	$y(t_1)$	x		
	$x(t_1+2\Delta)$	x		
	$y(t_1+2\Delta)$	x		
TPPI–States	$x(t_1)$	x	Complex	Edge
	$y(t_1)$	x		
	$-x(t_1+2\Delta)$	−x		
	$-y(t_1+2\Delta)$	−x		

* The time Δ equals $1/(2SW_1)$, where SW_1 is the spectral width in F_1. For the States and TPPI–States method, the x and y experiments are stored in separate locations to be processed as complex data. The TPPI–States method combines the different advantages of both the States and TPPI methods. Thus, shifting of the carrier position in the indirectly detected dimension(s) after data acquisition can be accomplished by simply applying a linear phase correction to the FIDs as in the States method. In addition, because the receiver phase is shifted by 180° for every t_1 increment, the axial signals invert their sign every t_1 increment as in the TPPI method, while the other signals remain unchanged relative to the regular States method. As a result, axial peaks in the TPPI–States method, like those in the TPPI method, are moved to the edge of the spectrum.

2.4.2. *Phase Corrections.* Another consideration to bear in mind is the phase correction required in both the directly and indirectly detected dimensions. To ensure flat baselines and absorptive folded peaks, the experimental conditions should be adjusted to ensure that the zero and first order phase corrections are either 0° and 0°, respectively, or 90° and −180°, respectively.[31,32] In the former case, the first data point should also be divided by two prior to Fourier transformation.[32]

Because of the need to optimize digital resolution, extensive folding can often be used to great effect, particularly in the case of ^{13}C where the complete spectral width to be covered is very large. If the zero and first order phase corrections are both set to 0°, then all folded peaks will have the same phase as the non-folded ones. When the zero and first order phase corrections are set to 90° and −180°, respectively, the folded peaks have positive or negative amplitudes depending on whether the number of times they are folded is even or odd.[32]

The zero order phase in the directly detected dimension can be adjusted by varying the relative receiver phase, while the first order phase can be adjusted by varying the delay between the last pulse of the experiment and the start of acquisition.[31]

For the indirectly detected dimensions, the zero (P_0) and first order phase (P_1) corrections can be adjusted by appropriately setting the value of $t(0)$, the value of the incremental delay at time zero. This is readily calculated by approximating the 90° pulses by a Dirac delta function displaced in time by $\delta = 2\tau_{90}/\pi$ and using the formula

$$P_1 = -2P_0 = -x[\Sigma\delta + \Sigma\tau_{180} + t(0)]/\Delta t$$

where Δt is the incremental delay, and x is either 360° in the case of the States and States–TPPI

methods, or 180° in the case of TPPI. Thus, for a simple NOESY sequence of the type

$$90°\text{-}t_1\text{-}90°\text{-}\tau_m\text{-}90°\text{-Acq}$$

the first order phase correction in the t_1 dimension is given by $-x[4\tau_{90}/\pi + t_1(0)]/\Delta t$.

2.4.3. *Off-Resonance Excitation Pulses.* Under certain circumstances it is useful to apply a pulse which has its maximum excitation a distance $\Delta\nu$ from the carrier position. For example, in the case of a spectrum recorded in water in which only protons bonded to ^{15}N are detected, it may be desirable to reduce the spectral width, and thereby optimize the digital resolution, by placing the carrier frequency in the middle of the NH region rather than at the water resonance position. Consequently, off-resonance pre-saturation is required. Similarly, in triple resonance experiments in which both aliphatic and carbonyl carbon spins need to be excited, it may be desirable to use only a single ^{13}C channel (i.e. one synthesizer) with the carrier placed in the middle of the aliphatic carbon spectrum. Hence, off-resonance excitation of the carbonyl spins must be used as they resonate ~ 130 ppm downfield from the center of the aliphatic carbon spectrum. This is readily achieved using a DANTE pulse scheme of the type[33]

$$[\theta_0\theta_{\pm\phi}\theta_{\pm 2\phi}\cdots\theta_{\pm(n-1)\phi}]N$$

repeated N times, where the length τ_θ of the pulse θ is given by $1/[n\Delta\nu]$, and the phase ϕ is given by $2\pi/n$ radians and $e^{in\phi} = 1$. To set the excitation maximum upfield or downfield from the carrier, the phase is successively incremented or decremented by ϕ, respectively, and the total length of the pulse train is set to the desired length of the excitation pulse. The magnitude of the frequency distribution $M(\nu)$ of this DANTE pulse train is given by

$$M(\nu) = \sum_{m=-\infty}^{\infty} |(B_1/\pi m)\sin(\omega_m\tau_\theta/2)| \cdot \left\{n + 2\sum_{p=1}^{n-1}(n-p)\cos[p(\omega\tau_\theta+\phi)]\right\}^{1/2} \cdot \delta[\nu - \omega_m/(2\pi)]$$

where m is the sideband number and δ is a Dirac delta function defined as $\delta(t - mn\tau_\theta)$ equals 0 if $t \neq mn\tau_\theta$ and 1 if $t = mn\tau_\theta$. This reduces to a series of sidebands centered $1/(n\tau_\theta)$ upfield (or downfield) from the carrier and spaced at $1/\tau_\theta$ Hz apart with intensities that decrease asymmetrically with respect to the offset from the central band. In practical applications, the carrier frequency and the values of n and τ_θ are chosen such that only the central band lies within the spectral regions of interest.

2.4.4. *Phase Cycling.* The main purpose of phase cycling is to ensure that only the desired coherence transfer pathway gives rise to magnetization detected in the acquisition dimension. In general, a single undesired coherence transfer pathway can usually be eliminated by a simple two-step phase cycle.[14] For each additional source of artifacts, further phase cycling in an independent manner is commonly carried out.[14] For example, in a simple NOESY sequence, phase cycling of the preparation pulse along $\pm x$ suppresses axial peaks. Suppression of single-quantum coherent transfer can then be achieved by phase cycling the last pulse along $\pm x$. If both phase cycles are executed simultaneously, single quantum coherent transfer of axial peaks would not be suppressed in the final spectrum. If on the other hand, the two phase cycles are executed independently giving rise to a 4 step phase cycle, each artifact will be eliminated.

In the case of 3D and 4D experiments, there may be a very large number of possible spurious transfer pathways. As extensive phase cycling is severely limited by the need to keep the measurement time down to practical levels, it may be necessary to consolidate several of the phase cycling steps. This can be achieved by executing two phase cycles simultaneously providing their purpose is to eliminate two unrelated sources of artifacts.[34] In such a case, if the first phase cycle completely cancels undesired magnetization that would result in an artifact with fractional intensity a, and the second phase cycle cancels a second unrelated artifact of fractional intensity b, then the intensity of the residual artifacts in the final spectrum will be very low and given by the product $a \times b$.

3. SEQUENTIAL ASSIGNMENT USING 3D HETERONUCLEAR NMR METHODS

Conventional assignment procedures using homonuclear ^1H–^1H 2D NMR methods, make use of correlation experiments of the COSY and HOHAHA type to identify direct and relayed through-bond connectivities, and NOESY experiments to obtain sequential through-space connectivities of the type $C^\alpha H/NH/C^\beta H(i)$–$NH(i+1)$, $C^\alpha H(i)$–$NH(i+2,3,4)$ and $C^\alpha H(i)$–$C^\beta H(i+3)$ along the polypeptide chain.[1,35] In order to alleviate overlap problems, it is also possible to use two 2D ^1H–^{15}N relayed HMQC–NOESY and HMQC–HOHAHA spectroscopy in which the NH chemical shifts are replaced by the corresponding ^{15}N chemical shifts.[36,37] Exactly the same philosophy can be employed in 3D heteronuclear NMR.[12,38] In addition, however, a number of triple resonance experiments involving correlations of ^1H_N, ^{13}C and ^{15}N chemical shifts can provide sequential connectivities by means of heteronuclear J couplings, without recourse to the NOE.[39,40] These procedures will be illustrated with regard to two larger proteins, interleukin-1β (IL-1β, 153 residues) and calmodulin (148 residues).

3.1. *Assignment of Spin Systems by Heteronuclear 3D NMR*

The strategy to identify spin systems using heteronuclear 3D NMR comprises two stages.[41] In the first step the NH and ^{15}N chemical shifts of each residue are correlated with the corresponding $^{13}C^\alpha$ carbon and $C^\alpha H$ proton chemical shifts on a sample dissolved in H_2O. The NH, ^{15}N and $C^\alpha H$ shifts are correlated using either the double resonance 3D ^1H–^{15}N HOHAHA–HMQC[38] or the triple resonance $C^\alpha H(^{13}C^\alpha)$–$^{15}N$–$NH(H(CA)NH)$[27] correlation experiments. The NH, ^{15}N and $^{13}C^\alpha$ chemical shifts are correlated using the triple resonance ^1H–^{15}N–$^{13}C^\alpha$ (HNCA) experiment.[39–41] It is very important to obtain the latter spectrum, in addition to one of the two former ones, in order to correlate the $C^\alpha H$ ^1H and $^{13}C^\alpha$ chemical shifts of a given residue unambiguously, as for larger proteins with many degenerate $C^\alpha H$ chemical shifts, the $^{13}C^\alpha$ chemical shifts cannot simply be determined by recording a 2D ^1H–^{13}C shift correlation spectrum. In the second step, the side chain spin systems are established by correlating the aliphatic ^1H and attached ^{13}C chemical shifts using the HCCH–COSY[34,41,42] and HCCH–TOCSY[41,43] experiments on samples dissolved in D_2O in which magnetization transfer is achieved via the large ^1H–^{13}C and ^{13}C–^{13}C couplings.[34,41–44]

3.1.1. *The 3D ^1H–^{15}N HOHAHA–HMQC Experiment.* The pulse sequence for the ^{15}N-separated HOHAHA–HMQC is shown in Fig. 5.[38,45] Aliphatic ^1H chemical shifts evolve during the evolution period t_1. In the next step, transfer of magnetization originating on aliphatic protons to the corresponding intraresidue NH protons proceeds via isotropic mixing of ^1H magnetization using, for example a [DIPSI-2-60°]$_n$ pulse train.[46,47] Heteronuclear multiple quantum coherence is generated during the evolution period t_2, and subsequently converted back into transverse ^1H magnetization so that at the end of the t_2 period ^1H magnetization is modulated by the shift of the directly attached ^{15}N nucleus. Magnetization now residing on the NH protons is finally detected during t_3.

In addition to providing intraresidue correlations between aliphatic and NH protons, the ^{15}N-separated HOHAHA–HMQC experiment recorded with a short mixing time (<35 ms) can be used to obtain a semi-quantitative estimate of $^3J_{\alpha\beta}$ coupling constants from the intensities of the well resolved HN–$C^\beta H$ cross peaks.[45]

Cross peak intensities in isotropic mixing experiments depend on the rate at which magnetization flows through a J-coupled spin system during the mixing period.[45] This rate depends not only on the topology of the spin system and on the size of the pertinent J couplings, but also on the quality of the isotropic mixing scheme used. For the newer isotropic mixing schemes of the DIPSI variety, off-resonance effects are minimal, and near-ideal mixing can be obtained over a substantial bandwidth.[46,47] Cross peak intensities also depend on the relaxation rates of the originating and destination protons, as well as on the other proton spins involved in the transfer pathway. These relaxation rates are generally only known with a low degree of accuracy, and may vary substantially for amino acids of the same type at different locations in the protein. This diversity in relaxation rates makes it difficult to fit in a rigorous manner the cross peak intensities observed in HOHAHA type

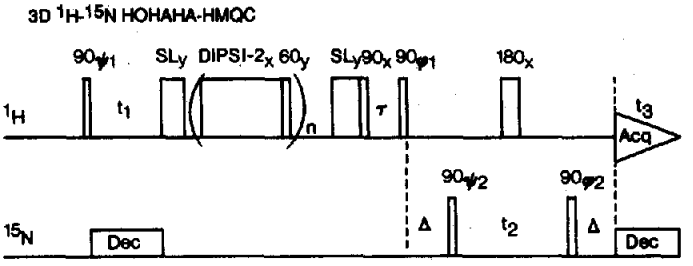

FIG. 5. Pulse sequence for the 3D ^{1}H–^{15}N HOHAHA–HMQC experiment.[45] The phase cycling is $\psi1 = x, -x$; $\phi2 = 2(x), 2(-x)$; $\phi1 = 4(x), 4(y), 4(-x), 4(-y)$; Acq = x, 2(−x), x, −y, 2(y), −y, −x, 2(x), −x, y, 2(−y), y. The delay τ is equal to half the DIPSI-2 mixing time to minimize ROE effects, and the delay $\Delta = 1/(2J_{NH})$ (or slightly less to avoid losses due to relaxation). TP is a trim pulse (usually set to ~800 μs), and ^{15}N decoupling (Dec) during the t_1 evolution period and the acquisition time can be readily achieved with random GARP modulation.

spectra to magnetization transfer curves that can be calculated for each of the amino acids.[48] However, a good estimate of the relative size of the J coupling between the C$^\alpha$H and C$^{\beta2}$H/C$^{\beta3}$H protons can be obtained from relative intensities of the HN–C$^{\beta2}$H and HN–C$^{\beta3}$H cross peaks, assuming that the two β-methylene protons of the same pair have similar relaxation times. Since relaxation of the β-methylene protons is typically dominated by their geminal dipolar interaction, this assumption is perfectly reasonable. Thus, if only the relative amount of HN–C$^{\beta2}$H and HN–C$^{\beta3}$H magnetization transfer is of interest, the magnetization from the HN to the C$^\beta$H protons may be calculated neglecting relaxation, since relaxation of the HN and C$^\alpha$H protons has the same effect on both magnetization transfers.

Figure 6 shows the transfer of magnetization from the HN to the C$^\beta$H protons as a function of mixing time for a residue with two non-equivalent C$^\beta$H protons.[45] The curves are calculated with coupling constants of $^3J_{HN\alpha} = 5$ or 10 Hz, $^3J_{\alpha\beta3} = 4$ Hz, and $^3J_{\alpha\beta2} = 11$ Hz. As expected, it is seen that for short mixing times transfer to the C$^{\beta2}$H proton is much larger than transfer to the C$^{\beta3}$H proton. Figure 7 plots the ratio of the two cross peak intensities as a function of mixing time. This ratio can be slightly reduced if there are other protons coupled to the C$^\beta$H protons. The dashed lines in both Figs 6 and 7 correspond to a 'worst case scenario' where a single C$^\gamma$H proton has a large coupling (11 Hz) to C$^{\beta2}$H and a small coupling (4 Hz) to C$^{\beta3}$H. As can be seen in Fig. 7, this reduces the cross peak ratio slightly for short mixing times (< 35 ms), although the absolute HN–C$^\beta$H cross peak intensities can be affected quite significantly (Fig. 6).

Distinguishing between amino acids with free rotation about the C$^\alpha$–C$^\beta$ bond and amino acids with the $\chi_1 = 60°$ rotamer that puts both methylene protons in *gauche* positions with respect to the C$^\alpha$H proton, requires a comparison of the HN–C$^\alpha$H and HN–C$^\beta$H cross peak intensities. Because the transverse relaxation rates of the C$^\alpha$H and C$^\beta$H protons may differ substantially, this type of semi-quantitative interpretation of cross peak ratios is less straightforward than the case discussed above. In the case of a fixed rotamer with $\chi_1 = 60 \pm 30°$, both $^3J_{\alpha\beta}$ couplings are less than about 4 Hz, whereas in the case of free rotation, the couplings are between 6 and 8 Hz. Thus, stronger HN–C$^\beta$H cross peaks are expected for the free rotation case relative to a fixed $\chi_1 \sim 60°$ rotamer. These cross peak intensities, however, also depend strongly on the size of the $^3J_{HN\alpha}$ coupling. Figure 8 shows the ratio of the intensities expected for the HN–C$^\beta$H and HN–C$^\alpha$H cross peaks for both 4 and 7 Hz $^3J_{\alpha\beta}$ couplings, assuming identical relaxation times for all spins involved.[45] In the case of free rotation, the relaxation time of the C$^\beta$H protons is expected to become longer relative to the case of a fixed rotamer, which would increase the C$^\beta$H/HN : C$^\alpha$H/HN cross peak ratio to an even larger value compared to the fixed $\chi_1 \sim 60°$ rotamer. The C$^\beta$H/HN : C$^\alpha$H/HN cross peak ratios shown in Fig. 7 are drawn for the $^3J_{HN\alpha}$ coupling of 7 Hz but depend only weakly on the size of this coupling provided it is in the 4–10 Hz range.

Figure 9 illustrates the HN–C$^\alpha$H and HN–C$^\beta$H cross peaks for some typical residues obtained for 3D ^{15}N-separated HOHAHA–HMQC spectrum of ^{15}N-labeled IL-1β recorded with a duration of

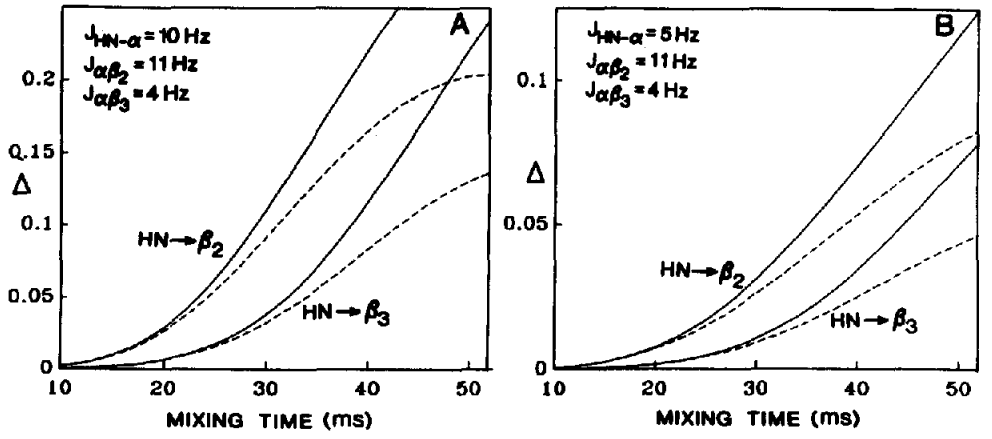

FIG. 6. Fraction of magnetization, Δ, transferred from the HN to the $C^{\beta 2}H$ and $C^{\beta 3}H$ protons as a function of the duration of isotropic mixing in the 3D ^1H–^{15}N HOHAHA–HMQC experiment for (A) $^3J_{HN\alpha} = 10$ Hz and (B) $^3J_{HN\alpha} = 5$ Hz.[45] For both cases $^2J_{\beta 2\beta 3} = -14$ Hz. Ideal isotropic mixing is assumed and the fractions are calculated in the absence of relaxation. Relaxation attenuates the HN→$C^{\beta 2}H$ and HN→$C^{\beta 3}H$ magnetization transfer to the same extent. The solid lines correspond to a spin system without $C^\gamma H$ protons; the dashed lines correspond to a spin system with a single $C^\gamma H$ proton with $^3J_{\beta 2\gamma} = 11$ Hz and $^3J_{\beta 3\gamma} = 4$ Hz.

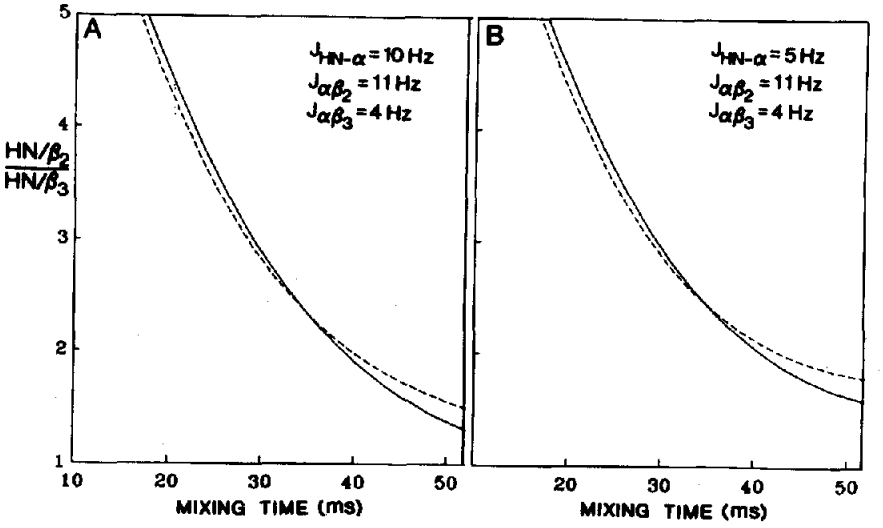

FIG. 7. Ratio of the HN–$C^{\beta 2}H$ and HN–$C^{\beta 3}H$ cross peak intensities as a function of isotropic mixing duration in the 3D ^1H–^{15}N HOHAHA–HMQC experiment for (A) $^3J_{HN\alpha} = 10$ Hz, and (B) $^3J_{HN\alpha} = 5$ Hz.[45] The solid lines correspond to a spin system without $C^\gamma H$ protons, the dashed lines correspond to a spin system with a single $C^\gamma H$ proton with $^3J_{\beta 2\gamma} = 11$ Hz and $^3J_{\beta 3\gamma} = 4$ Hz.

30.7 ms for the DIPSI-2 mixing sequence.[45] In the case of $\chi_1 = -60°$ (Fig. 9A) or $\chi_1 = 180°$ (Fig. 9B), it is generally the case that only one of the two possible HN–$C^\beta H$ cross peaks is observed, corresponding to the $C^\beta H$ proton with the larger $^3J_{\alpha\beta}$ coupling (i.e. $C^{\beta 2}H$ in the case of $\chi_1 = -60°$ and $C^{\beta 3}H$ in the case of $\chi_1 = 180°$). Occasionally both HN–$C^\beta H$ cross peaks can be observed (e.g. Asp-142 in Fig 9A), but in such cases one of the cross peaks is much stronger than the other. For those residues with $\chi_1 = 60°$

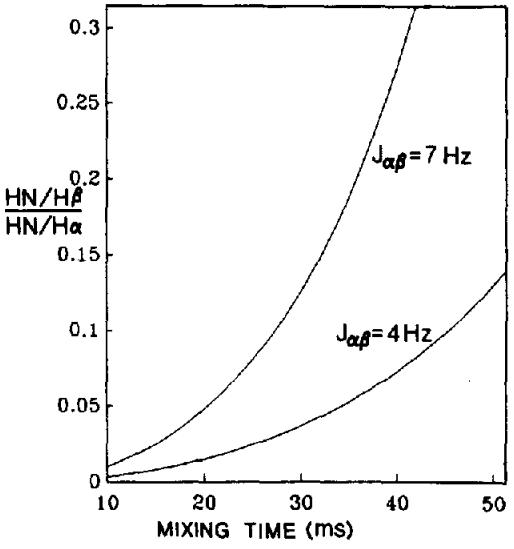

FIG. 8. Ratio of the HN–C$^{\alpha}$H and HN–C$^{\beta}$H cross peak intensities in the 3D ^{1}H–^{15}N HOHAHA–HMQC experiment when both C$^{\beta}$H methylene protons have identical couplings to the C$^{\alpha}$H proton.[45] The HN–C$^{\beta}$H cross peak intensity corresponds to a single C$^{\beta}$H proton. (i.e. If the two C$^{\beta}$H protons have degenerate chemical shifts the cross peak ratio will be twice that shown in the graph.) The cross peak ratios have been calculated with $^{3}J_{HN\alpha} = 7$ Hz and no C$^{\gamma}$H protons.

(Fig. 9C), where both $^{3}J_{\alpha\beta}$ couplings are small, no relayed HN–C$^{\beta}$H cross peaks are observed. Finally, for those residues with disordered χ_1 conformations (Fig. 9D), both HN–C$^{\beta}$H cross peaks are seen with approximately equal intensity.

3.1.2. *The 3D H(CA)NH Experiment.* The pulse sequence for the 3D H(CA)NH experiment is shown in Fig. 10.[27] The C$^{\alpha}$H chemical shifts evolve during the evolution period t_1 and ^{1}H magnetization is subsequently transferred by an INEPT sequence to the directly coupled ^{13}C$^{\alpha}$ spin. Immediately prior to the transfer the water and antiphase C$^{\alpha}$H spins are orthogonal so that a ^{1}H trim pulse can be applied to suppress the water signal. After the application of 90° ^{1}H and ^{13}C$^{\alpha}$ pulses, the antiphase ^{13}C$^{\alpha}$ polarization is refocused with respect to the C$^{\alpha}$H spins during the period $2\tau_{II}$, after which ^{13}C$^{\alpha}$–^{15}N dephasing occurs during the interval $2\delta_{II}$. By suitably concatenating the 180° pulses as described in Section 2.3, the ^{13}C$^{\alpha}$–C$^{\alpha}$H refocusing and ^{13}C$^{\alpha}$–^{15}N defocusing periods overlap, thereby shortening the total length of the delays required. The next ^{13}C 90° pulse creates *zz* carbon–nitrogen magnetization, and the following ^{1}H trim and 90°$_{y}$ pulses serve to suppress the water resonance further. Magnetization is then transferred to ^{15}N by the application of a ^{15}N 90° pulse and ^{15}N chemical shifts evolve during the period t_2. The effects of ^{1}H–^{15}N and ^{13}C$^{\alpha}$–^{15}N J coupling are removed during this time by application of ^{1}H and ^{13}C 180° pulses. ^{15}N magnetization is refocused with respect to the ^{13}C$^{\alpha}$ spin during the delay $2\delta_{III}$ and defocused with respect to the directly bonded NH proton during $2\tau_{III}$ to allow transfer back to NH protons via an INEPT sequence. Finally, NH chemical shifts are detected during t_3. The effects of one-bond ^{13}C$^{\alpha}$–CO and ^{1}H–^{15}N couplings are removed by GARP decoupling during the time that ^{13}C$^{\alpha}$ transverse magnetization evolves and during the acquisition period, respectively.

Optimal choices for the delays τ_{II} and δ_{II} are found by maximizing the magnetization transferred from the ^{13}C$^{\alpha}$ to the ^{15}N spins given by[27]

$$\sin(2\pi^{1}J_{C\alpha N}\delta_{II})\cdot\cos(2\pi^{2}J_{C\alpha N}\delta_{II})\cdot\cos(2\pi J_{C\alpha\beta}\delta_{II})\cdot\sin(2\pi J_{HC\alpha}\tau_{II})\cdot\exp(-2\delta_{II}/T_{2C\alpha}).$$

As $^{1}J_{HC\alpha} \gg {}^{1}J_{C\alpha N}$, the optimal value of τ_{II} is $1/(4J_{HC\alpha})$. The optimal value of δ_{II} depends not only on the

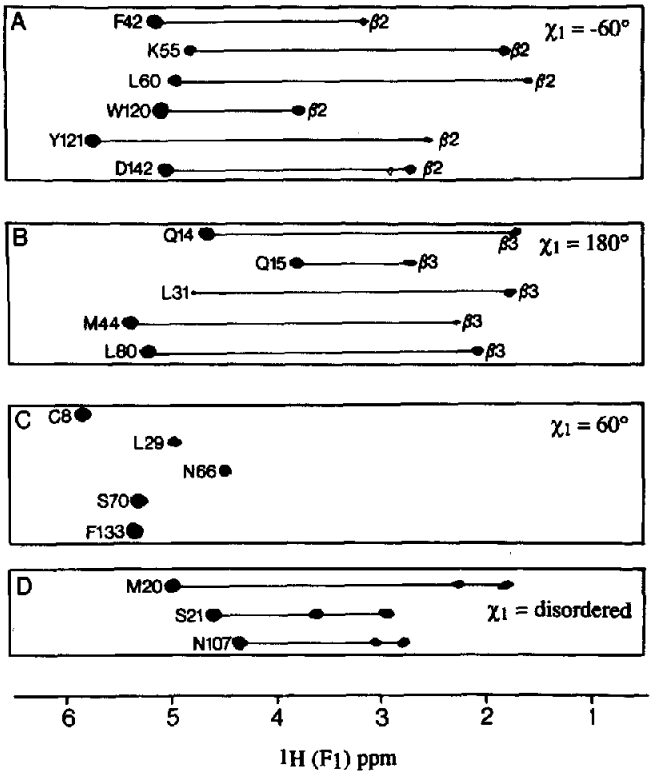

FIG. 9. Composite of amide strips taken from the 3D ^{15}N-separated HOHAHA–HMQC spectrum of ^{15}N labeled IL-1β recorded with a 30.7 ms mixing time showing NH–C$^{\alpha}$H and NH–C$^{\beta}$H cross peaks for a number of residues.[45] Examples of residues with $\chi_1 = -60°$, 180° and 60° are shown in (A), (B) and (C), respectively, while residues with disordered χ_1 conformations are shown in (D). (See Section 3.2 for a description of how the strips are extracted from the 3D spectrum.)

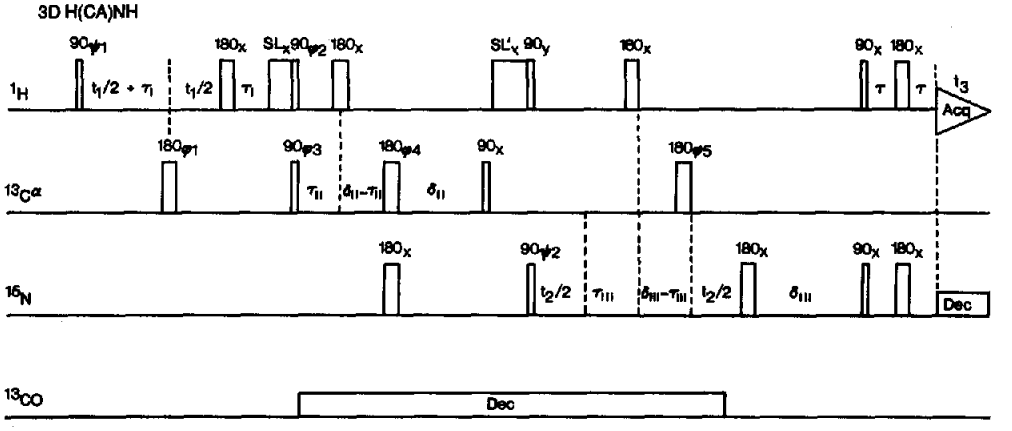

FIG. 10. Pulse sequence for the 3D H(CA)NH experiment.[27] The phase cycling is: $\psi 1 = x$, $\psi 2 = 16(x), 16(-x)$, $\phi 1 = x, -x$; $\phi 2 = x, -x$, $\phi 3 = 2(x), 2(-x)$, $\phi 4 = 4(x), 4(y), 4(-x)\ 4(-y)$, $\phi 5 = 8(x), 8(-x)$. Typical durations for the delays are $\tau_I = 1.5$ ms, $\tau_{II} = 1.7$ ms, $\delta_{II} = 12.5$ ms, $\tau_{III} = 2.75$ ms, $\delta_{III} = 11.5$ ms. $\tau = 2.25$ ms, slightly less than $1/(4J_{NH})$. Water suppression is achieved using two purge pulses SL_x and SL'_x, typically applied for 1.5 and 9 ms, respectively. GARP[78] modulation is used for carbonyl decoupling, while ^{15}N decoupling during acquisition can be accomplished with either WALTZ[79] or GARP modulation.

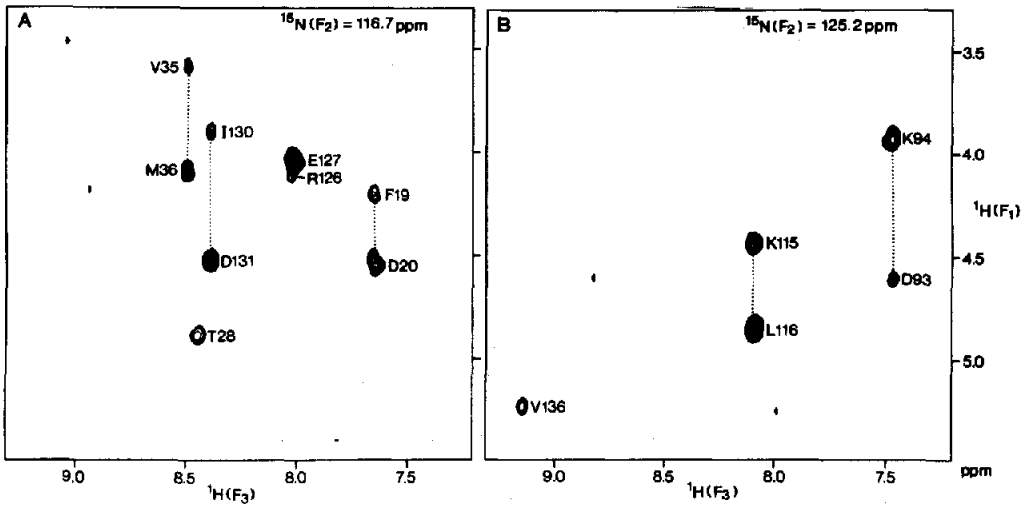

FIG. 11. Examples of two NH(F_3)–C$^\alpha$H(F_1) planes at different ^{15}N(F_2) frequencies of the 500 MHz 3D H(CA)NH spectrum of 1.5 mM ^{15}N/^{13}C labeled calmodulin in 90% H_2O/10% D_2O.[27] Strong intraresidue C$^\alpha$H(i)–NH(i)–N(i) and weaker interresidue C$^\alpha$H($i-1$)–NH(i)–N(i) correlations are observed.

couplings but also on the $^{13}C^\alpha$ linewidths. For $^1J_{C\alpha N} = 11$ Hz, $^2J_{C\alpha N} = 7$ Hz, $^1J_{C\alpha\beta} = 37$ Hz and $1/(\pi T_{2C\alpha}) = 15$–$20$ Hz, the optimal value of δ_{II} is 12–13 ms.

Similarly optimal choices for the delays τ_{III} and δ_{III} are found by maximizing the magnetization transferred from ^{15}N to the directly attached amide proton given by[27]

$$\sin(2\pi^1 J_{C\alpha N}\delta_{III}) \cdot \cos(2\pi^2 J_{C\alpha N}\delta_{III}) \cdot \sin(2\pi J_{NH}\tau_{II}) \exp(-2\delta_{III}/T_{2N}).$$

As $^1J_{NH} \gg {}^1J_{C\alpha N}$, τ_{III} should be set to $1/(4J_{NH})$. The value of δ_{III} also depends on the ^{15}N linewidths, and for $^1J_{C\alpha N} = 11$ Hz, $^2J_{C\alpha N} = 7$ Hz and a ^{15}N linewidth of 7 Hz, the optimal value of δ_{III} is 11.5 ms.

Two sets of correlations are observed in the 3D H(CA)NH experiment: the intraresidue connectivity between C$^\alpha$H(i), ^{15}N(i) and NH(i) arising from transfer of magnetization via the 11 Hz one-bond $^{13}C^\alpha$–^{15}N coupling, and the sequential interresidue connectivity between C$^\alpha$H($i-1$), ^{15}N(i) and NH(i) via the 7 Hz two bond $^{13}C^\alpha$–^{15}N coupling. This is illustrated in Fig. 11 by two NH(F_3)–C$^\alpha$H(F_1) planes of the 3D H(CA)NNH spectrum of ^{15}N/^{13}C-labeled calmodulin.[27]

3.1.3. *The 3D HNCA Experiment.* The pulse sequence for the HNCA experiment is shown in Fig. 12.[39–41] Magnetization originally residing on the NH protons is transferred to their directly attached ^{15}N via an INEPT sequence, and ^{15}N chemical shifts evolve during the period t_1, with $^{13}C^\alpha$ and ^{1}H decoupling achieved by the application of 180° ^{1}H and ^{13}C pulses in the middle of t_1. During the delay δ (set to an integral multiple of $1/J_{NH}$) ^{15}N magnetization becomes antiphase with respect to the coupled $^{13}C^\alpha$ spin(s). To minimize relaxation losses while still optimizing transfer via two-bond ^{15}N–$^{13}C^\alpha$ couplings, δ is best set to $1/(3J_{NC\alpha})$. Subsequent application of 90° pulses simultaneously to both ^{1}H and $^{13}C^\alpha$ establishes three-spin NH–^{15}N–$^{13}C^\alpha$ coherence (i.e. the term $I_yN_xA_y$ is generated where I, N and A refer to ^{1}H, ^{15}N and ^{13}C spins). Evolution of solely $^{13}C^\alpha$ chemical shifts during the period t_2 is ensured by refocussing of ^{1}H and ^{15}N chemical shifts through the application of ^{1}H and ^{15}N 180° pulses at the midpoint of the t_2 period. Magnetization is then transferred back to NH protons by simply reversing the above procedure.

In terms of the product operator formalism, assuming for simplicity that the two-bond coupling between ^{15}N(i) and $^{13}C^\alpha(i-1)$ is zero and that the delay $\delta = 1/(2J_{NC\alpha})$, (where $J_{NC\alpha}$ is the one-bond ^{15}N–$^{13}C^\alpha$ J coupling), the evolution of magnetization during the course of this experiment can be

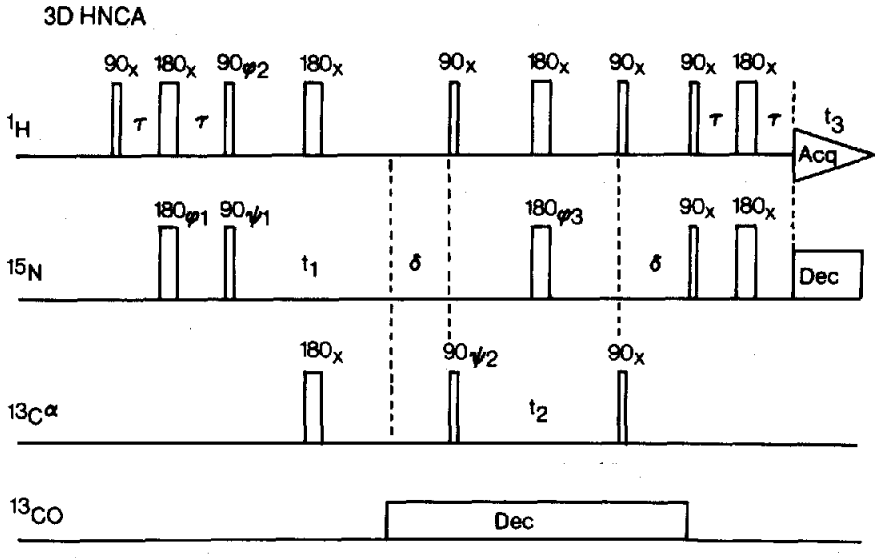

FIG. 12. Pulse sequence of the 3D HNCA experiment.[40] The phase cycling is: $\psi 1 = x; \psi 2 = 2(x), 2(-x); \phi 1 = x, -x; \phi 2 = y, -y; \phi 3 = 4(x), 4(y), 4(-x), 4(-y)$; Acq = x, 2(−x), x, −x, 2(x), −x. Typical delay durations are $\delta = 33$ ms (tuned to an integral number of $1/J_{NH}$ and $\tau = 2.25$ ms, slightly less than $1/(4J_{NH})$. Carbonyl decoupling is achieved using GARP modulation, while ^{15}N decoupling during acquisition can be accomplished with either WALTZ or GARP modulation.

described as:[40]

$$I_z \xrightarrow{A} -2I_zN_y \xrightarrow{t_1} 2I_zN_y \cos \Omega_N t_1 \cos \pi J_{NCO} t_1 \xrightarrow{B} -4I_yN_xA_y \cos \Omega_N t_1 \cos \pi J_{NCO} t_1$$

$$\xrightarrow{t_2} 4I_yN_xA_y \cos \Omega_N t_1 \cos \pi J_{NCO} t_1 \cos \Omega_A t_2 \xrightarrow{C} I_x \cos \Omega_N t_1 \cos \pi J_{NCO} t_1 \cos \Omega_A t_2,$$

where I, N and A denote the intraresidue NH, ^{15}N and ^{13}C$^\alpha$ spins, and the carbonyl spin of the preceding residue is denoted by CO. The chemical shifts of the intraresidue ^{15}N and ^{13}C$^\alpha$ spins are denoted as Ω_N and Ω_A, and J_{NCO} is the interresidue ^{15}N–^{13}CO coupling constant. If a significant two bond-coupling, $^2J_{NC\alpha(i-1)}$, between ^{15}N(i) and the preceding ^{13}C$^\alpha$($i-1$) spin, A', exists, the signal immediately prior to detection is then given by[40]

$$I_x \cos \Omega_N t_1 \cos \pi J_{NCO} t_1 \{\cos \Omega_A t_2 [\sin \pi J_{NC\alpha} \delta \cos \pi J_{NC\alpha(i-1)} \delta]^2$$
$$+ \cos \Omega_{A'} t_2 [\sin \pi J_{NC\alpha(i-1)} \delta \cos \pi J_{NC\alpha} \delta]^2\}.$$

In both cases the detected signal is amplitude modulated in both the t_1 and t_2 dimensions, indicating that the line shape after 3D Fourier transformation is pure absorption. It should also be noted that as the acquisition time usually employed in the ^{15}N dimension ($\sim$20 ms for a spectral width of 1670 Hz and 32 complex data points) is shorter than $1/(2J_{NCO})$($\sim$33 ms), the J_{NCO} coupling present during the t_1 evolution period has little effect on the signal.

As in the H(CA)NH experiment, two sets of correlations can be observed in the HNCA spectrum: the intraresidue C$^\alpha$(i)–^{15}N(i)–NH(i) connectivity via the one bond $^1J_{NC\alpha}$ coupling (8–12 Hz) and the interresidue C$^\alpha$($i-1$)–^{15}N(i)–NH(i) connectivity via the two-bond $^2J_{NC\alpha}$ coupling (5–7 Hz). Examples of NH(F_3)–^{13}C(F_2) planes at different ^{15}N chemical shifts of the HNCA spectrum of ^{15}N/^{13}C labeled IL-1β are shown in Fig. 13.[41] Note that it is a simple matter to distinguish intra-from interresidue connectivities, as the former are more intense than the latter.

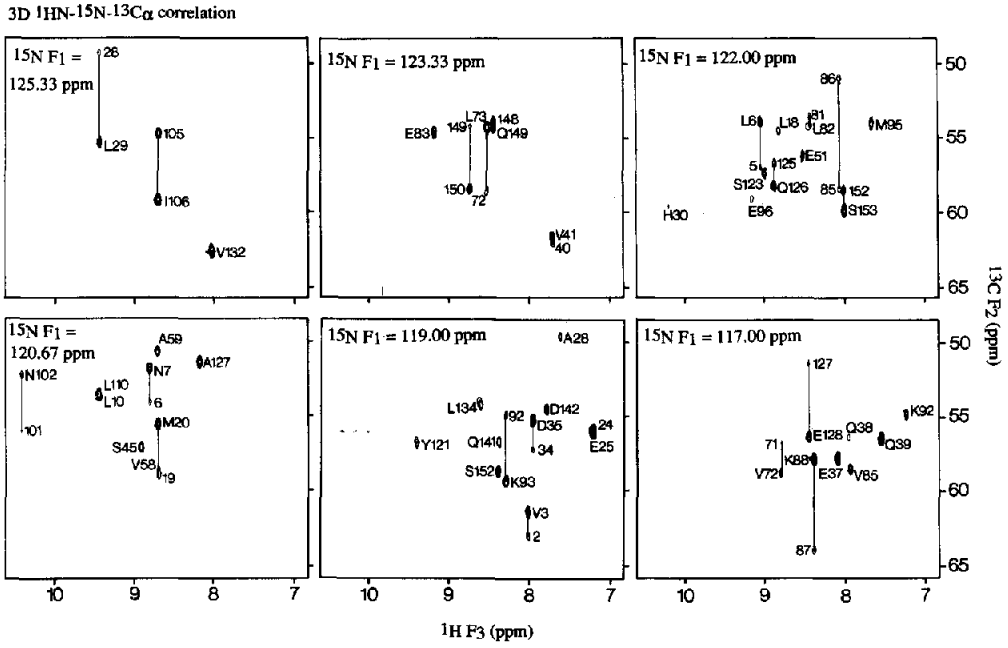

FIG. 13. Examples of six representative NH(F_3)–$^{13}C^{\alpha}$(F_2) planes at different ^{15}N(F_1) frequencies of the 500 MHz 3D HNCA spectrum of 1.7 mM $^{15}N/^{13}C$ labeled IL-1β in 90% H_2O/10% D_2O.[41] Strong intraresidue $^{13}C^{\alpha}(i)$–NH(i)–N(i) and weaker interresidue $^{13}C^{\alpha}(i-1)$–NH(i)–N(i) correlations are observed.

3.1.4. *Side Chains: The 3D HCCH–COSY and HCCH–TOCSY Experiments.* Once the $C^{\alpha}H$ and $^{13}C^{\alpha}$ resonances of each residue have been correlated, complete amino acid spin systems can be delineated[41] using the HCCH–COSY[34,42] and HCCH–TOCSY[43] experiments. Both experiments are based on analogous principles and make use of the well resolved one-bond ^1H–^{13}C (140 Hz) and ^{13}C–^{13}C (30–40 Hz) J couplings to transfer magnetization along the side chain via the pathway

$$^1H \xrightarrow{^1J_{CH}} {}^{13}C \xrightarrow{^1J_{CC}} {}^{13}C \xrightarrow{^1J_{CH}} {}^1H.$$

By this means, all the problems associated with conventional ^1H–^1H correlation experiments, which rely on poorly resolved three-bond ^1H–^1H couplings (3–12 Hz), are circumvented.

The pulse schemes for these two experiments are shown in Fig. 14.[34,43] After the evolution period t_1, ^1H magnetization (H_A) is transferred to its directly bonded ^{13}C nucleus (C_A) via the $^1J_{CH}$ coupling in an INEPT-type manner. The ^{13}C magnetization which is antiphase with respect to the polarization of H_A becomes in-phase during the delay $2\delta_1$, and ^{13}C magnetization evolves during the evolution period t_2 under the influence of the ^{13}C chemical shift. The 180° ^1H and ^{13}CO pulses during t_2 remove the effects of ^1H–^{13}C coupling and eliminate $J_{C\alpha CO}$ dephasing of the $^{13}C^{\alpha}$ magnetization, respectively. During t_2 and the delay δ_1, C_A magnetization becomes antiphase with respect to its ^{13}C coupling partner C_B at a rate that is determined by $^1J_{CC}$. In the case of the HCCH–COSY experiment (Fig. 14A) a 90° ^{13}C pulse then transfers this antiphase C_A magnetization into antiphase C_B magnetization in a COSY-like manner. During the following interval $2(\Delta+\delta_2)$, the antiphase C_B magnetization becomes in-phase with respect to C_A, and the 180° ^1H pulse (applied at time δ_2 before the final set of simultaneous 90° pulses) ensures that the refocused C_B magnetization is antiphase with respect to its attached proton H_B. Finally C_B magnetization is transferred to H_B by a reverse refocused INEPT which is detected during t_3. In the case of the HCCH–TOCSY experiment (Fig. 14B), on the other hand, a short ^{13}C trim pulse applied along the x axis at the end of the t_2 evolution period defocuses all

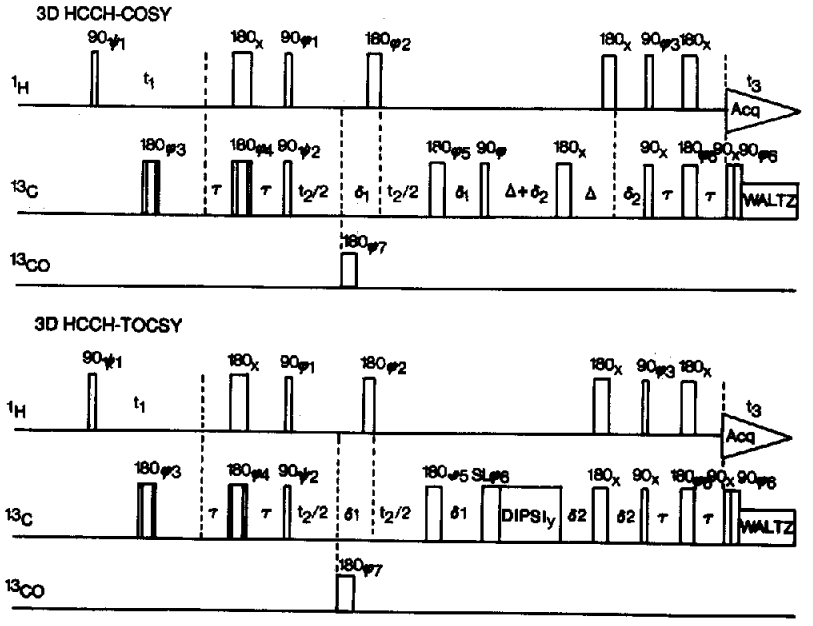

FIG. 14. Pulse sequences for the 3D HCCH–COSY[42] and HCCH–TOCSY[43] experiments. The phase cycling is: $\phi1 = y, -y$; $\phi2 = 4(x), 4(y), 4(-x), 4(-y)$; $\phi3 = 8(x), 8(-x)$; $\phi4 = 2(x), 2(-x)$; $\phi5 = 2(x), 2(y), 2(-x), 2(-y)$; $\phi6 = 4(x), 4(-x)$; $\phi7 = 8(x), 8(y)$; $\psi1 = x$; $\psi2 = x$; Acq $= 2(x-, -x, -x, x)\,2(-x, x, x, -x)$. The delay τ is set to 1.5 ms, slightly less than $1/(4J_{CH})$, the delays δ_1 and δ_2 are set to $\sim 1/(6J_{CH}) \sim 1.1$ ms, and the delay $\Delta + \delta_1$ is set to $\sim 1/(8J_{CC}) \sim 3.25$ ms. To eliminate the need for phase correction in the $^1H(F_1)$ dimension, the duration of the composite 180° ^{13}C pulse is added to the delay τ between the 180_x and $90_{\phi1}$ ^1H pulses. In the $^{13}C(F_2)$ dimension, phase correction is eliminated by applying the $180_{\phi2}$ ^1H pulse at the end of the first δ_1 interval. The simplest way to generate the $180_{\phi7}$ carbonyl pulse is with an off-resonance DANTE sequence (see Section 2.6). ^{13}C decoupling during acquisition can be achieved with GARP modulation. The 90_x–$90_{\phi6}$ pulse pair immediately prior to the start of GARP decoupling serves to reduce the intensity of modulation sidebands originating from incompletely refocused ^1H magnetization (I_yS_z type terms). This pulse pair has the effect of inverting S_z on alternate scans, cancelling signals originating from I_yS_z.

in-phase ^{13}C magnetization that is not parallel to the effective field, and the subsequent isotropic mixing period, accomplished with a DIPSI-3 scheme, transfers the net ^{13}C magnetization to its neighbors. Finally, like in the HCCH–COSY experiment, this ^{13}C magnetization is transferred back to the attached protons by a reverse INEPT sequence and detected in t_3.

The DIPSI-3 sequence is ideally suited for the HCCH–TOCSY experiment as, in the case of ^{13}C with relatively large homonuclear couplings (30–40 Hz), it can cover a bandwidth of $\sim \pm 0.75\,\nu$, where ν is the strength of the applied ^{13}C rf field. Thus, on a 500 MHz spectrometer an rf field strength of only ~ 7 kHz is needed for efficient isotropic mixing. Typically, this requires ~ 12.5 W of rf power, which is sufficiently low to permit mixing for periods up to 25 ms without causing substantial sample heating during the course of the experiment.

The final result in both cases is a 3D spectrum in which each $^1H(F_1)$–$^1H(F_3)$ plane has an appearance similar to that of a 2D ^1H–^1H COSY or HOHAHA/TOCSY experiment, but is edited by the chemical shift of the ^{13}C nucleus directly bonded to the ^1H at the diagonal position from which magnetization originates. Further, in contrast to the 2D correlation experiments, the cross peaks in each plane do not occur symmetrically on either side of the diagonal. This is represented diagrammatically in Fig. 15 for the simple case where magnetization is transferred from proton A to proton B.[41] In the plane corresponding to the chemical shift of the ^{13}C nucleus directly bonded to proton A where magnetization originates, a correlation is observed between a diagonal peak at

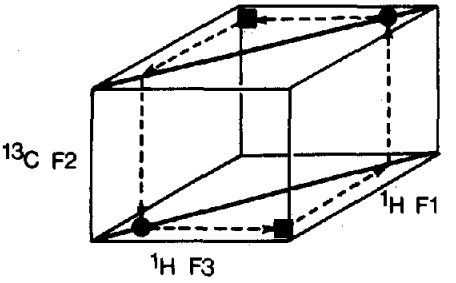

FIG. 15. Schematic diagram of two slices of an HCCH spectrum at different $^{13}C(F_2)$ chemical shifts showing the diagonal and cross peaks expected for a simple two spin system.[41] The diagonal peaks are represented by circles and the cross peaks by squares. Note that each slice is asymmetric about the diagonal, and cross peaks only appear in the F_3 dimension. This is due to the fact that magnetization originating from a proton attached to a given ^{13}C nucleus is only visible in the F_1–F_3 plane at the $^{13}C(F_2)$ chemical shift of this particular ^{13}C nucleus. The corresponding cross peak at the other side of the $F_1 = F_3$ diagonal is found in the plane taken at the ^{13}C frequency of the destination carbon.

$(F_1, F_3)=(\delta_A, \delta_A)$ and a cross peak $(F_1, F_3)=(\delta_A, \delta_B)$ in one half of the spectrum. The symmetric correlation between the diagonal peak at $(F_1, F_3)=(\delta_B, \delta_B)$ and the cross peak at $(F_1, F_3)=(\delta_B, \delta_A)$ is then seen in the plane corresponding to the chemical shift of the ^{13}C nucleus directly bonded to proton B. By this means, unambiguous checks on the assignments are afforded at each step in the process, which are made all the easier as the ^{13}C chemical shifts for different carbon types are located in characteristic regions of the ^{13}C spectrum with little overlap between them. This feature also permits use of extensive folding in the $^{13}C(F_2)$ dimension without the risk of introducing ambiguities. Further, this enables problems to be resolved which are associated with extensive chemical shift degeneracy. For example, even if the $C^\alpha H$, $^{13}C^\alpha$ and $C^\beta H$ chemical shifts of two residues are degenerate, one can still ascertain that two residues rather than one are involved and trace out the connnectivities for the remainder of the two spin systems providing the $^{13}C^\beta$ chemical shifts of the two residues are different.

The HCCH–COSY experiment is particularly useful for identifying Gly, Ala, Thr and Val spin systems, as well as for amino acids of the AMX type (e.g. Ser, Cys, Asn, Asp, His, Thr, Phe and Trp).[41] Figure 16 principally demonstrates the use of the HCCH–COSY experiment for the assignment of Gly and Ser spin systems in a sample of $^{13}C/^{15}N$-labeled IL-1β. Both these residues tend to pose problems in conventional ^1H–^1H correlation spectra as the proton resonances are often very close to each other. Each slice corresponds to several ^{13}C shifts separated by 20.71 ppm. Gly $^{13}C^\alpha$ shifts occur at 42–46 ppm, while $^{13}C^\alpha$ and $^{13}C^\beta$ shifts of Ser occur at 55–60 and 61–67 ppm, respectively. The two Gly $C^\alpha H$ protons are attached to the same C^α carbon, so that a symmetric pattern appears about the diagonal. The same is true, of course, for β-methylene protons. However, the β-methylene protons are also associated with cross peaks to the $C^\alpha H$ protons. Consequently, there is no difficulty in deciding which peaks originate from $C^\alpha H$ protons of Gly and $C^\beta H$ protons of either Ser (left hand and middle top panels of Fig. 16) or another AMX spin system such as Phe whose C^β has a similar chemical shift to the Gly C^α (right hand top panel of Fig. 16). The assignment of the Ser spin system is easily checked by examining the slices corresponding to the C^α and C^β chemical shifts of Ser (e.g. left hand and middle bottom panel of Fig. 16). In this respect, it is worth noting that in conventional ^1H–^1H correlated spectra it is often difficult to ascertain the $C^\alpha H$ and $C^\beta H$ chemical shifts of Ser for cases where the $C^\beta H$ shifts are degenerate, as the latter may lie to both low and high field of the $C^\alpha H$ shifts. In the case of the HCCH–COSY experiment, this ambiguity is easily resolved as the chemical shifts of the C^α and C^β carbons differ by 2–10 ppm, with the C^α resonance always upfield of that for C^β.

Despite the resolution afforded by the $^{13}C(F_2)$ dimension in the HCCH–COSY experiment, problems still remain with regard to the assignment of other spin systems. For example, it is frequently the case for Gln, Glu, Met and Leu spin systems that the chemical shifts of the $C^\beta H$ and $C^\gamma H$ protons are similar and sometimes degenerate. Consequently, it is often difficult to locate the $C^\beta H$–$C^\gamma H$

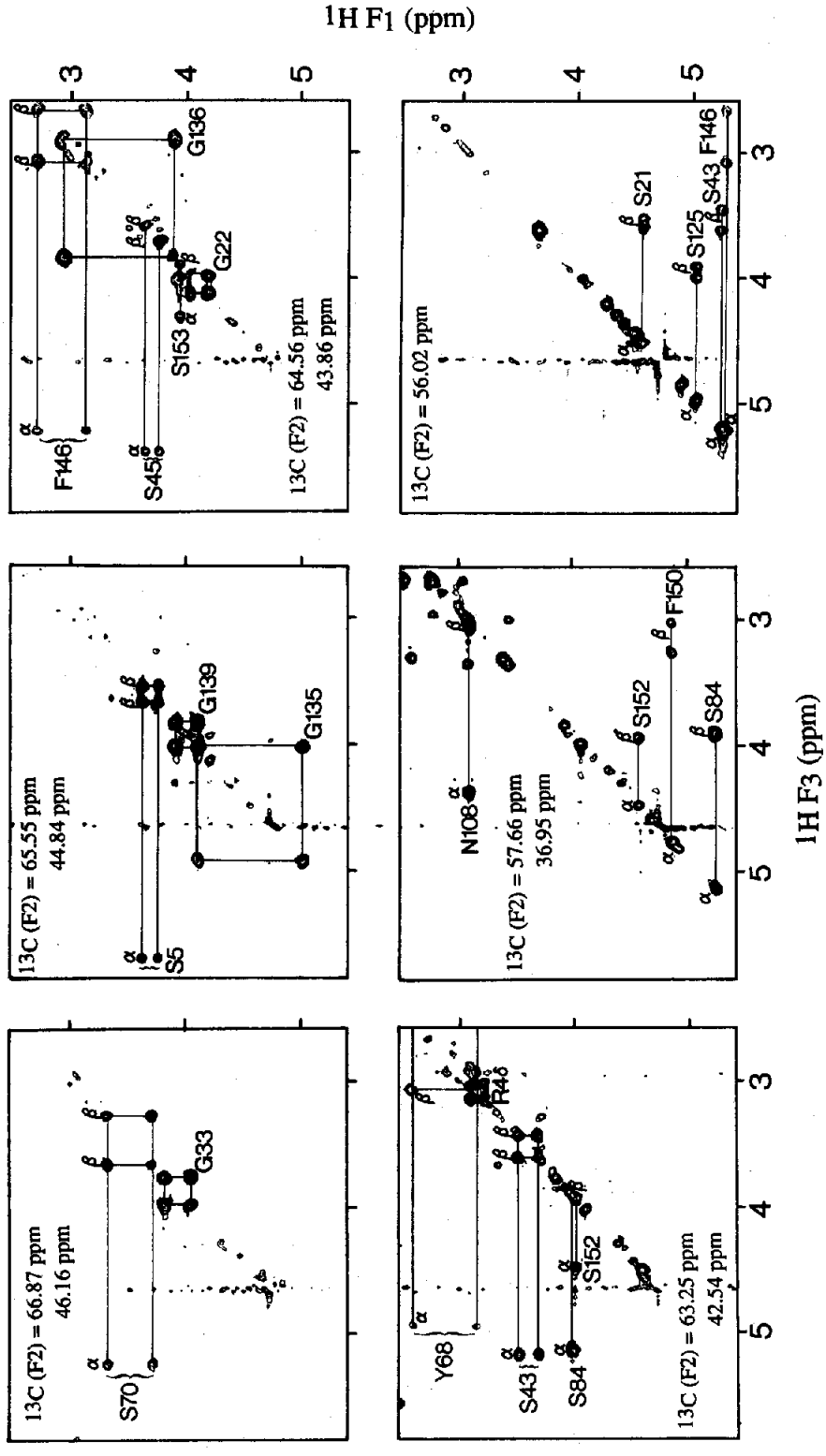

FIG. 16. Selected $^{1}H(F_3)$–$^{1}H(F_1)$ planes at different $^{13}C(F_2)$ frequencies of the 600 MHz 3D HCCH–COSY spectrum of 1.7 mM $^{13}C/^{15}N$ labelled IL-1β in D_2O, principally illustrating connectivities involving Gly and Ser residues.[41] Because extensive folding is employed, the ^{13}C chemical shifts are given by $x \pm nSW$, where x is the ppm value listed in the figure, n is an integer and SW is the spectral width (20.71 ppm).

connectivities unambiguously in the HCCH–COSY spectrum. These problems are even further exacerbated for longer side chain spin systems such as Arg, Pro and Lys. The same problem presents itself in the interpretation of regular 2D ^1H–^1H COSY type spectra, and can be circumvented by means of experiments which detect not only direct but relayed through-bond connectivities, for example relayed-COSY[49] and HOHAHA/TOCSY[50] spectroscopy. Similarly, the ambiguities present for longer side chain spin systems in the HCCH–COSY experiment can be resolved with complete confidence by recording an HCCH–TOCSY experiment in which carbon magnetization is transferred along the carbon chain by isotropic mixing.[41]

To establish conditions which are optimal for the observation of relayed connectivities in the HCCH–TCOSY experiment, the expected theoretical cross peak intensities as a function of isotropic mixing time have to be considered.[41] The rate at which magnetization is transferred from one carbon to its neighbor depends on the size of the effective J coupling, J_{eff}, present during the mixing period.[43] For coupled ^{13}C nuclei with widely different chemical shifts (e.g. Thr-C^β and C^γ), the

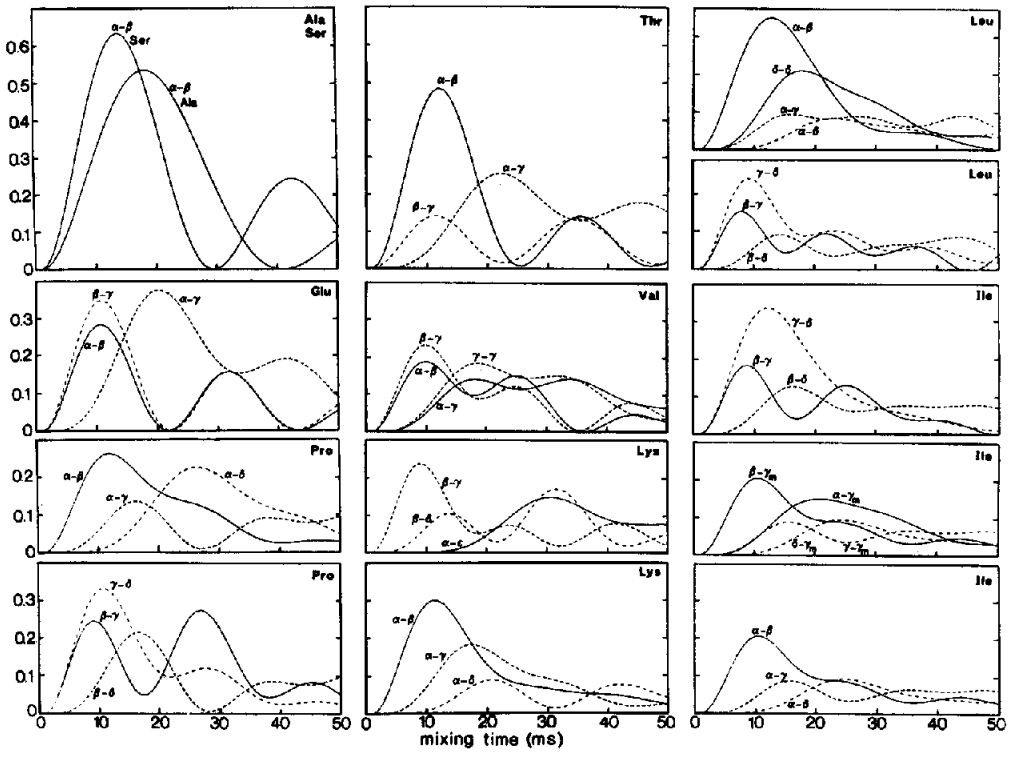

FIG. 17. Amount of net intraresidue carbon–carbon magnetization transfer occuring during the DIPSI-3 mixing period in the HCCH–TOCSY experiment, assuming a relaxation rate of ^{13}C magnetization during isotropic mixing equal to 33 s^{-1}.[41] Because J_{CC} dephasing during the δ_1, δ_2 and t_2 periods in the pulse sequence (see Fig. 14), the curves should be shifted towards the left by several ms for predicting the cross peak intensities observed in the HCCH–TOCSY spectrum. Cross-peak intensities in the HCCH–TOCSY experiment are proportional to the amount of carbon–carbon magnetization transfer, but are attenuated two-fold if one of the carbons has two magnetically inequivalent protons attached, and four-fold if both carbons have non-equivalent protons attached. The reduced effective carbon–carbon J couplings used for calculating these graphs are as follows: Ser, $J_{\alpha\beta}=35$ Hz; Ala, $J_{\alpha\beta}=25$ Hz; Thr: $J_{\alpha\beta}=20$ Hz, $J_{\beta\gamma}=35$ Hz; Glu: $J_{\alpha\beta}=30$ Hz, $J_{\beta\gamma}=33$ Hz; Val: $J_{\alpha\beta}=27$ Hz, $J_{\beta\gamma}=30$ Hz; Pro: $J_{\alpha\beta}=27$ Hz, $J_{\beta\gamma}=J_{\gamma\delta}=33$ Hz; Lys: $J_{\alpha\beta}=30$ Hz, $J_{\beta\gamma}=J_{\gamma\delta}=J_{\delta\varepsilon}=33$ Hz; Leu: $J_{\alpha\beta}=J_{\beta\gamma}=30$ Hz, $J_{\gamma\delta}=33$ Hz; Ile: $J_{\alpha\beta}=J_{\beta\gamma m}=27$ Hz, $J_{\beta\gamma}=J_{\gamma\delta}=30$ Hz. All multiple bond carbon–carbon couplings are assumed to be zero, and couplings between aliphatic and carbonyl resonances have been neglected because the large chemical shift difference between the aromatic and carbonyl nuclei on the one hand and the aliphatic carbons on the other reduces their effective J couplings to aliphatic carbons.

effective J coupling will be smaller than the real J coupling by a factor of $\sim[1-(1-\cos\phi)\cdot(8/3)^{1/2}]$ (where ϕ is the angle between the effective fields experienced by the two spins and $\phi \ll \pi/2$), resulting in a significant reduction in the rate of ^{13}C magnetization transfer.[43] Figure 17 shows the calculated fraction of net magnetization that is transferred from one carbon to another as a function of the length of the isotropic mixing period for various amino acids.[41] From analysis of these theoretical curves, it can be concluded that an isotropic mixing time in the range 20–30 ms is optimal for the observation of relayed connectivities.

Examples of different sorts of relayed connectivities observed in the 24 ms mixing time HCCH–TOCSY spectra recorded on $^{13}C/^{15}N$-labeled IL-1β are shown in Figs 18 and 19. In Fig. 18 relayed connectivities originating from the $C^{\alpha}H$ proton of a number of different amino acid spin systems are seen. Complete spin systems are clearly delineated not only for medium length side chains such as those of Glu, Gln, Met and Val, but also for the long side chains of Leu, Ile, Pro, Arg and Lys. Figure 19 shows a series of relayed connectivities for Ile spin systems starting at different positions along the chain. In virtually every case the complete spin system is delineated, thereby confirming ^1H assignments derived from connectivities starting from the $C^{\alpha}H$ protons and providing the ^{13}C chemical shifts of the other carbon atoms.[41]

3.2. *Conventional Sequential Assignment Using 3D Heteronuclear NMR*

Conventional sequential assignment relies on identifying NOE connectivities between adjacent residues involving the NH, $C^{\alpha}H$ and $C^{\beta}H$ protons.[1,2,35] The same approach can be used in heteronuclear 3D NMR,[12] making use of the 3D ^1H–^{15}N HOHAHA–HMQC experiment described in Section 3.1.1. to identify intraresidue connectivities between NH and $C^{\alpha}H$ protons, and the 3D ^1H–^{15}N NOESY–HMQC experiment[38,51-53] (Fig. 20) to identify through-space connectivities. The two experiments are very similar and differ in the mixing sequence (HOHAHA versus NOE mixing). Thus, the 3D ^1H–^{15}N NOESY–HMQC spectrum has the same appearance as the NH(F_2)–^1H(F_1) region of a conventional ^1H–^1H NOESY spectrum, except that it is spread out in a series of slices according to the ^{15}N chemical shifts. Examples of two NH(F_3)–^1H(F_1) planes of the 3D ^{15}N-separated NOESY–HMQC and HOHAHA–HMQC spectra of ^{15}N-labeled IL-1β are shown in Fig. 21, illustrating some of the most crowded regions in the 3D spectrum.[12] The massive simplification relative to the corresponding 2D spectra of the same protein shown in Fig. 1 is readily apparent.

Sequential assignment can proceed in a relatively straightforward manner by hopping from one pair of HOHAHA/NOESY planes to another pair,[38] connecting them via either $C^{\alpha}H(i)$–NH($i+1$) or NH(i)–NH($i+1$) NOEs in a manner analogous to that employed in the analysis of 2D spectra. This hopping is illustrated in Fig. 22 for a stretch of $C^{\alpha}H(i)$–NH($i+1$) sequential connectivities from Ser-45 to Gln-39 of ^{15}N-labeled IL-1β.

An alternative and simpler method of analysis can be readily conceived by selecting strips of data from each slice containing cross peaks arising from individual amide resonances, thereby eliminating the empty space that is present in 3D spectrum and the redundancy that is caused by the fact that a series of cross peaks from a single amide NH may appear in more than one slice of the 3D spectrum.[12,24] These strips are generated as follows. First the F_3(NH)–F_1(^{1}H) plane in which a set of cross peaks involving a given amide resonance are at a maximum is noted, followed by the index of the data point in the F_3(NH) dimension closest to the peak maximum of the NH resonance. Next a strip of data of width $2n+1$ points (i.e. the center point $\pm n$ data points) and containing the whole F_1(^{1}H) spectral width is extracted from the relevant slice. The width of each strip should be at least twice as wide as the base of the broadest cross peak. These strips of data are then aligned alongside each other to form one large 2D data set. Finally, for the purposes of display a $(2n+1)$ point unshifted (since)$^{3/2}$ window function is applied across each strip of data. This has the effect of removing intensity from the edges of each strip which is irrelevant to the amide in question, while leaving the absolute heights of those peaks of interest unaltered. In practice we have found that using a 0.23 ppm strip width of 17 data points combined with the (sine)$^{3/2}$ window causes little or no visible distortion of the peaks of interest within each strip.

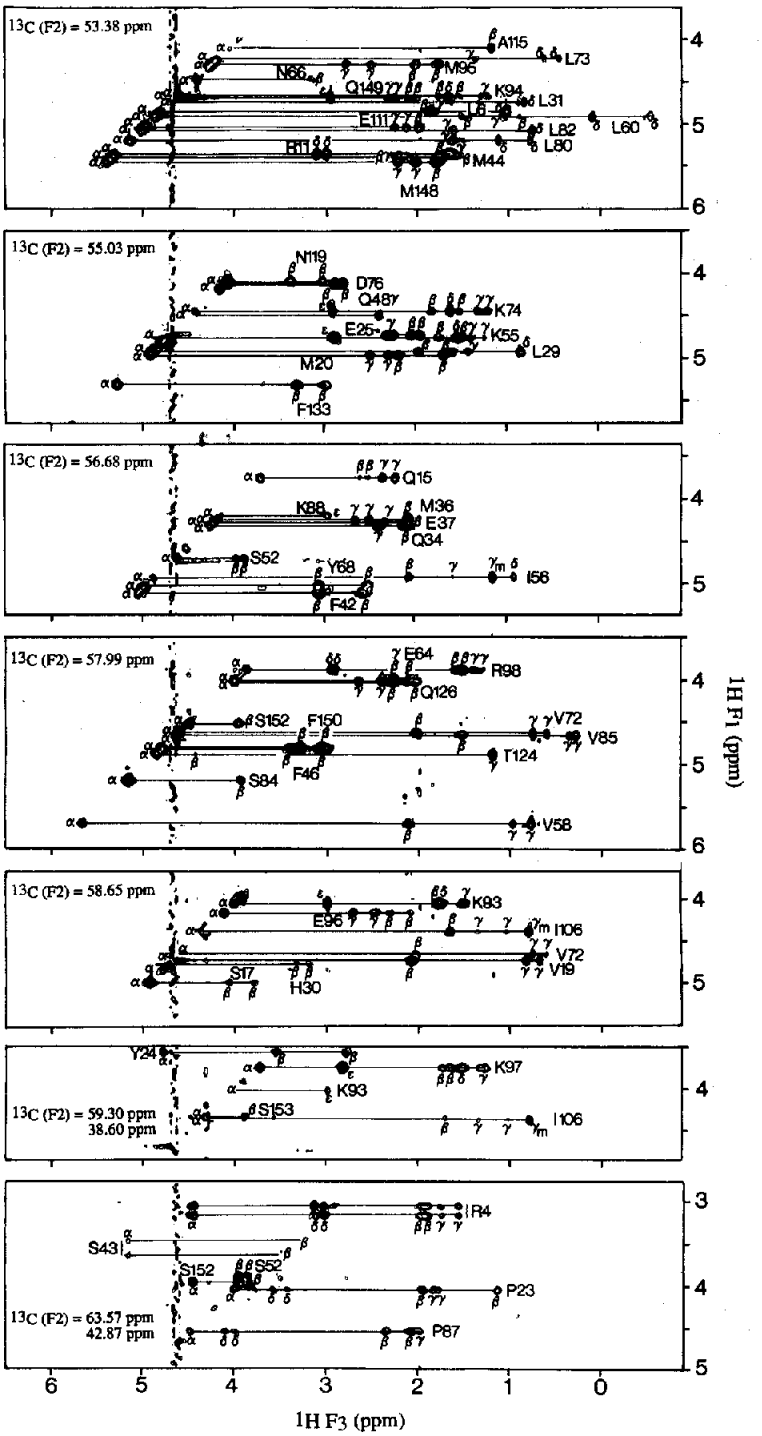

FIG. 18. Selected $^{1}H(F_3)$–$^{1}H(F_1)$ planes at different ^{13}C (F_2) chemical shifts of the 500 MHz 3D HCCH–TOCSY spectrum of 1.7 mM $^{15}N/^{13}C$ labelled IL-1β in D_2O illustrating relayed connectivities originating from the C$^{\alpha}$H proton of several longer side chain amino acid spin systems such as Glu, Gln, Met, Pro, Arg and Lys.[41]

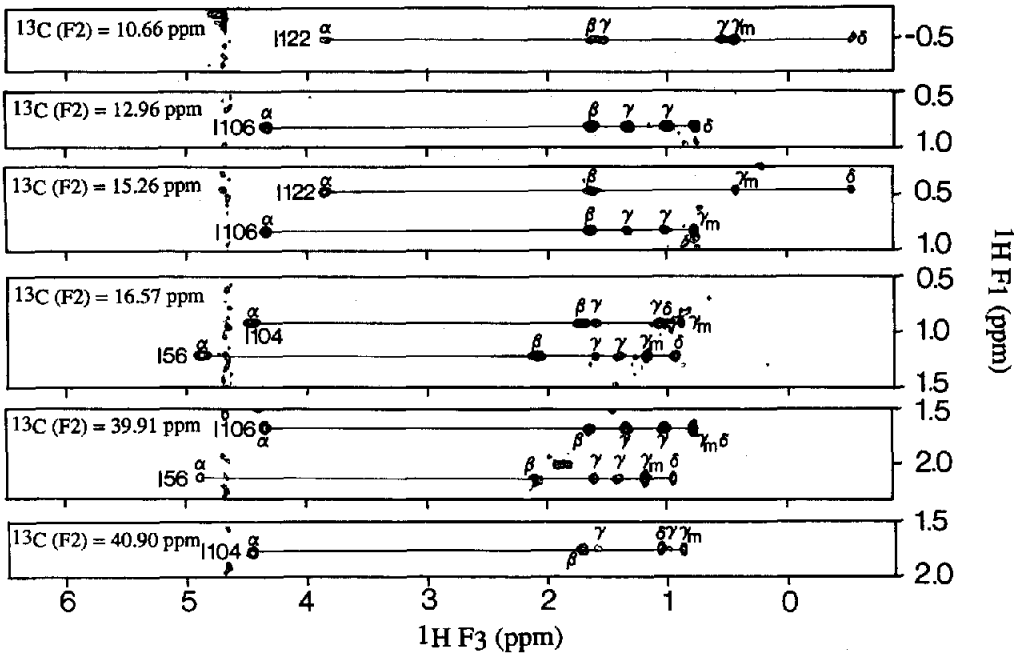

FIG. 19. Selected $^1H(F_3)$–$^1H(F_1)$ planes at different ^{13}C (F_2) chemical shifts of the 500 MHz 3D HCCH–TOCSY spectrum of 1.7 mM $^{15}N/^{13}C$ labeled IL-1β in D_2O illustrating multiple relayed connectivities originating from the $C^\delta H_3$, $C^{\gamma m}H_3$ and $C^\beta H$ protons of several Ile spin systems.[41]

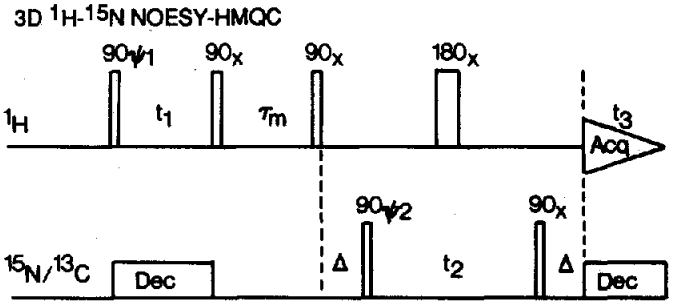

FIG. 20. Pulse sequence for the 3D ^1H–^{15}N NOESY–HMQC experiment.[38] The phase cycling is: $\psi 1 = x, -x$; $\psi 2 = 2(x), 2(-x)$; Acq = x, −x, −x, x. The delay τ is set to 4.5 ms, slightly less than $1/(2J_{NH})$. ^{15}N decoupling during t_1 and the acquisition period can be achieved using WALTZ modulation. In the case of a 3D ^1H–^{13}C NOESY–HMQC experiment,[62,63] the ^{15}N pulses can simply be replaced by ^{13}C ones, and τ is set to 3 ms, slightly less than $1/(2J_{CH})$. In practice, however, several other modifications are also desirable to reduce artifacts and t_1 noise. In particular, ^{13}C decoupling during t_1 is best achieved with a 180° ^{13}C pulse, phase cycled independently along $\pm x$ in the middle of the t_1 period; similarly the ^1H 180° pulse in the middle of the t_2 evolution period is phase cycled independently along $\pm x$; finally, a 90_x–$90_{\pm x}$ ^{13}C pulse pair is inserted at the beginning of acquisition immediately prior to the start of GARP decoupling to reduce the intensity of modulation sidebands.

Using this strip approach, it is readily possible to reduce all the information present in the 3D ^1H–^{15}N NOESY–HMQC and HOHAHA–HMQC spectra to a relatively small number of 2D plots. Initially, the ordering of the strips is obviously arbitrary and the sequential assignment strategy proceeds in exactly the same way as that used for regular 2D spectra, with the obvious and crucial

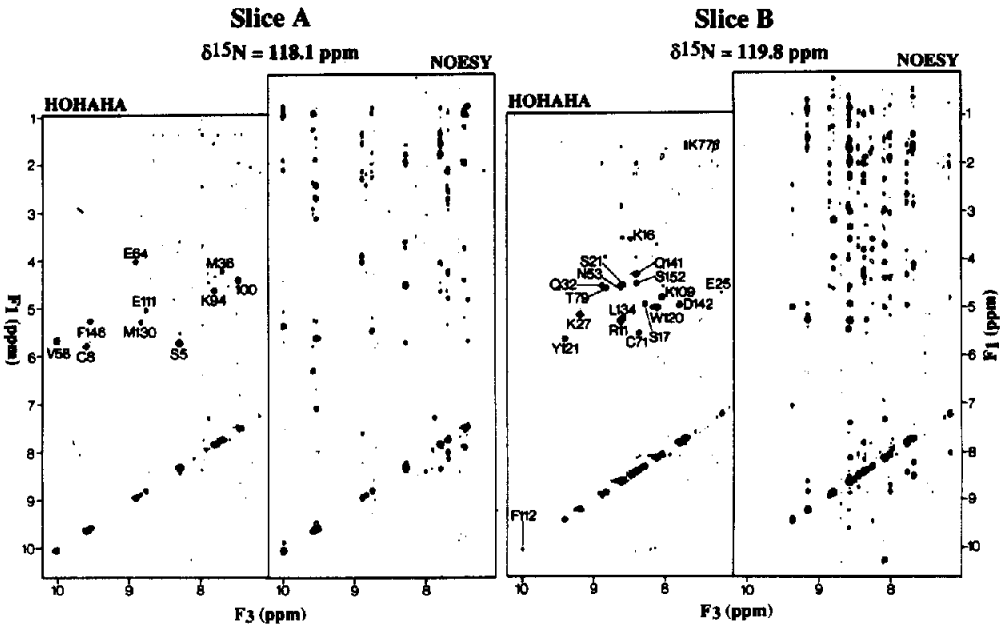

FIG. 21. The two most crowded NH(F_3)–^{1}H(F_1) planes of the 600 MHz 3D ^{1}H–^{15}N HOHAHA–HMQC and ^{1}H–^{15}N NOESY–HMQC spectra of 1.7 mM ^{15}N labeled IL-1β in 90% H_2O/10% D_2O.[12]

difference that chemical shift degeneracy and overlap involving the NH resonances is removed. Subsequent to the completion of the sequential assignment process, the strips can be reordered to be consistent with the amino acid sequence, as illustrated in Fig. 23 for the stretch of residues from Ile-104 to Glu-111 of IL-1β.[12] The top half of the figure shows the amide strips from the ^{15}N-separated HOHAHA spectrum, while the bottom half shows the corresponding set of strips from the ^{15}N-separated NOESY spectrum. The remarkable absence of cross peak overlap is readily appreciated. A number of sequential NOE connectivities are indicated by arrows, including C$^\alpha$H(i)–NH($i+1$), C$^\beta$H(i)–NH($i+1$) and NH(i)–NH($i+1$) NOEs. There are also two cases of near chemical shift degeneracy present in this section of the spectrum: namely, the NH resonances of Gln-14 and Leu-10 are just upfield from those of Lys-109 and Leu-110, respectively. Nevertheless, although the difference in NH and ^{15}N chemical shifts within these two sets of residues is small, the resolution in the 3D spectrum is still sufficient to avoid confusion.

3.3. *Sequential Assignment via Well-Resolved One-Bond and Two-Bond J Couplings*

In addition to the conventional sequential assignment approach which relies on the use of the NOE, heteronuclear 3D NMR can be employed to sequentially assign the backbone NH, ^{15}N, ^{13}C$^\alpha$, ^{13}CO and C$^\alpha$H resonances by means of heteronuclear one-bond and two-bond couplings using a number of triple resonance experiments without any absolute requirement for a knowledge of spin systems,[39] although clearly such information is very useful. This approach relies on six 3D experiments, three of which, the ^{1}H–^{15}N HOHAHA–HMQC, the H(CA)NH and the HNCA experiments, have already been described above with respect to spin system identification (Sections 3.1.1–3.1.3). The other three experiments are the 3D HNCO, HCACO and HCA(CO)N experiments.[39,40] In addition to the large one-bond ^{1}H–^{15}N and ^{1}H–^{13}C couplings, the relevant couplings used in these experiments are the one-bond ^{13}C$^\alpha$–CO (55 Hz), ^{15}N–CO ($\sim$15 Hz) and ^{15}N–^{13}C$^\alpha$ ($\sim$10 Hz) couplings, and the two-bond ^{15}N–^{13}C$^\alpha$ ($\leqslant$7 Hz) coupling. The correlations observed in these six experiments are illustrated in

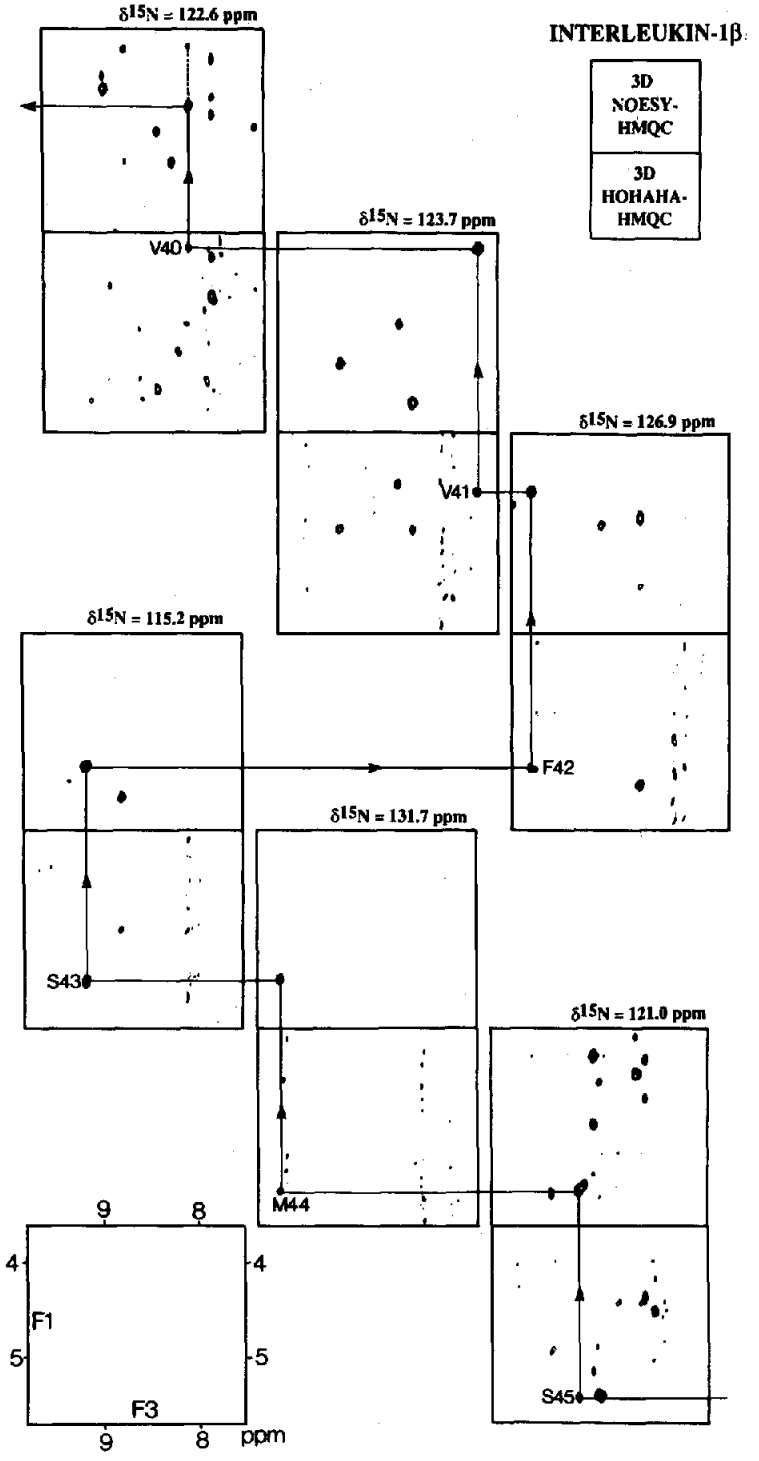

FIG. 22. Illustration of the sequential assignment procedure in ^{15}N labeled IL-1β using 3D ^{1}H–^{15}N NOESY–HMQC and HOHAHA–HMQC spectra by hopping from one ^{15}N plane to the next.[38]

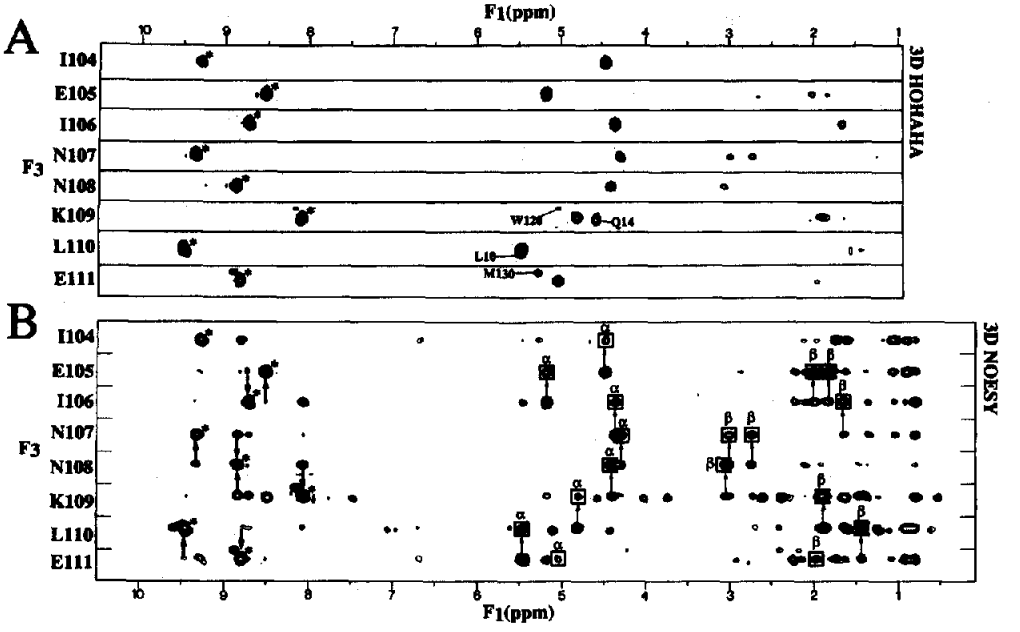

FIG. 23. Illustration of the sequential assignment procedure in ^{15}N labeled IL-1β using 3D ^{1}H–^{15}N NOESY–HMQC and HOHAHA–HMQC spectra where the empty space present in the 3D spectra has been eliminated and the relevant data from each NH(F_3)–^{1}H(F_1) plane at the different ^{15}N(F_2) frequencies has been extracted in the form of strips that are displayed as a 2D plot.[12] The 'diagonal' NH peaks are indicated by asterisks, and NH–NH, NH–C$^{\alpha}$H and NH–C$^{\beta}$H NOE cross peaks for residues Ile-104 through Glu-111 are shown.

(a)	^{1}H-^{15}N HOHAHA-HMQC	C$^{\alpha}$H(i)-^{15}N(i)-NH(i)	$^{3}J_{HN\alpha}$ (~3-11 Hz)
(b)	H(CA)NH	C$^{\alpha}$H(i)-^{15}N(i)-NH(i)	$^{1}J_{NC\alpha}$ (~7-11 Hz)
		C$^{\alpha}$H(i-1)-^{15}N(i)-NH(i)	$^{2}J_{NC\alpha}$ (~4-7 Hz)
(c)	HNCA	^{13}C$^{\alpha}$(i)-^{15}N(i)-NH(i)	$^{1}J_{NC\alpha}$ (~7-11 Hz)
		^{13}C$^{\alpha}$(i-1)-^{15}N(i)-NH(i)	$^{2}J_{NC\alpha}$ (~4-7 Hz)
(d)	HNCO	^{13}CO(i-1)-^{15}N(i)-NH(i)	$^{1}J_{NCO}$ (~15 Hz)
(e)	HCACO	C$^{\alpha}$H(i)-^{13}C$^{\alpha}$(i)-^{13}CO(i)	$^{1}J_{C\alpha CO}$ (~55 Hz)
(f)	HCA(CO)N	C$^{\alpha}$H(i)-^{13}CO(i)-^{15}N(i+1)	$^{1}J_{C\alpha CO}$ (~55 Hz)
			$^{1}J_{NCO}$ (~15 Hz)

FIG. 24. Connectivities observed in 3D triple resonance correlation experiments that can be used for sequential backbone assignments via well resolved one-bond and two-bond heteronuclear J couplings.

Fig. 24, from which it is readily apparent that there will be at least two and often three independent pathways for determining any given sequential connectivity.[39] As a practical example Fig. 25 illustrates the J correlations between Lys-21 and Asp-22 of $^{15}N/^{13}C$-labeled calmodulin used for sequential assignment, based on five of the six experiments mentioned above.[39]

3.3.1. *The 3D HNCO Experiment.* The 3D HNCO experiment (Fig. 26) correlates the NH and ^{15}N chemical shifts of residue i with the ^{13}CO shift of the preceding residue via the one-bond $^{1}J_{NCO}$

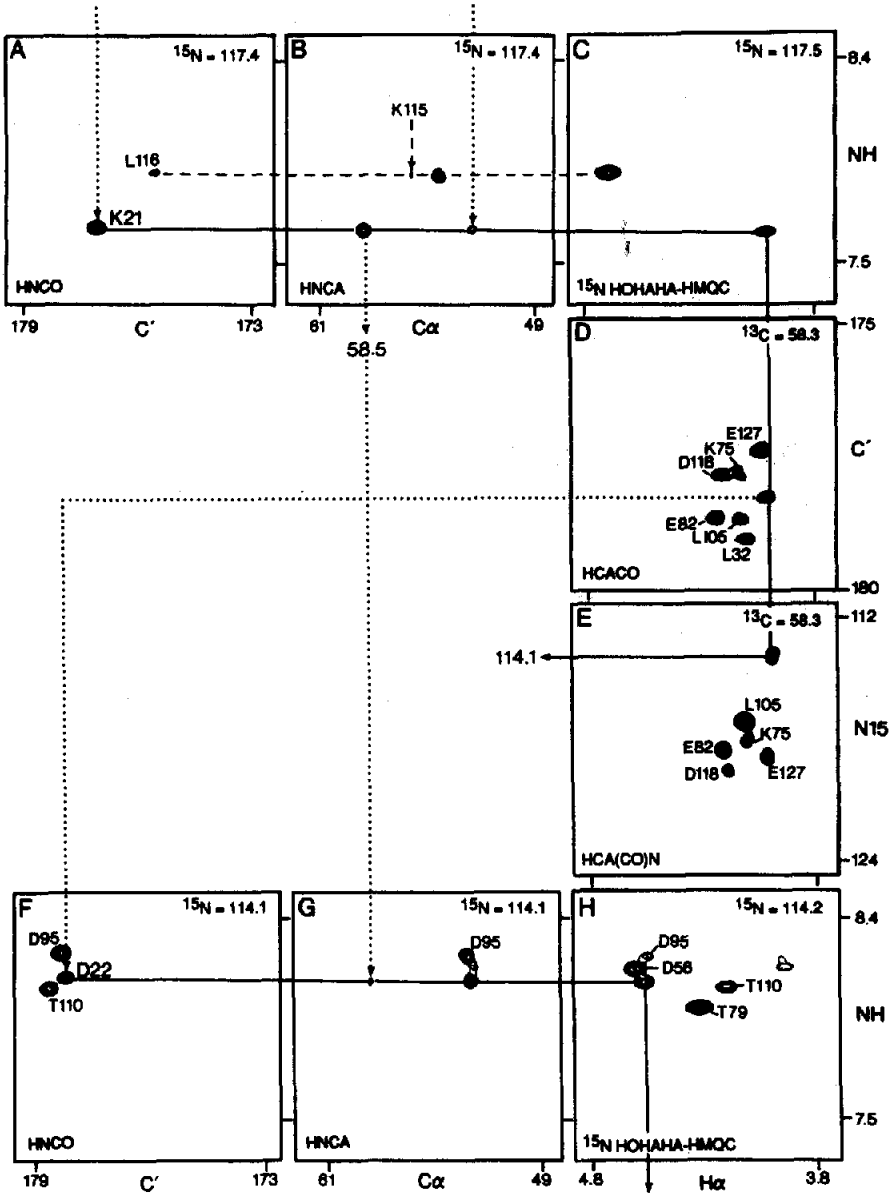

FIG. 25. Illustration of the 3D triple resonance correlation experiments to obtain sequential assignments via one-bond and two-bond heteronuclear J couplings between Lys-21 and Asp-22 of $^{15}N/^{13}C$ labeled calmodulin.[39] The 3D ^{1}H–^{15}N HOHAHA–HMQC, HNCA and HNCO experiments are recorded in H_2O, while the HCACO, and HCA(CO)N experiments are recorded in D_2O.

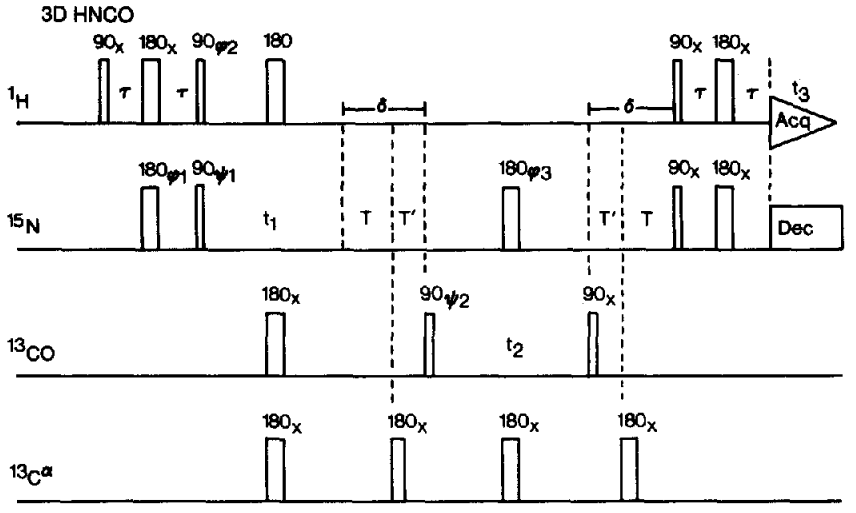

FIG. 26. Pulse sequence for the 3D HNCO experiment.[40] The phase cycling is: $\psi 1 = x$; $\psi 2 = 2(x), 2(-x)$; $\phi 1 = x, -x$; $\phi 2 = y, -y$; $\phi 3 = 4(x), 4(y), 4(-x), 4(-y)$; Acq = x, 2(−x), x, −x, 2(x), −x. Typical delays are $\tau = 2.25$ ms, slightly less than $1/(4J_{NH})$; $\delta = 18$ ms; $T = 14$ ms; and $T' = 4$ ms.

coupling (~15 Hz), thereby providing sequential connectivity information.[39] In this experiment, magnetization originating from NH protons is transferred to the directly bonded ^{15}N spins using an INEPT sequence, following which ^{15}N magnetization evolves exclusively under the influence of the ^{15}N chemical shift as a result of ^{1}H, ^{13}CO and $^{13}C^{\alpha}$ decoupling through the application of 180° pulses at the midpoint of the t_1 interval. During the delay δ, ^{15}N magnetization becomes antiphase with respect to the polarization of the carbonyl spin of the preceding residue via the $^{1}J_{NCO}$ coupling, and the subsequent 90° ^{13}CO pulse converts this magnetization into ^{15}N–^{13}CO two-spin coherence. Evolution of ^{13}CO chemical shifts then occurs during the period t_2, and the contributions of ^{15}N chemical shift and ^{1}H–^{15}N J coupling on the one hand, and of the $^{13}C^{\alpha}$–^{13}CO J coupling on the other, are removed by the application of 180° ^{15}N and $^{13}C^{\alpha}$ pulses, respectively, at the t_2 midpoint. Magnetization is finally transferred back to the NH protons by reversing the transfer steps, and detected during t_3.

In terms of the product operator formalism, the evolution of magnetization during the course of the HNCO experiment is described by[40]

$$I_z \xrightarrow{A} -2I_zN_y \xrightarrow{t_1} 2I_zN_y \cos\Omega_N t_1 \xrightarrow{B} 4N_xS_yI_z \cos\Omega_N t_1 \xrightarrow{t_2}$$

$$4N_xS_yI_z \cos\Omega_N t_1 \cos\Omega_S t_2 \cos\{\pi J_{NC\alpha}[t_2 - 2(T-T')]\}\left\{\prod_k \cos\pi J_{kCO} t_2\right\} \xrightarrow{C}$$

$$I_x \cos\Omega_N t_1 \cos\Omega_S t_2 \cos\{\pi J_{NC\alpha}[t_2 - 2(T-T')]\}\left\{\prod_k \cos\pi J_{kCO} t_2\right\}$$

where the NH, ^{15}N and CO spins are denoted by I, N and S, respectively, Ω_N and Ω_S are the ^{15}N and CO chemical shifts, $J_{NC\alpha}$ is the one-bond intraresidue ^{15}N–$^{13}C^{\alpha}$ J coupling, and J_{kCO} is the long range coupling between the carbonyl carbon and other protons, k. The detected signal, I_x, is amplitude modulated by Ω_N in the t_1 dimension and by Ω_S in the t_2 dimension, so that the cross peaks in the fully processed 3D spectrum have pure absorption lineshapes. By setting $T > T'$, the magnetization envelope in t_2 reaches a maximum value at $2(T-T')$ which is equivalent to resolution enhancement by a shifted sine bell function.

3.3.2. *The 3D HCACO Experiment.* The 3D HCACO experiment (Fig. 27) correlates the intraresidue $C^{\alpha}H$, $^{13}C^{\alpha}$ and ^{13}CO shifts.[39] Magnetization is transferred from $C^{\alpha}H$ protons to the directly bonded $^{13}C^{\alpha}$ spins via an INEPT sequence, and $^{13}C^{\alpha}$ magnetization evolves during the period t_1 under the influence of $^{13}C^{\alpha}$ chemical shift as well as the $^{13}C^{\alpha}$–^{13}CO and $^{13}C^{\alpha}$–$^{13}C^{\beta}$ J couplings, while the $C^{\alpha}H$–$^{13}C^{\alpha}$ J coupling is removed by the 180° ^{1}H pulse applied at the midpoint of t_1. Transfer of magnetization occurs next in a COSY like manner from $^{13}C^{\alpha}$ spins to ^{13}CO spins via the $^{1}J_{C\alpha CO}$ coupling by the application of simultaneous 90° $^{13}C^{\alpha}$ and ^{13}CO pulses. Evolution of ^{13}CO chemical shifts occurs during t_2 and the effects of $^{13}C^{\alpha}H$–^{13}CO and $^{13}C^{\alpha}$–^{13}CO couplings are removed by the application of 180° ^{1}H and $^{13}C^{\alpha}$ pulses at the midpoint of t_2. ^{13}CO magnetization is then transferred back to $^{13}C^{\alpha}$ by the application of simultaneous $^{13}C^{\alpha}$ and ^{13}CO pulses, at which point the $^{13}C^{\alpha}$ magnetization is anti-phase with respect to the ^{13}CO spin state. This antiphase magnetization is removed during the subsequent interval 2Δ, and finally magnetization is transferred all the way back to the $C^{\alpha}H$ spins by a reverse-INEPT sequence and detected during t_3. To minimize loss of magnetization due to relaxation and dephasing by coupling of the $^{13}C^{\alpha}$ spin to the $^{13}C^{\beta}$ spin, 2Δ should be set to $\sim 1/(3J_{C\alpha CO})$.

The evolution of magnetization in the HCACO experiment is described by[40]

$$I_z \xrightarrow{A} -2I_zA_y \xrightarrow{t_1} -4I_zA_xS_z \cos\Omega_A t_1 \sin \pi J_{C\alpha CO} t_1 \cos \pi J_{C\alpha C\beta} t_1 \xrightarrow{B}$$

$$-4I_zA_zS_y \cos\Omega_A t_1 \pi J_{C\alpha CO} t_1 \cos \pi J_{C\alpha C\beta} t_1 \xrightarrow{t_2} -4I_zA_zS_y \cos\Omega_A t_1 \sin \pi J_{AS} t_1 \cos \pi J_{C\alpha C\beta} t_1 \cos \Omega_S t_2$$

$$\xrightarrow{C} I_x \cos\Omega_A t_1 \sin \pi J_{C\alpha CO} t_1 \cos \pi J_{C\alpha C\beta} t_1 \cos\Omega_S t_2$$

where I, A and S refer to the $C^{\alpha}H$, $^{13}C^{\alpha}$ and ^{13}CO spins, Ω_A and Ω_S are the $^{13}C^{\alpha}$ and ^{13}CO chemical shifts, and $J_{C\alpha CO}$ and $J_{C\alpha C\beta}$ are the one-bond $^{13}C^{\alpha}$–^{13}CO and $^{13}C^{\alpha}$–$^{13}C^{\beta}$ couplings. As both the active

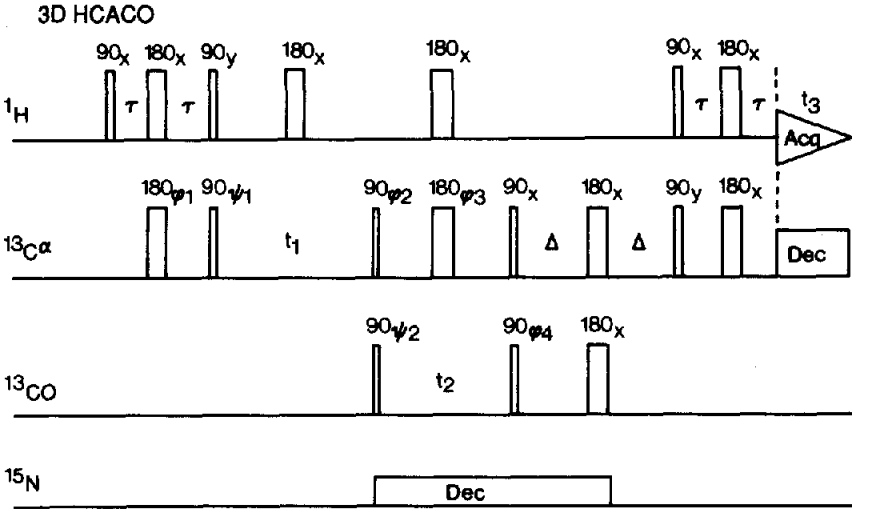

FIG. 27. Pulse sequence for the 3D HCACO experiment.[40] The phase cycling is: $\psi 1 = x$; $\psi 2 = 2(x), 2(-x)$; $\phi 1 = x, -x$; $\phi 2 = y, -y$; $\phi 3 = 4(x), 4(-x)$; $\phi 4 = 8(x), 8(-x)$; Acq = 2(x, −x, −x, x), 2(−x, x, x, −x). Typical delay durations are $\tau = 1.5$ ms, slightly less than $1/(4J_{CH})$; and $\Delta = 3$ ms. The carbonyl 90° pulses are easiest to apply as DANTE-type pulses using multiple repetitions of the cycle $\theta_{0°}$–$\theta_{300°}$–$\theta_{240°}$–$\theta_{180°}$–$\theta_{120°}$–$\theta_{60°}$. For $\theta \ll \pi$, a single cycle corresponds to a flip angle of 5.8θ, applied at an offset downfield from the carrier that equals the reciprocal duration of the cycle. The difference between the centres of the $^{13}C^{\alpha}$ and ^{13}CO regions is 121 ppm which is equal to 18.25 kHz at 600 MHz. Thus, by adjusting the duration of θ to 9.13 μs, on-resonance excitation of the ^{13}CO resonances can be accomplished without switching the frequency synthesizer.

$J_{C\alpha CO}$ and passive $J_{C\alpha C\beta}$ couplings are present during the evolution period t_1, phasing the F_1 dimension in absorption mode would result in the superposition of two antiphase F_1 doublet components. Consequently, it is advantageous in this particular experiment, to either phase the F_1 dimension in dispersive mode or use maximum entropy reconstruction to generate a single absorption signal.

3.3.3. *The 3D HCA(CO)N Experiment.* The 3D HCA(CO)N experiment (Fig. 28) provides a second source of sequential information by correlating the $C^{\alpha}H$ and $^{13}C^{\alpha}$ shifts of residue i with the ^{15}N shift of residue $i+1$.[39] The experiment is very similar to the HCACO one, except that magnetization transferred to the ^{13}CO spin in the HCACO experiment is subsequently transferred to the ^{15}N spin of residue $i+1$. This is achieved by simply including an interval $\delta \sim 0.3/J_{NCO}$ (18 ms) after the end of the t_1 period so that the ^{13}CO magnetization becomes antiphase with respect to that of the directly bonded ^{15}N spin. The subsequent ^{15}N 90° pulse generates two-spin ^{15}N–^{13}CO coherence which evolves during t_2 under the influence of the ^{15}N chemical shift only, as a 180° ^{13}CO pulse refocuses the effects of both ^{13}CO chemical shifts and ^{13}CO–$^{13}C^{\alpha}$ J coupling. At the end of the t_2 period, magnetization is transferred back to the $C^{\alpha}H$ protons by reversing the transfer steps and detected during t_3.

The evolution of magnetization during the course of the HCA(CO)N experiment can be described by[40]

$$I_z \xrightarrow{A} -2I_zA_y \xrightarrow{t_1} -4I_zA_xS_z\cos\Omega_A t_1 \sin\pi J_{C\alpha CO} t_1 \cos\pi J_{C\alpha C\beta} t_1 \xrightarrow{B}$$

$$-8I_zA_zS_xN_y\cos\Omega_A t_1 \sin\pi J_{C\alpha CO} t_1 \cos\pi J_{C\alpha C\beta} t_1 \xrightarrow{t_2}$$

$$-8I_zA_zS_xN_y\cos\Omega_A t_1 \sin\pi J_{C\alpha CO} t_1 \cos\pi J_{C\alpha C\beta} t_1 \cos\Omega_N t_2 \xrightarrow{C}$$

$$I_x\cos\Omega_A t_1 \sin\pi J_{C\alpha CO} t_1 \cos\pi J_{C\alpha C\beta} t_1 \cos\Omega_N t_2$$

where the notation is the same as that used in Section 3.3.2 for the HCACO experiment, and N refers to the ^{15}N spin of the $(i+1)$ residue. Just as in the HCACO experiment, the pure phase absorption signal in the F_1 dimension comprises a pair of antiphase doublets, so that the F_1 dimension is best phased in dispersion mode.

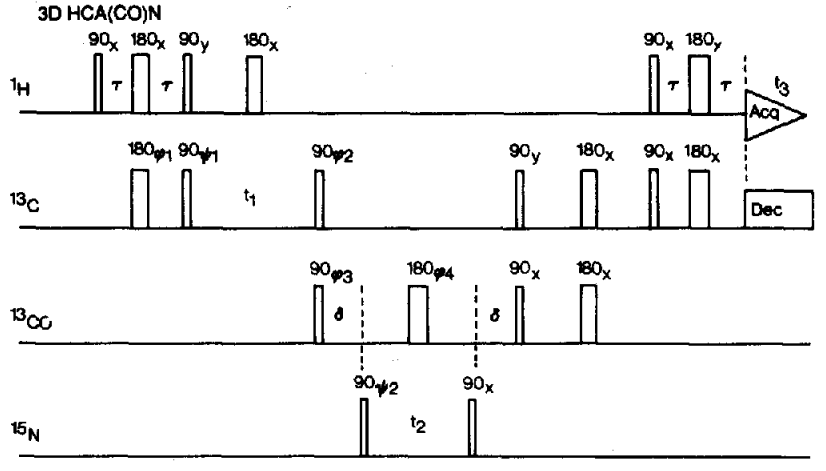

FIG. 28. Pulse sequence for the 3D HCA(CO)N experiment.[40] The phase cycling is: $\psi 1 = x$; $\psi 2 = 4(x), 4(-x)$; $\phi 1 = x, -x$; $\phi 2 = y, -y$; $\phi 3 = 2(x), 2(-x)$; $\phi 4 = 8(x), 8(y), 8(-x), 8(-y)$; Acq = x, 2(−x), x, −x, 2(x), 2(−x), 2(x), −x, x, 2(−x), x. Typical delay durations are $\tau = 1.5$ ms, slightly less than $1/(4J_{CH})$; $\Delta = 3$ ms; and $\delta = 18$–20 ms. Carbonyl pulses can be applied as DANTE type pulses in the same manner as for the HCACO experiment (cf. Fig. 27).

4. OTHER USEFUL HETERONUCLEAR 3D NMR EXPERIMENTS

In this section, we will discuss three other useful 3D NMR pulse sequences related to the identification of through-space interactions, namely the ^{15}N and ^{13}C-separated ROESY–HMQC[45, 55] and the ^{1}H–^{15}N HMQC–NOESY–HMQC[56, 57] experiments. The two former experiments are useful for distinguishing NOEs from chemical exchange effects and for effectively removing distortions in cross peak intensities due to spin-diffusion. The latter experiment is useful for detecting NOEs between NH protons with degenerate chemical shifts.

4.1. *The 3D ^{1}H–^{15}N ROESY–HMQC Experiment*

The main use for this particular experiment in protein NMR lies in detecting NOEs between NH protons and bound water. In addition, it provides an accurate assessment of intraresidue interproton distances between the NH, $C^{\alpha}H$ and $C^{\beta}H$ protons. The rationale behind the experiment is that in the rotating frame, NOEs (which are now referred to as ROEs) and chemical exchange peaks are of opposite sign, in contrast to laboratory frame experiments, where all such interactions give rise to cross peaks of the same sign and hence are indistinguishable.[58]

To detect bound water in this manner, a method of water resonance suppression must be employed which does not interfere with the observation of ROEs between NH protons and bound water molecules. As alluded to in Section 2.3 this can be achieved fairly easily, and the pulse scheme is shown in Fig. 29.[55] After the evolution of ^{1}H chemical shifts in t_1, a spin lock pulse, typically set to the length of the spin-locked relaxation time $T_{1\rho}$ of the amide protons for optimal signal-to-noise, is applied along the y axis and causes mixing of ^{1}H magnetization through chemical exchange and ROE effects (as well as some Hartmann–Hahn effects). At this stage, ^{1}H magnetization is aligned along the effective field, in the yz plane, close to the y axis. After dephasing caused by the ^{15}N–^{1}H J coupling during the time period $2\tau \sim 1/(2J_{NH})$, all magnetization residing on ^{15}N-attached protons is subsequently converted into ^{1}H–^{15}N multiple quantum coherence by the application of a ^{15}N 90° pulse. Magnetization from protons not attached to ^{15}N, on the other hand, remains aligned along the y axis at the end of the interval 2τ. This includes the large water magnetization which needs to be suppressed. By applying a short ($\sim$2 ms) ^{1}H trim pulse along the x axis, this magnetization is effectively removed by randomization.[59] As a result, the necessity for presaturation of the water resonance, with the concomitant perturbation of ROE effects between water and ^{15}N-attached protons, is avoided. During the evolution period t_2, ^{1}H offset effects are suppressed by the 180° ^{1}H pulse, and multiple quantum coherence evolves with the ^{15}N chemical shift frequency. At the end of the t_2 period, multiple quantum coherence is converted back into observable magnetization. To ensure indentical amounts of z magnetization at the start of every sequence, a trim pulse is applied along the x axis immediately after acquisition.

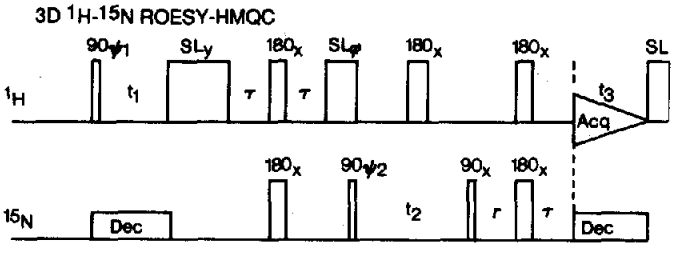

FIG. 29. Pulse sequence for the ^{1}H–^{15}N ROESY–HMQC experiment.[55] The phase cycling is as follows: $\psi 1 = x, -x$; $\psi 2 = 2(x), 2(-x)$; $\phi = 4(x), 4(-x)$, Acq = 2(x, −x, −x, x). ROESY mixing is achieved by a spin lock along the y axis (SL_y). The two other spin lock pulses (SL_ϕ and SL), related to water suppression, are applied for only 2 ms. The delay τ is set to 2.25 ms, slightly less than $1/(4J_{NH})$.

Using the pulse sequence outlined above, cross peaks may arise from one of three sources.[55] Negative cross peaks (of opposite sign to the diagonal peaks at $\delta F_1 = \delta F_3$) arise from NOEs in the rotating frame (i.e. ROEs). Chemical exchange, on the other hand, as well as Hartman–Hahn effects, give rise to positive cross peaks. The latter will only be observed when the matching for homonuclear Hartmann–Hahn transfer is near perfect, that is to say when the two ^{1}H spins have opposite but approximately equal offsets from the transmitter.

Negative ROE cross peaks between NH protons and bound water can arise through two different mechanisms.[55, 60] The first involves solely an ROE and is due to the close proximity of the NH proton and the bound water molecule. The second involves an indirect pathway whereby magnetization is transferred by an ROE from an NH proton to a rapidly exchanging side chain proton (i.e. hydroxyl group of Ser, Thr and Tyr, the side chain amide group of Asn, Gln and Lys, and the guanidinium group of Arg), followed by chemical exchange between the latter proton and water. Providing the three-dimensional structure of the protein under consideration is known, it is easy to assess the possible contribution of this indirect magnetization transfer pathway.

The application of the 3D ^{1}H–^{15}N ROESY–HMQC experiment is illustrated in Fig. 30 which shows several NH(F_3)–F_1(^{1}H) planes at different ^{15}N frequencies of the spectrum of ^{15}N-labeled IL-1β.[55] Seven ROE cross peaks between NH protons in the F_3 dimension and the water frequency in the F_1 dimension are clearly seen in Fig. 30, and in total, 17 such cross peaks were identified in the complete data set, of which 15 could be unambiguously attributed to ROEs between NH protons and bound water.

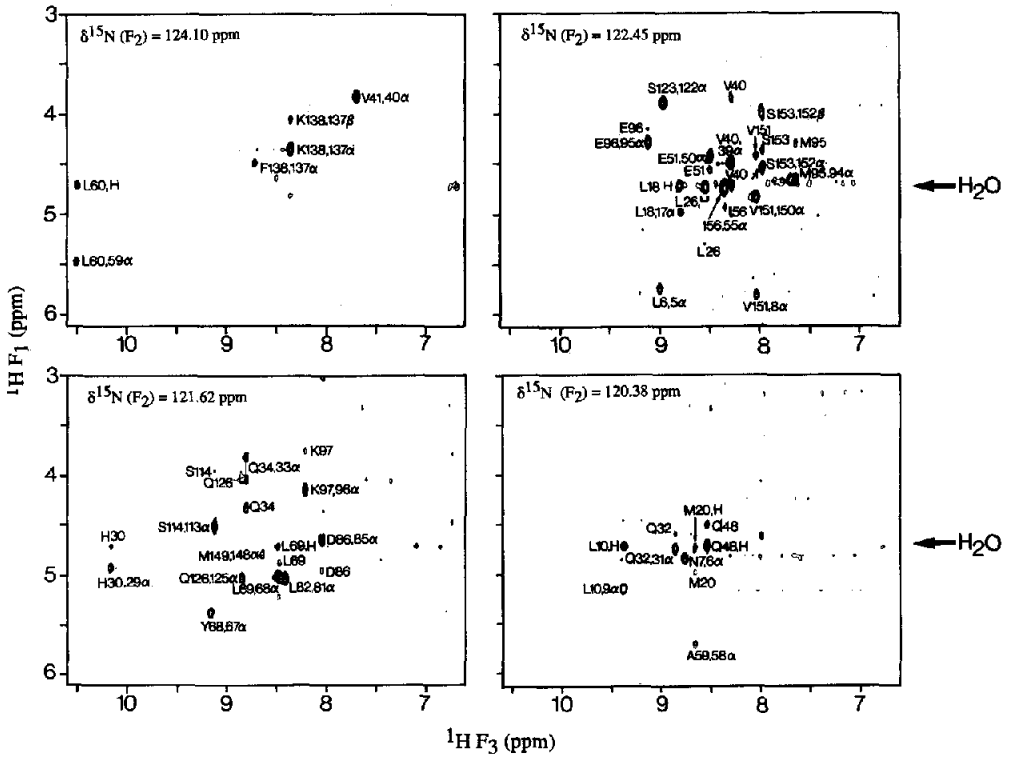

FIG. 30. Four out of 64 (F_1, F_3) slices of the 600 MHz 3D ^{1}H–^{15}N ROESY–HMQC spectrum of 1.7 mM ^{15}N labeled IL-1β in 90% H_2O/10% D_2O.[55] Peaks are labeled i, j, where i refers to the NH proton (with the residue name and number indicated), and j refers either to water (indicated by the letter H) or an aliphatic proton (indicated by the residue number and the proton type). The water frequency is at 4.67 ppm.

4.2. *The 3D ^1H–^{13}C ROESY–HMQC Experiment*

The pulse scheme for the ^{13}C-separated ROESY–HMQC experiment is relatively straightforward and shown in Fig. 31.[45] The main use of this particular experiment is to assess the relative intensities of intraresidue ROEs between $C^\alpha H$ and $C^\beta H$ protons for the purposes of stereospecific assignment of β-methylene protons. Consequently, it is essential to place the ^1H carrier frequency to low field of the $C^\alpha H$ resonances to avoid artifacts from Hartmann–Hahn transfer between $C^\alpha H$ and $C^\beta H$ protons in cases where the matching for this process is near perfect. In order to optimize resolution in the F_1 dimension, it is advisable to keep the F_1 spectral width to a minimum. In practice, this can be achieved by using a spectral width equal to the aliphatic region of the spectrum and shifting the carrier prior to Fourier transformation. Provided either the States or States–TPPI methods have been used for quadrature detection in F_1, this is easily achieved by applying a linear phase correction to the time domain data in t_1 given by $\Delta\nu/SW \times$ number of complex points $\times 360°$, where SW is the spectral width and $\Delta\nu$ is the required carried shift.[24, 61]

In principle, the $C^\alpha H$–$C^\beta H$ NOE cross peak intensities could also be obtained from a short mixing time 3D ^{13}C-separated NOESY–HMQC spectrum.[62, 63] In practice, however, it is difficult to obtain such a spectrum as the diagonal resonances, at mixing times short enough to avoid spin diffusion, are very intense resulting in substantial amounts of t_1 noise which obscure many of the weaker cross peaks.[45] Because the ROE is positive for all values of the molecular correlation time τ_c, indirect ROE contributions are of opposite sign relative to direct ROE effects in the case of one intervening spin, and positive indirect effects involving an even number of intermediate spins are generally not observable because positive and negative contributions tend to cancel out one another.[58, 64] As a result, ROESY spectra recorded with reasonably long mixing times still provide a faithful representation of internuclear distances not only for small proteins and oligonucleotides, but more importantly for larger proteins as well.[55, 65]

The optimal value of the ROESY mixing period is equal to the approximate average value of the spin-locked relaxation time $T_{1\rho}$,[58, 66] and at such mixing times, the diagonal resonances are significantly attenuated, and reasonably strong cross peaks can be readily observed. This is illustrated by several $^1H(F_3)$–$^1H(F_1)$ planes of the ^{13}C-separated ROESY–HMQC spectrum of $^{13}C/^{15}N$ labeled IL-1β shown in Fig. 32.[45] As a consequence of the short mixing time (<25 ms for a protein of ~18 kDa), interproton distances larger than about 3.5 Å do not give rise to observable ROE effects.[45, 55]

4.3. *The 3D ^1H–^{15}N HMQC–NOESY–HMQC Experiment*

In the case of the heteronuclear-separated NOESY experiments described so far in this review, it is impossible to observe NOEs between protons with degenerate chemical shifts. Such interactions occur

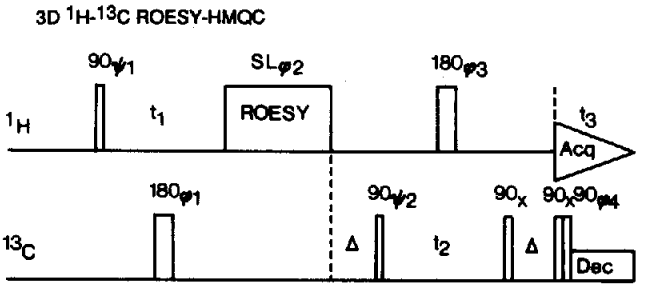

FIG. 31. Pulse sequence for the ^1H–^{13}C ROESY–HMQC experiment.[45] The phase cycling is: $\psi 1 = 4(x), 4(y)$; $y2 = x, -x$; $\phi 1 = 4(x), 4(-x)$; $\phi 2 = 4(y), 4(-x), 4(-y), 4(x)$; $\phi 3 = 2(x), 2(y), 2(-y), 2(x), 2(-x), 2(-y), 2(y), 2(-x)$; $\phi 4 = 8(x), 8(-x)$; Acq = x, 2(−x), x, y, 2(−y), y. The ^{13}C $180_{\phi 1}$ pulse is a composite 180° pulse of the type $90_x180_y90_x$. SL_{ϕ_2} is the ROESY spin lock. The delay Δ should be set to ~3 ms, slightly less than $1/(2J_{CH})$. ^{13}C decoupling during the acquisition period is achieved using coherent decoupling, and the ^{13}C $90_x90_{\phi 4}$ pulse pair at the beginning of acquisition prior to the start of decoupling reduces the intensity of modulation side bands.

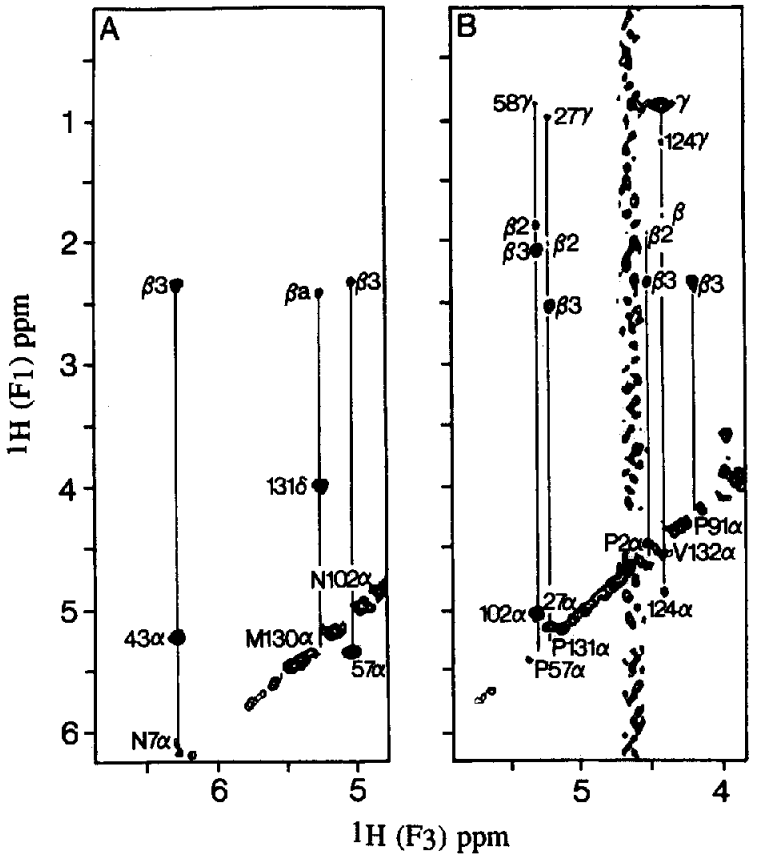

FIG. 32. Two $^1H(F_1)$–$^1H(F_3)$ planes at different ^{13}C frequencies of the 600 MHz 3D ^{13}C-separated ROESY–HMQC spectrum of 1.7 mM $^{13}C/^{15}N$ labeled IL-1β in D_2O recorded with a 22 ms mixing time.[45] (A) $\delta^{13}C = 51.4 (\pm nSW)$ ppm; (B) $\delta^{13}C = 61.9$ $(\pm nSW)$ ppm. (The spectral width SW is 20.71 ppm). Only positive levels are shown and diagonal resonances are therefore not observed. Note that in addition to intraresidue ROEs, a number of both short and long-range interresidue ROEs are also seen in both slices.

repeatedly, both among aliphatic and aromatic protons, and between sequential amide protons in helical proteins. Providing the chemical shifts of the directly bonded heteronuclei are not degenerate, NOEs between degenerate protons can be detected in a 3D spectrum in which the heteronuclear chemical shifts are labeled in the F_1 and F_2 dimensions, and the ^1H chemical shift in the F_3 dimension. In the case of NOEs involving NH protons the 3D ^1H–^{15}N HQMC–NOESY–HMQC experiment yields the necessary information.[56, 57] The pulse scheme is shown in Fig. 33.[56] Briefly, heteronuclear multiple quantum coherence is generated during the t_1 period which is subsequently converted back into transverse magnetization. Thus, at the end of the t_1 period, ^1H magnetization is modulated by the shift of its attached ^{15}N nucleus. During the subsequent NOESY mixing period τ_m, ^1H magnetization is transferred to its immediate spatial neighbors. At the end of τ_m, NH magnetization is converted back into heteronuclear multiple quantum coherence during t_2, before being detected during t_3. Obviously, the same pulse sequence can be used to detect NOEs between aliphatic or aromatic protons with degenerate chemical shifts by replacing the ^{15}N pulses with ^{13}C pulses.

Two ^{15}N (F_2)–^{15}N (F_1) planes and one $NH(F_3)$–$^{15}N(F_1)$ plane of the 3D HMQC–NOESY–HMQC spectrum of ^{15}N-labeled calmodulin are shown in Fig. 34.[56] In the slices taken perpendicular to the F_3 axis, the F_1 and F_2 coordinates are those of the ^{15}N atoms bonded to the originating and

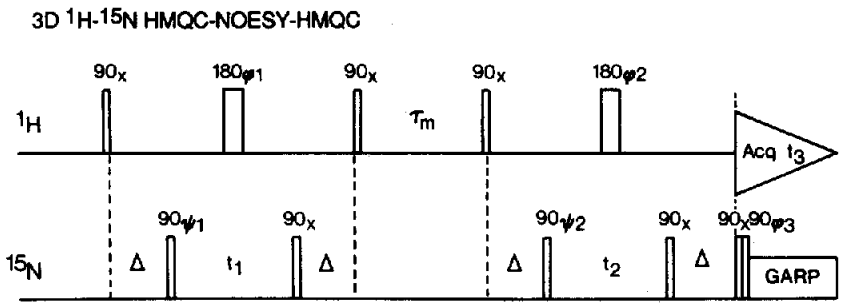

FIG. 33. Pulse scheme for the 3D ^{1}H–^{15}N HMQC–NOESY–HMQC experiment.[56] Phase cycling is as follows: $\psi 1 = x, -x$; $\psi 2 = 2(x), 2(-x)$; $\phi 1 = 4(x), 4(y), 4(-x), 4(-y)$; $\phi 2 = 8(x), 8(y), 8(-x), 8(-y)$; $\phi 3 = x, -x$; Receiver = $(x, -x, -x, x), 2(-x, x, x, -x), (x, -x, -x, x)$. The delay Δ should be set to 4.5 ms, slightly less than $1/(2J_{NH})$. ^{15}N decoupling during acquisition is achieved using coherent ^{15}N GARP modulation and the 90_x–$90_{\rho 3}$ ^{15}N pulse pair immediately prior to the start of GARP decoupling serves to reduce the intensity of modulation sidebands.

destination protons, respectively. Thus, in the case of NH protons with different chemical shifts, the NOE cross peaks appear in only one half of the spectrum in a given (F_1, F_2) slice (i.e. for an NOE interaction between amide protons A and B, one NOE appears in the plane $F_3 = \delta$A, and the other one in the slice with $F_3 = \delta$B). For NOEs involving NH protons with the same chemical shifts, on the other hand, the cross peaks occur symmetrically about the diagonal in the same (F_1, F_2) plane. Two such NOEs are illustrated in Fig. 34, namely between the NH protons of Met-76 and Lys-77, and between the NH protons of Met-144 and Met-145.

5. IDENTIFICATION OF LONG RANGE NOE CONNECTIVITIES: HETERONUCLEAR 4D NMR

The 3D heteronuclear experiments described in Sections 3 and 4 have proved very successful in obtaining complete ^{1}H, ^{15}N and ^{13}C resonance assignments for proteins of 17–20 kDa, the first example of which is provided by IL-1β.[12, 41, 67] The key to 3D protein structure determination, however, lies not simply in obtaining resonance assignments, but in identifying as many short (< 5 Å) interproton contacts (i.e. NOEs) as possible.[4, 6] Particularly important are NOEs between residues far apart in the sequence but close together in space as they provide the crucial information needed to determine the polypeptide fold. Experience with IL-1β indicates that, although 3D ^{15}N or ^{13}C-separated NOESY–HMQC experiments can be used to assign a fair number of long range NOEs, a still larger number is difficult to assign unambiguously owing to extensive spectral overlap.[12, 67, 68] Indeed, in the case of IL-1β, it was not possible to assign a large enough number of NOEs from such spectra to allow the determination of a high resolution structure of the quality now attainable for smaller proteins,[7–11] although the information content was sufficient to obtain a low resolution structure.[68] The solution to this impasse lies in extending the dimensionality of the NMR spectra still further to four dimensions.[13, 69] In this regard, there are two 4D experiments which play the pivotal role in obtaining the necessary interproton distance restraints required for high resolution structure determinations of larger proteins, namely the 4D ^{13}C/^{15}N- and ^{13}C/^{13}C-edited NOESY experiments. Once complete assignments are available from the range of 3D double and triple resonance experiments described above, these 4D experiments permit the straightforward assignment of virtually all NOEs, as problems associated with resonance overlap are completely (or almost completely) eliminated.

5.1. *Processing of 4D Spectra*

In order to keep the measuring time down to reasonable limits, it is necessary to use rather limited digital resolution. Consequently, it is often crucial to extend these severely truncated signals by linear

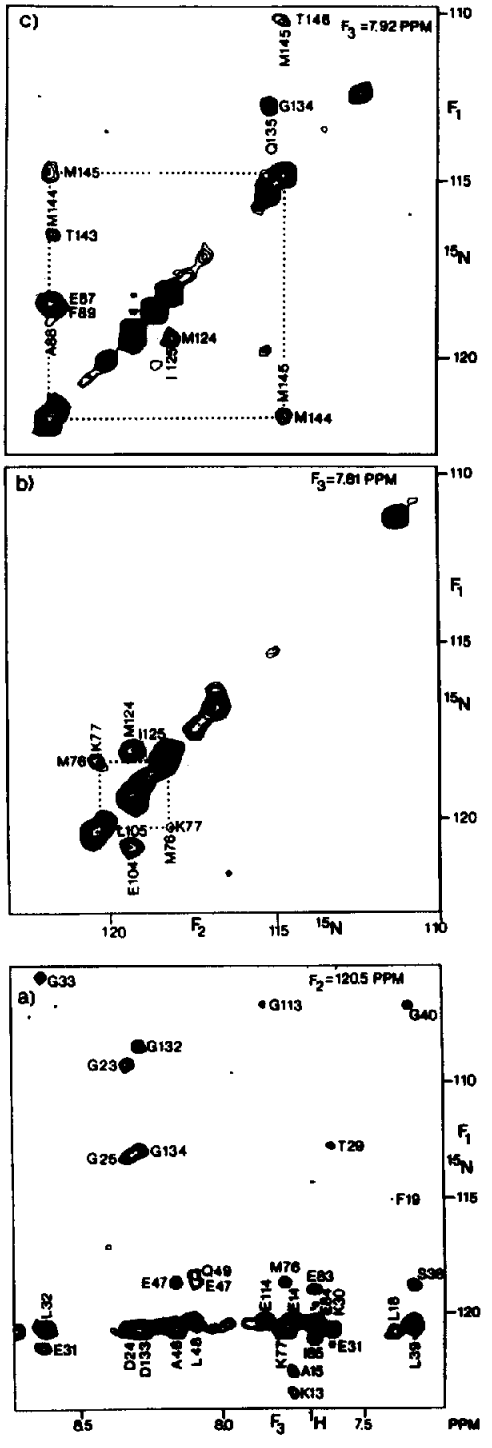

FIG. 34. One selected $^{15}N(F_1)$–$^{1}H(F_3)$ slice (A), and two selected $^{15}N(F_1)$–$^{15}N(F_2)$ slices at different $^{1}H(F_3)$ chemical shifts (B and C) of the 600 MHz 3D ^{1}H–^{15}N HMQC–NOESY–HMQC spectrum of 1.5 mM ^{15}N-labeled calmodulin in 90% H_2O/10% D_2O.[56] The NOE mixing time τ_m is 140 ms.

prediction.[70] This entails the use of a more complex processing scheme than would otherwise be the case if only conventional Fourier transformation was employed. The simplest scheme to implement is one in which linear prediction is performed one dimension at a time.[71] This means that the number of frequency components present in the time domain data which one wants to extend, must be minimized. To this end Fourier transformation is carried out in all the other dimensions prior to linear prediction of the dimension of interest.

Consider, the case of the $^{13}C/^{13}C$-edited NOESY experiment, for example, in which ^{13}C chemical shifts are recorded in t_1 and t_3 with very limited digital resolution (e.g. 8 complex data points), and ^1H chemical shifts in t_2 and t_4. A flowchart of the processing scheme used to extend the data in the t_1 and t_3 dimensions is shown in Table 2.[69] Briefly, the t_3 dimension is transformed first, followed by processing of the t_2 and t_4 dimensions with appropriate digital filtering, zero-filling, Fourier transformation and phasing. The imaginary parts in F_2 and F_4 are discarded at the end of this stage. The t_1 dimension is then extended by linear prediction, followed by digital filtering, zero filling, Fourier transformation and phasing. Subsequently the imaginary parts in t_1 are discarded. Finally, the resolution in the t_3 dimension is increased by a procedure involving inverse Fourier transformation, followed by linear prediction, digital filtering, zero-filling, forward Fourier transformation and phasing in t_3.

In considering linear prediction for the processing of 3D data, it is worth noting a number of additional features that can be used to improve the reliability and efficiency of the method. First, as it is generally desirable to extend the data in the severely truncated dimensions by a factor of 2, it is essential to treat the data as complex numbers,[69, 72] rather than predicting the real and imaginary parts separately.[73] Second, it is necessary to use a process known as root reflection[74] to ensure that the predicted part of the time domain data does not increase in amplitude.[75] This simply involves calculating the root of an nth-order polynomial where n is the number of prediction coefficients. Third, the negative time behavior can be calculated giving a doubling of the size of the time domain data used as input for the linear prediction algorithm.[75] This can be done by delaying the sampling in the dimensions to be extended by exactly half a dwell time so that, neglecting signal decay and using the fact that at time zero the signal phase is zero, the data at negative time are the complex conjugates of the data recorded at positive time.[75] Thus, for a data point x_n at positive time, the corresponding point at negative time is given by $x_{-n}=x_n^*$. As the noise is correlated for both positive and negative time domain points, no additional signal is generated by this procedure.[69] It does, however, result in an increase by a factor of 2 in the number of time domain data points that can be used for linear prediction, thereby effectively doubling the number of frequency components that can be extracted from the data.[69, 75] In practice, for $2N$ data points (including the negative time domain data), $K=N-2$ prediction coefficients can safely be used, resulting in $N+2$ linear equations. As a result, the unknown frequency and amplitude of each unknown signal component can be determined with greater accuracy.

Typically we use 256 real points in the $t_4(^1H)$ acquisition dimension, 64 complex points in the $t_2(^1H)$ dimension, and only 8 complex points in the t_1 and t_3 (heteronuclei) dimensions.[69] After extending the F_1 and F_3 dimensions to 16 complex points by linear prediction and zero filling in all dimensions, the final absorptive portion of the fully processed spectrum comprises a $32\times128\times32\times256$ data point

TABLE 2. Flowchart of the steps used in processing 4D $^{13}C/^{15}N$ and $^{13}C/^{13}C$-edited NOESY data sets[69]

Step	Computation performed
1	Fourier transform in t_3 (^{13}C or ^{15}N) dimension
2	Processing of the [$t_2(^1H)$, $t_4(^1H)$] planes
3	Linear prediction of t_1 (^{13}C) time domain
4	Processing of t_1 (^{13}C) dimension
5	Inverse Fourier transform in t_3 (^{13}C or ^{15}N)
6	Linear prediction of t_3 (^{13}C or ^{15}N) time domain
7	Processing of t_3 (^{13}C or ^{15}N) dimension

matrix. Thus for 4 scans per increment, a 4D spectrum can potentially be recorded in as little as 1.5 days.

5.2. *The 4D $^{13}C/^{15}N$-Edited NOESY Experiment*

In the 3D ^{1}H–^{15}N NOESY–HMQC experiment NOEs between NH protons and aliphatic protons are spread into a third dimension by the chemical shift of the directly bonded ^{15}N atoms.[13] While this 3D experiment effectively removes, in all but a very few cases, chemical shift degeneracy associated with the NH protons, it leaves ambiguities associated with severe overlap of the aliphatic protons unaffected. Thus, even if a cross peak connecting an aliphatic and amide proton is well resolved in the 3D spectrum, it is frequently not possible, with the exception of cases involving the $C^{\alpha}H$ resonances, to identify conclusively the aliphatic proton involved on the basis of its ^{1}H chemical shift. This problem can be overcome by introducing a fourth dimension comprising the chemical shift of ^{13}C spins directly bonded to the aliphatic protons.

The pulse scheme for the 4D $^{13}C/^{15}N$-edited NOESY experiment is shown in Fig. 35 and comprises three separate 2D experiments, namely ^{1}H–^{13}C HMQC, ^{1}H–^{1}H NOESY and ^{1}H–^{15}N HMQC sequences.[13] Because of the double heteronuclear filter, a 4 step phase cycle is sufficient to produce spectra free of artifacts. The transfer of magnetization from the aliphatic protons to the NH protons follows the pathway

$$^{1}H \xrightarrow{^{1}J_{CH}} {}^{13}C \xrightarrow{^{1}J_{CH}} {}^{1}H \xrightarrow{NOE} NH \xrightarrow{^{1}J_{NH}} {}^{15}N \xrightarrow{^{1}J_{NH}} NH.$$

The chemical shifts of ^{13}C, ^{1}H and ^{15}N evolve during the variable time periods t_1, t_2 and t_3 which are incremented independently, and the NH signal is detected during the acquisition period t_4. There are three key aspects of practical importance concerning this 4D experiment. First, the number of peaks in this 4D spectrum is the same as that present in the corresponding $^{15}N/^{13}C$ edited 3D and 2D spectra, so that the extension to a fourth dimension increases the resolution without a concomitant increase in complexity. Second, the through-bond transfer steps are highly efficient as they involve one-bond heteronuclear couplings (90–130 Hz) which are much larger than the linewidths. As a result, the sensitivity of the experiment is high and it can easily be performed on a 1–2 mM sample of uniformly labeled $^{15}N/^{13}C$ protein. Third, extensive folding can be employed to maximize resolution in the

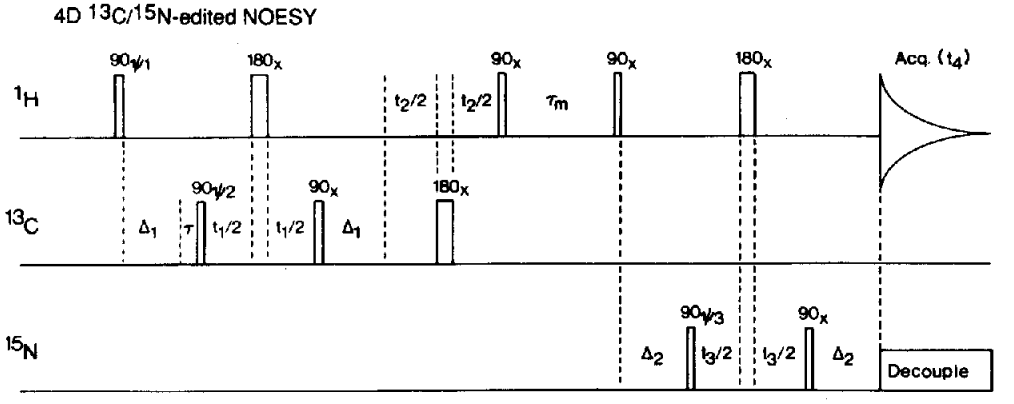

FIG. 35. Pulse sequence of the $^{13}C/^{15}N$-edited NOESY 4D experiment.[13] Phase cycling is as follows: $\psi 1 = 4x$, $\psi 2 = 2(x, -x)$, $\psi 3 = 2(x)$, $2(-x)$, Receiver = x, $2(-x)$, x. To minimize relaxation losses, the delays Δ_1 and Δ_2, that allow for efficient creation of heteronuclear multiple quantum coherence, should be set to 3.0 ms and 4.5 ms, slightly less than $1/(2J_{HC})$ and $1/(2J_{HN})$, respectively. The delay, τ, immediately prior to application of the first ^{13}C 90° pulse is included to compensate for the ^{13}C 180° pulse so that no first order phase correction is necessary in F_2. ^{15}N decoupling during acquisition can be achieved using incoherent GARP or WALTZ decoupling.

$^{13}C(F_1)$ dimension so that each ^{13}C coordinate corresponds to a series of ^{13}C chemical shifts separated by intervals of typically ~20 ppm. This does not complicate the interpretation of the 4D spectrum in any way since all ^{13}C resonances would have been previously assigned using the 3D HNCA, HCCH–COSY and HCCH–TOCSY experiments described in Sections 3.1.3 and 3.1.4, and the appropriate ^{13}C chemical shift is easily ascertained on the basis of the ^{1}H chemical shift of the aliphatic proton from which the magnetization originates.

Selected $F_4(NH)$–$F_2(^1H)$ slices of the 4D $^{13}C/^{15}N$-edited NOESY experiment on $^{13}C/^{15}N$ labeled IL-1β at two $^{15}N(F_3)$ and several $^{13}C(F_1)$ frequencies are shown in Fig. 36, together with the

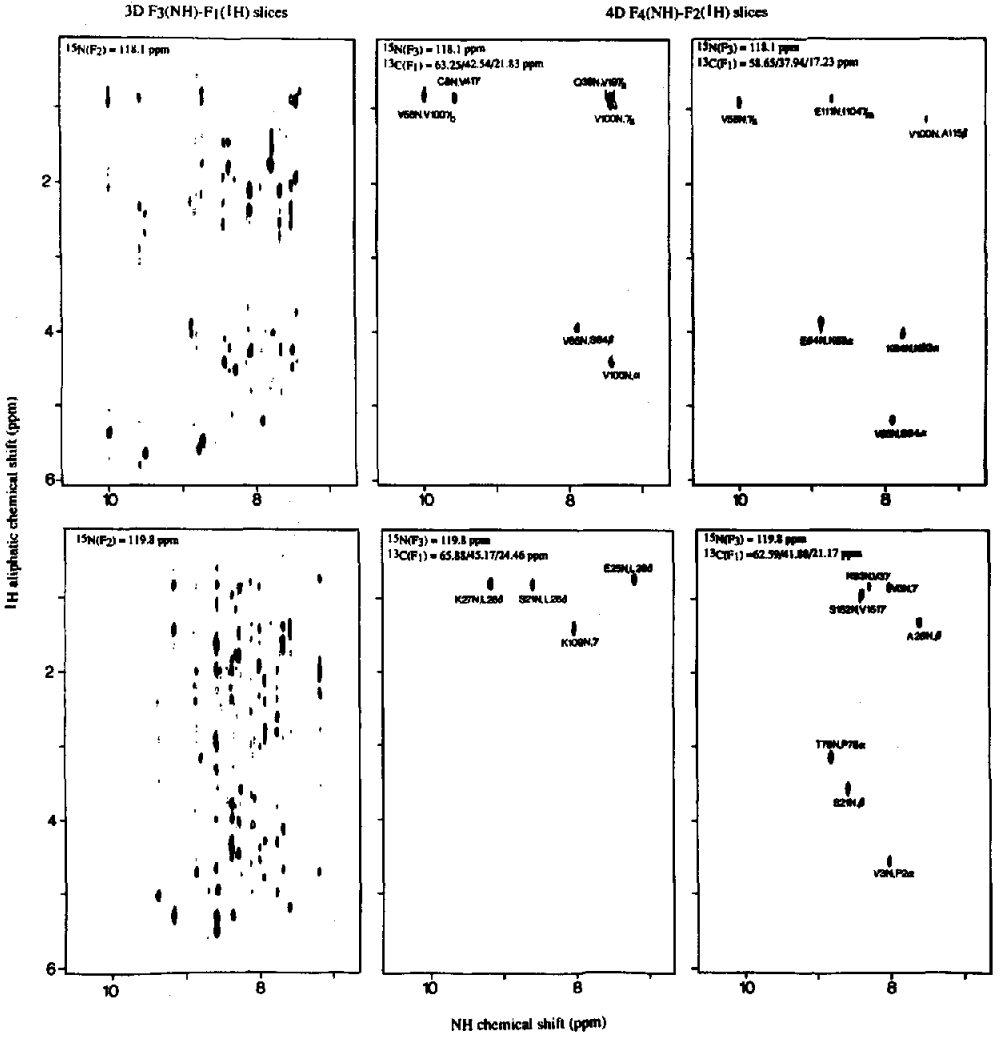

FIG. 36. Representative $F_4(NH)$–$F_2(^1H)$ planes of the 4D $^{15}N/^{13}C$ edited NOESY spectrum together with the $F_3(NH)$–$F_1(^1H)$ slices of the 3D $^{15}N/^{13}C$ edited NOESY spectrum at the corresponding ^{15}N frequencies.[13] The acquired 4D data matrix comprised 16 complex (t_1) × 64 complex (t_2) × 16 complex (t_3) × 512 real (t_4) data points. To ensure that the phase of the folded peaks in F_1 is the same as those that are not folded, the delays and pulse widths in the sequence were chosen such that the zero and first order phase corrections in $F_1(^{13}C)$ were $-90°$ and 180°, respectively. The spectral widths employed in F_1, F_2, F_3 and F_4 are 20.71, 8.3, 26.0 and 6.94 ppm, respectively, with corresponding acquisition times of 5.0, 12.6, 9.8 and 61.4 ms in t_1, t_2, t_3 and t_4, respectively. The absorptive part of the final processed data matrix comprised 64 × 128 × 32 × 512 points with a digital resolution of 48.8, 38.9, 49.4 and 8.1 Hz/pt in F_1, F_2, F_3 and F_4 respectively.

corresponding F_3(NH)–F_1(^{1}H) slices of the 3D ^{13}C/^{15}N-edited ^{1}H–^{15}N NOESY–HMQC spectrum at the same ^{15}N(F_2) chemical shifts.[113] The improved resolution relative to the 3D spectrum is clearly apparent. For example, consider the NOEs between an aliphatic ^{1}H resonance at 0.89 ppm and the NH protons of Ser-21, Lys-27, Gln-39 and Val-58. Between 1.2 and 0.8 ppm alone there are some 57 separate ^{1}H resonances, so that the assignments of these NOEs from the 3D spectrum is virtually impossible. The two NOEs involving Ser-21(NH) and Lys-27(NH) are seen in the slice at δ^{13}C = 65.9/45.2/21.9 ppm. while those involving Gln-39(NH) and Val-58(NH) are observed in the slice at δ^{13}C = 63.3/42.5/21.9 ppm. From the ^{1}H and ^{13}C assignments in hand, it is a simple matter to assign the NOEs to Ser-21(NH) and Lys-27(NH) as originating from one of the methyl group of Leu-26. The NOEs to Gln-39(NH) and Val-58(NH) could involve the same or a different methyl group of either Val-19 or Val-100. The NOE, however, to Val-58(NH) is maximal in this slice, while that to Gln-39(NH) is maximal in the adjacent slice downfield in ^{13}C chemical shift, indicating that they arise from methyl groups with different ^{13}C chemical shifts. This enables one to deduce that the NOE to Val-58(NH) originates from Val-100($C^{\gamma b}H_3$), while that to Gln-39(NH) arises from Val-19($C^{\gamma a}H_3$).

5.3. *The 4D ^{13}C/^{13}C-Edited NOESY Experiment*

The pulse scheme for the 4D ^{13}C/^{13}C-edited NOSEY experiment is shown in Fig. 37. Although it is based on the same philosophy that led to the 4D ^{13}C/^{15}N-edited sequence, the exact form of this sequence is the result of a long and iterative development procedure.[69] As in the 4D ^{13}C/^{15}N-edited NOESY spectrum it comprises a central NOESY sequence sandwiched between two HMQC sequences so that the transfer of magnetization follows the pathway

$$^1H \xrightarrow{^1J_{CH}} {}^{13}C \xrightarrow{^1J_{CH}} {}^1H \xrightarrow{NOE} {}^1H \xrightarrow{^1J_{CH}} {}^{13}C \xrightarrow{^1J_{CH}} {}^1H.$$

^{1}H magnetization of the originating and destination protons evolves during t_2 and t_4, while the corresponding ^{13}C chemical shifts of the attached carbon atoms evolve during t_1 and t_3. Unlike the 4D ^{13}C/^{15}N-edited NOESY experiment, however, it is much more difficult to design a suitable pulse scheme for the 4D ^{13}C/^{13}C-edited NOESY experiment which yields an artifact free spectrum, given that the length of the phase cycling is severely limited if the experiment is to be recorded in a practical time frame. This is due to two factors. First, there are a larger number of minor magnetization transfer pathways in the homonuclear ^{13}C/^{13}C case than in the heteronuclear ^{15}N/^{13}C case that can lead to spurious magnetization. Second, in the 4D ^{15}N/^{13}C-edited spectrum there are no 'diagonal peaks' that would correspond to magnetization that has not been transferred from one hydrogen to another, as double heteronuclear filtering is extremely efficient at completely removing these normally very intense resonances. In the ^{13}C/^{13}C-edited experiment, on the other hand, a double heteronuclear filter is not

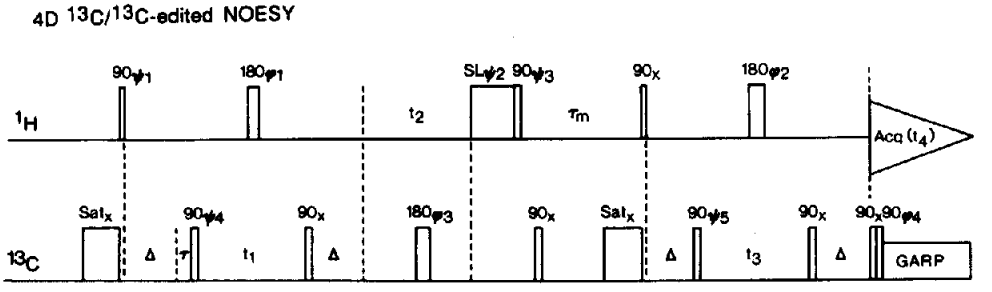

FIG. 37. Pulse scheme for the 4D ^{13}C/^{13}C-edited NOESY experiment.[69] The eight step phase cycle is as follows: $\psi1 = x$; $\psi2 = -y$; $\psi3 = x$; $\psi4 = x, -x$; $\psi5 = 2(x), 2(-x)$; $\phi1 = 4(x), 4(y)$; $\phi2 = 4(x), 4(y)$; $\phi3 = 2(x), 2(-x)$; $\phi4 = x, -x$; Receiver = x, 2(−x), x. The ^{13}C 180° pulse is a composite pulse ($90_x - 180_y - 90_x$); Sat_x is a 1 ms ^{13}C saturation pulse; and $SL_{\psi2}$ is a 500 μs ^{1}H spin lock pulse. The delay $\Delta = 1/(2J_{CH})$ (~3.4 ms).

available making it very difficult to design a pulse sequence that minimizes the level of artifacts associated with these intense resonances.

The rationale behind the pulse sequence in Fig. 37 is as follows.[69] To prevent magnetization originating on ^{13}C spins being transferred to coupled ^{1}H spins via a DEPT[76] type mechanism, a 1 ms ^{13}C saturation pulse is applied immediately prior to the first ^{1}H 90° pulse. In the same vein, the ^{13}C 90_x pulse applied at the beginning of the NOESY mixing period converts all residual I_zS_z magnetization to I_zS_x, and any residual ^{13}C magnetization is removed by the 1 ms ^{13}C saturation pulse at the end of the NOESY mixing period. The spin lock pulse along the $-y$ axis applied prior to the second ^{1}H 90° pulse ensures that all ^{1}H magnetization other than that lying along $-y$ is dephased. In principle, phase cycling of the ^{1}H 180° pulse in the middle of the evolution periods t_1 and t_3 along the $\pm x$ axes would eliminate artifacts originating from the partial 90° character of the 180° ^{1}H pulse. However, to ensure that the experiment can be recorded within a reasonable time frame with appropriate digital resolution, the phase cycling has to be restricted to a maximum of eight steps. In particular, the ^{13}C 90° pulses at the beginning of the two HMQC sequences are phase cycled independently in conjunction with the receiver phase along the $\pm x$ axes to eliminate axial peaks in F_1 and F_3. The ^{13}C 180° pulse in the middle of the evolution period t_2 is phase cycled along the $\pm x$ axes concurrently with the 90° pulse at the beginning of the second HMQC sequence in order to prevent magnetization residing on ^{1}H spins at the beginning of the t_2 period from being transferred to coupled ^{13}C spins. Finally, the ^{1}H 180° pulses in the middle of the t_1 and t_3 periods are cycled concurrently along the x and y axes to eliminate the effects arising from the partial 0° character of the 180° pulse (due to the fact that at best only 80% of the resonance intensity is inverted) which gives rise to false diagonal peaks which would appear at $\pm\omega_H$ in the ^{13}C dimensions. It should be noted that phase cycling of these two ^{1}H 180° pulses simultaneously can be carried out without any untoward effects as the artifacts occurring during the t_1 period are independent of those in the t_3 period (cf. Section 2.4.4). Finally, to eliminate quadrature artifacts in the $F_2(^1H)$ dimension, the States part of the method of obtaining quadrature in the F_2 dimension is applied to the phases of the second ^{1}H 90° pulse ($\psi 3$) and associated ^{1}H spin lock pulse ($\psi 2$), while the TPPI part is applied to the first ^{1}H 90° pulse ($\psi 1$).

A number of other features of the pulse sequence in Fig. 37 are worth pointing out.[69] The delay τ, immediately prior to the application of the first ^{13}C 90° pulse, is set to the duration of the ^{13}C 180° composite pulse. This serves to compensate for the ^{13}C 180° pulse in the middle of t_2 so that no first order phase correction is necessary in F_2. The length of the initial t_1 and t_3 delays should be adjusted to exactly half a dwell time such that the zero and first order phase corrections in F_1 and F_3 are 90° and $-180°$, respectively. This is achieved by setting $[t_{1,3}(0)+\tau_{180}(^1H)+4\tau_{90}(^{13}C)/\pi]=\Delta t_{1,3}/2$, where $\Delta t_{1,3}$ is the value of the t_1 and t_3 increment, and $t_{1,3}(0)$ is the initial value of the t_1 and t_3 delays (cf. Section 2.4.2). This ensures that the folded peaks are all absorptive and have positive or negative amplitudes depending on whether the number of times they are folded is even or odd, respectively. It also permits for the purposes of linear prediction, the data to be extended to negative time as discussed in Section 5.1.

The relationship between 3D ^{13}C-edited NOESY and 4D $^{13}C/^{13}C$-edited NOESY spectra is shown in Fig. 38.[69] The 3D spectrum comprises a single cube in which NOEs appear in different ^{1}H–^{1}H planes determined by the ^{13}C chemical shift of the carbon atom attached to the destination proton. Each ^{1}H–^{1}H slice of the 3D cube constitutes a cube in the 4D spectrum in which the NOEs are further edited by the ^{13}C chemical shift of the carbon atom bonded to the originating proton. Thus, the 4D spectrum consists of a series of 3D cubes at different ^{13}C chemical shifts in the F_3 dimension, corresponding to the resonance frequency of the carbon atom directly bonded to the destination proton(s), and the axes of each cube are the ^{1}H chemical shifts of the originating and destination protons in F_2 and F_4, respectively, and the ^{13}C chemical shift of the carbon atom attached to the originating proton in the F_1 dimension.

In principle, a 3D ^{13}C-edited NOESY spectrum[62, 63] contains approximately the same information as the 4D $^{13}C/^{13}C$-edited spectrum. However, in any given ^{13}C slice of the 3D spectrum, the NOE peak between the originating proton H_k and the destination proton H_i is only labeled by the two ^{1}H chemical shifts and the chemical shift of the carbon atom directly bonded to the destination proton C_i. In the majority of cases there are many protons which resonate at the same chemical shift as H_k.

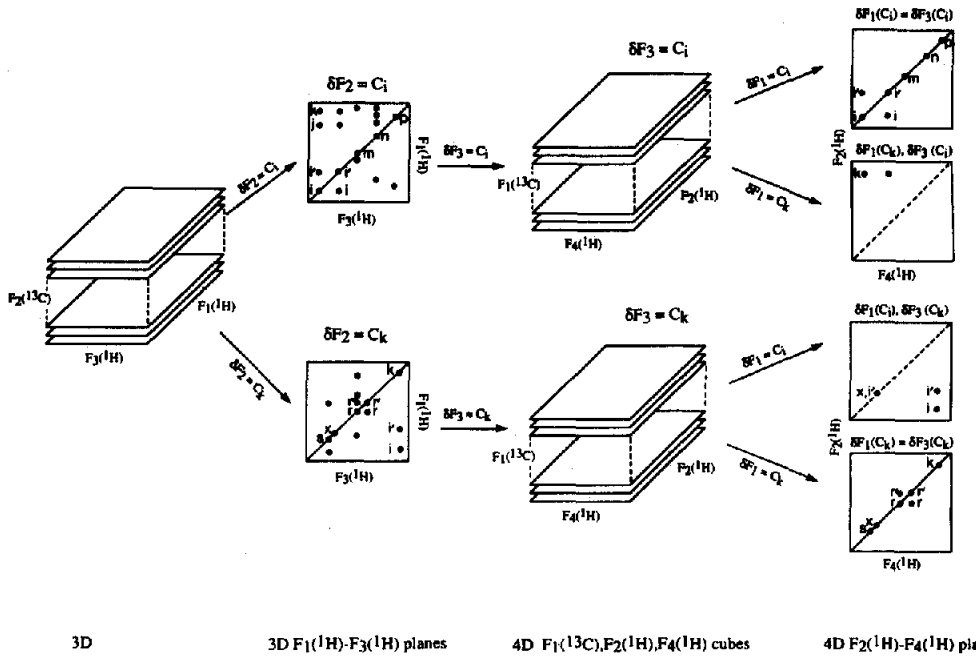

FIG. 38. Schematic representation of the relationship between 3D ^{13}C-edited NOESY and 4D ^{13}C/^{13}C-edited NOESY spectra.[69]

Consequently, in the 3D spectrum it is essential to be able to locate the symmetry related NOE cross peak at the chemical shift of the carbon atom C_k directly bonded to H_k in order to assign the identity of H_k with any degree of confidence.[41, 69] This task can be rendered difficult due to the presence of t_1 noise and extensive spectral overlap in the $^1H(F_1)$ dimension, as well as by the fact that many of the NOE peaks are of very weak intensity, and may not appear in both locations in the 3D spectrum. In the case of the 4D spectrum, all this information is contained in a single peak. Further, each NOE appears twice in the 4D spectrum (as the ^{13}C shifts of the destination and originating carbon atoms are swapped), providing a means to improve the quality of the spectrum by symmetrization. An additional and major advantage of the 4D over the 3D spectrum is that in the 4D spectrum genuine 'diagonal' peaks corresponding to magnetization that has not been transferred from one proton to another, as well as the intense NOE peaks involving protons attached to the same carbon atom (i.e. methylene protons), appear in only a single $F_2(^1H)$, $F_4(^1H)$ plane of each $F_1(^{13}C)$, $F_2(^1H)$, $F_4(^1H)$ cube at the carbon frequency where the originating and destination carbon atoms coincide (i.e. at $F_1 = F_3$). Therefore, these intense resonances no longer obscure NOEs between protons with similar or even degenerate chemical shifts, thus providing additional valuable interproton distance restraints for the 3D structure determination.

In the schematic example illustrated in Fig. 38,[69] there are three protons close in space: the methylene protons i and i' attached to the same carbon atom C_i, and a methyl proton k attached to the carbon atom C_k. In the 3D spectrum, the diagonal peaks for the methylene protons i and i', and NOE cross peaks between the methylene protons i and i' and from the methyl proton k to the methylene protons i and i' are seen at the $^{13}C(F_2)$ frequency of C_i; the diagonal peak for k and the NOEs from i and i' to k are seen at the $^{13}C(F_2)$ frequency of C_k. In the 4D spectrum, the diagonal peaks for the methylene protons i and i', and the methyl proton k are seen in the $^1H(F_2)-{}^1H(F_4)$ planes at $\delta F_1(^{13}C_i) = \delta F_3(^{13}C_i)$ and $\delta F_1(^{13}C_k) = \delta F_3(^{13}C_k)$, respectively. The NOEs from k to i are seen in the $^1H(F_2)$–$^1H(F_4)$ plane at $\delta F_1(C_k)$, $\delta F_3(C_i)$, while the NOEs from i and i' to k are seen in the

$^1H(F_2)$–$^1H(F_4)$ planes at $\delta F_1(C_i)$, $\delta F_3(C_k)$. Also shown in the latter plane is an NOE between two protons x and i' with identical chemical shifts, where the chemical shift of the carbon atom attached to x is the same as that of C_k.

Examples of several different planes of the 4D $^{13}C/^{13}C$-edited NOESY spectrum of $^{13}C/^{15}N$ labeled IL-1β are shown in Figs 39 and 40, clearly demonstrating their extreme simplicity and sparseness.[69]

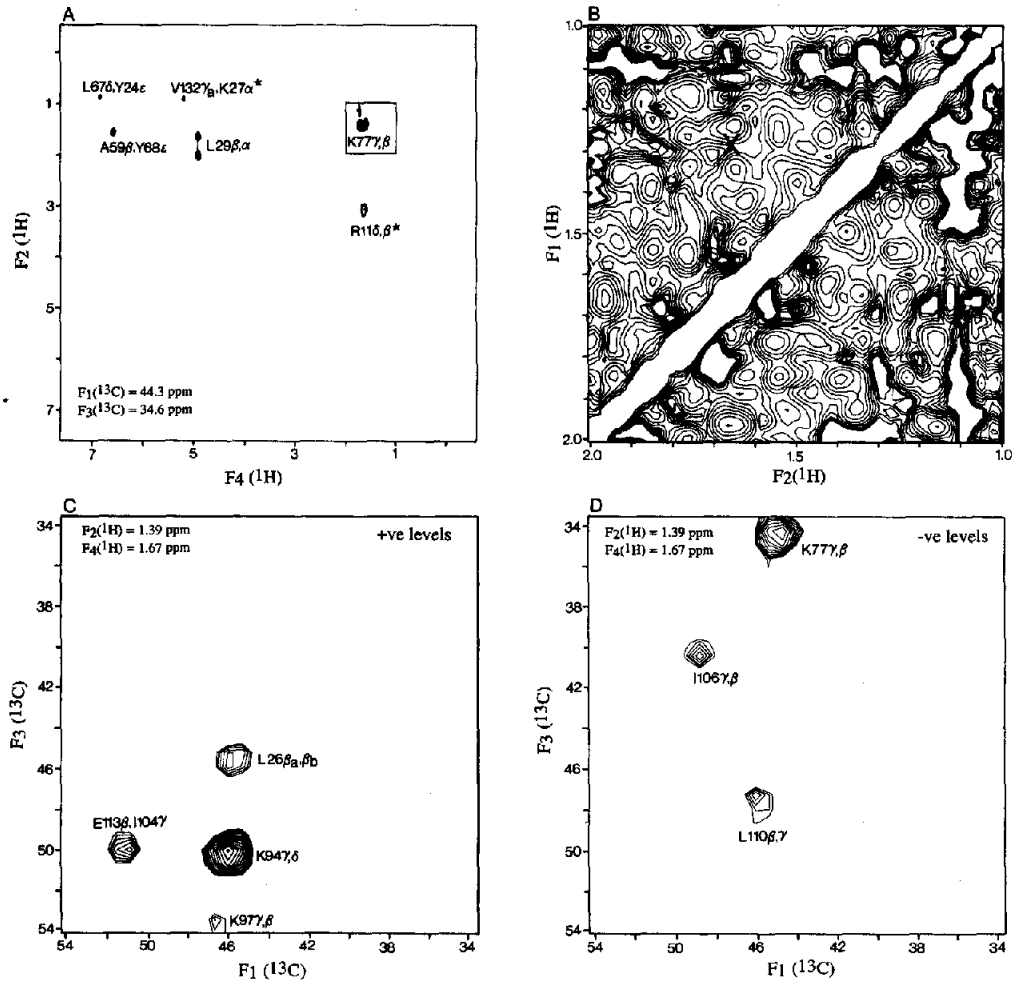

FIG. 39. Selected $F_2(^1H)$–$F_4(^1H)$ and $F_1(^{13}C)$–$F_3(^{13}C)$ planes of the 600 MHz 4D $^{13}C/^{13}C$-edited NOESY spectrum of 1.7 mM $^{13}C/^{15}N$ labeled IL-1β in D_2O.[69] (A) $F_2(^1H)$–$F_4(^1H)$ slice at $\delta F_1(^{13}C) = 44.3$ ppm and $\delta F_3(^{13}C) = 34.6$ ppm; (C) and (D) positive and negative contours of the $F_1(^1H)$–$F_3(^{13}C)$ plane at $\delta F_2(^1H) = 1.39$ ppm, $\delta F_4(^1H) = 1.67$ ppm corresponding to the ^1H chemical shifts of the cross peak between the $C^\gamma H$ and $C^{\beta a}H$ protons of Lys-77 shown by the arrow in (A); (B) Region between 1 and 2 ppm of the 110 ms 2D NOESY spectrum of IL-1β (with a digital resolution of 6.9 Hz), corresponding to the boxed region shown in (A). (The X marks the ^1H coordinates of the peak indicated by the arrow in A.) Note that because extensive folding is employed, the ^{13}C chemical shifts are given by $x \pm nSW$, where x is the ppm value listed in the figure, n is an integer and SW is the spectral width (20.71 ppm). In (A) there are two positive cross peaks indicated by an asterisk, while the remaining cross peaks are negative. The acquired 3D data matrix comprised 8 complex (t_1) × 64 complex (t_2) × 8 complex (t_3) × 256 real (t_4) data points, and the total measuring time was 78 h. The spectral widths in F_1, F_2, F_3 and F_4 were 3125, 5263, 3125 and 5346 Hz, respectively, with corresponding acquisition times of 2.56, 12.16, 2.56 and 23.94 ms, respectively. The absorptive part of the final processed data matrix comprised 32 × 128 × 32 × 256 points with a digital resolution of 97.7, 41.1, 97.7 and 21 Hz in F_1, F_2, F_3 and F_4, respectively.

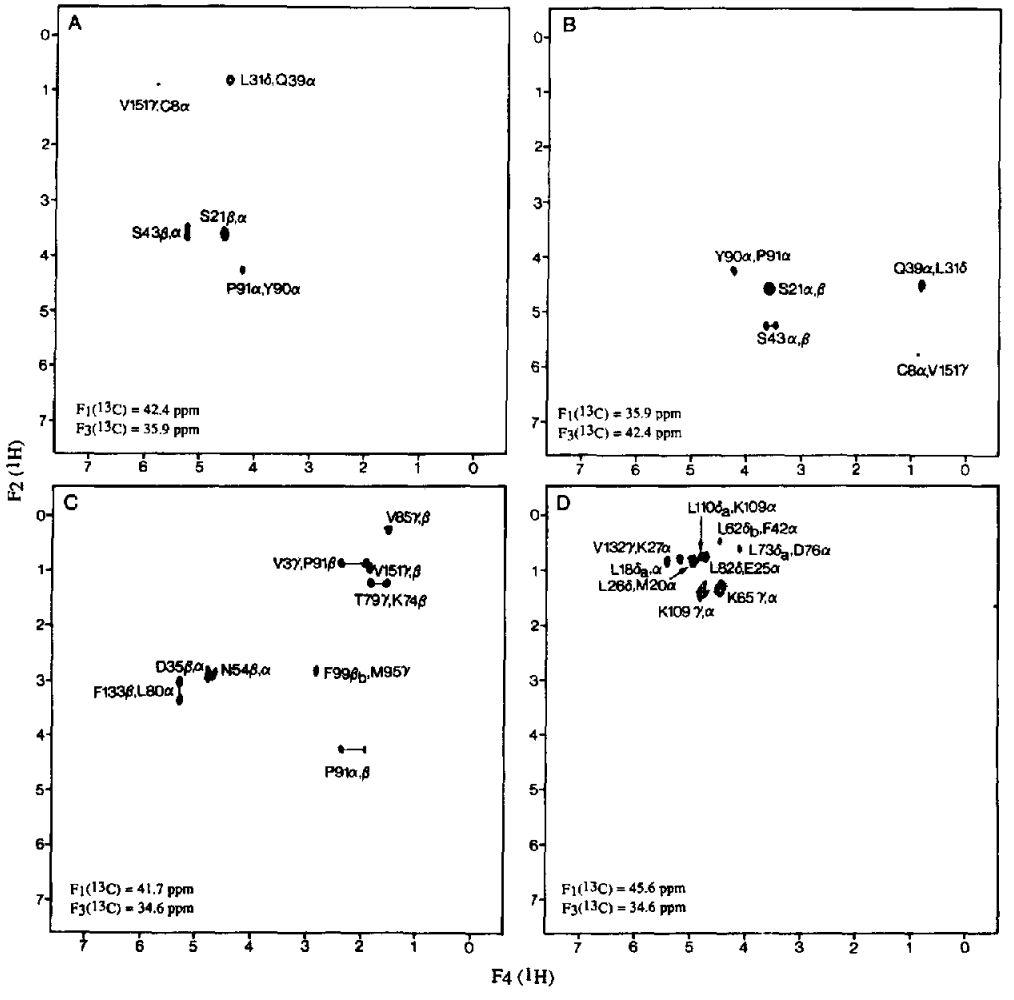

FIG. 40. Selected $F_2(^1H)$–$F_4(^1H)$ slices at several $F_3(^{13}C)$ and $F_1(^{13}C)$ chemical shifts of the 4D $^{13}C/^{13}C$-edited NOESY spectrum of IL-1β.[69] (A) and (B) constitute 'mirror image' planes displaying NOE interactions between the same set of protons. (C) and (D) show two ^1H–^1H planes taken at the same $F_3(^{13}C)$ frequency, but different $F_1(^{13}C)$ frequencies. A single slice of a regular 3D ^{13}C-edited NOESY spectrum in the present case would consist of 32 such planes superimposed on one another. Only positive contours are displayed in (A), (B) and (C), while only negative ones are plotted in (D).

As in the 4D $^{13}C/^{15}N$-edited case interpretation of the complete 4D $^{13}C/^{13}C$-edited NOESY spectrum is straightforward using a simple search algorithm to match up the four chemical shift coordinates of each peak with the complete list of ^1H and ^{13}C assignments already available from 3D methods.

Figure 39 shows the $F_2(^1H)$–$F_4(^1H)$ plane at $\delta F_1(^{13}C)$, $\delta F_3(^{13}C) = 44.3$, 34.6 ppm. As extensive folding is employed, each ^{13}C frequency corresponds to several ^{13}C chemical shifts given by $x \pm nSW$, where x is the shift specified, n an integer, and SW the spectral width (in this case 20.71 ppm). A number of long range NOE cross peaks are clearly discerned involving both aromatic and aliphatic protons. In addition, there are a number of intraresidue cross peaks. The intraresidue NOE between the $C^{\beta}H$ and $C^{\gamma}H$ protons of Lys-77 occurs in the region between 1 and 2 ppm. A plot of this region of the 2D spectrum is shown in Fig. 39B and the position of the peak between the $C^{\gamma}H$ and $C^{\beta a}H$ protons of Lys-77 which is indicated by the arrow in Fig. 39A, is marked by the letter X in Fig. 39B. It is clear from Fig.

39B that no individual cross peaks can be resolved in this region of the 2D spectrum. Figures 39C and D show the positive and negative contours, respectively, of the $F_1(^{13}C)$–$F_3(^{13}C)$ plane at $F_2(^1H)$, $F_4(^1H) = 1.39$, 1.67 ppm corresponding to the ^1H coordinates of the cross peak between the $C^{\gamma}H$ and $C^{\beta_a}H$ protons of Lys-77. There are 4 positive cross peaks (in which the number of times the peaks are folded is even), and 3 negative ones (in which the number of times the peaks are folded is odd) clearly resolved in this single $F_1(^{13}C)$–$F_3(^{13}C)$ plane of the spectrum. Thus, seven NOE cross peaks are superimposed at the ^1H coordinates of 1.39, 1.67 ppm, which could not have been assigned in either a 2D or a 3D ^{13}C-edited NOESY spectrum.

Figures 40A and B show two $F_2(^1H)$–$F_4(^1H)$ planes at $\delta F_1(^{13}C)$, $\delta F_3(^{13}C) = 42.4$, 35.9 ppm and 35.9, 42.4 ppm, respectively. Thus, these two planes are related by symmetry, and the same NOEs are observed with comparable intensities in both planes with the $F_2(^1H)$ and $F_4(^1H)$ frequencies of the cross peaks interchanged. A number of intraresidue and long range interresidue NOEs are observed.

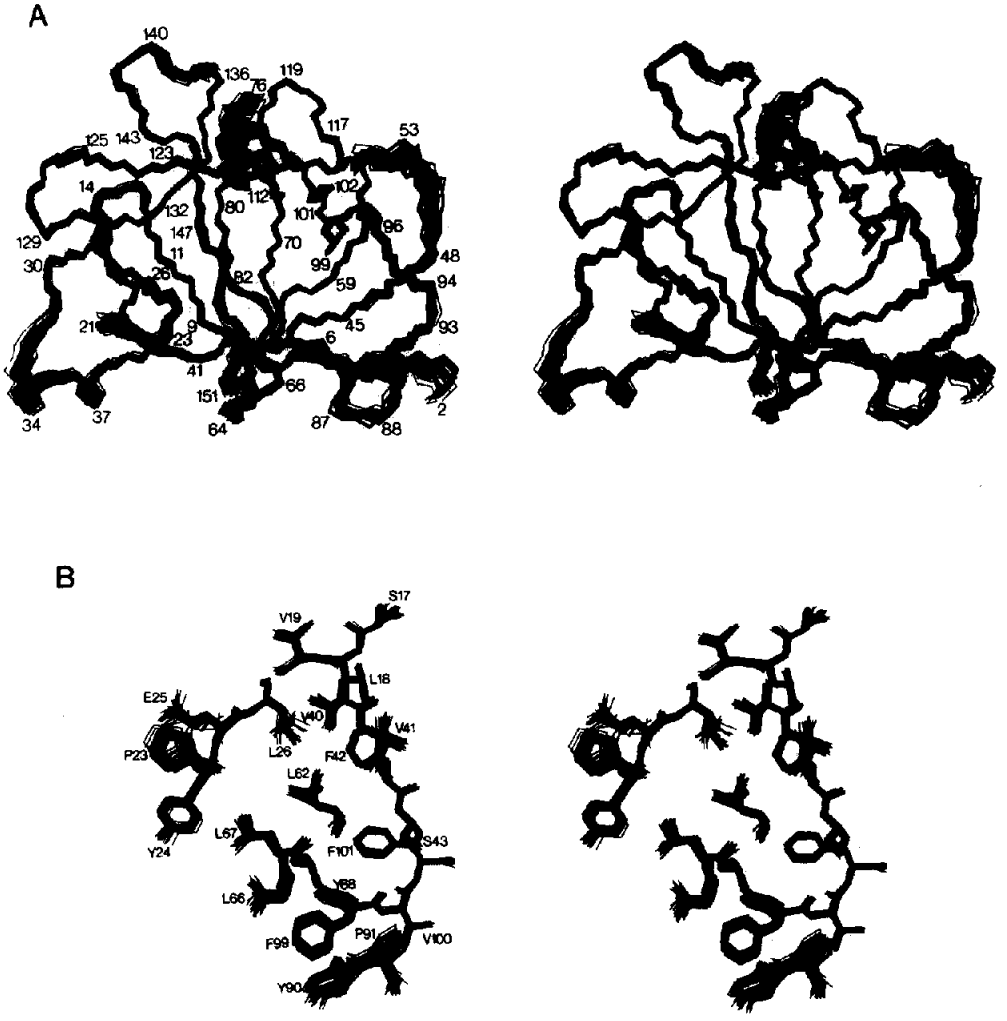

FIG. 41. Stereoviews of the 3D structure of IL-1β determined by 3D and 4D heteronuclear NMR spectroscopy.[77] Best fit superposition of the backbone (N, C^{α}, C) atoms and selected side chains of the 32 simulated annealing structures are shown in (A) and (B), respectively. The structures have been calculated on the basis of a total of 3146 experimental NMR restraints.

In addition, there is a sequential NOE between the $C^{\alpha}H$ protons of Tyr-90 and Pro-91 (indicative of a *cis*-proline). The resonances of these protons have near identical chemical shifts (4.19 and 4.25 ppm, respectively) so that this particular NOE would have been very difficult to observe in either a 2D spectrum or a 3D ^{13}C-edited NOESY spectrum, as the cross peak is located so close to the diagonal. Another example of an NOE between protons with near identical chemical shifts can be seen in Fig. 40C between Phe-99($C^{\beta b}H$) and Met-95($C^{\gamma}H$) at $\delta F_2(^1H)$, $\delta F_4(^1H) = 2.87$, 2.75 ppm.

6. CONCLUDING REMARKS

In this review we have presented a number of 3D and 4D heteronuclear experiments which have been designed to extend the range of applicability of the NMR method of structure determination to proteins in the 15–30 kDa range. While it is clear that these methods offer a means of overcoming problems associated both with extensive resonance overlap and large linewidths, the true test of any new approach must lie in the demonstration of its use in a practical situation. The experiments presented have been applied to two proteins: IL-1β (153 residues) and calmodulin (148 residues). At the present time complete ^1H, ^{13}C and ^{15}N backbone and side chain resonance assignments have been obtained for IL-1β,[12,41] and complete backbone assignments have been obtained for calmodulin.[39] Resonance assignments, however, are only a means to an end, namely the determination of a 3D structure. This goal has indeed been attained in the case of IL-1β.[77] A stereoview showing a superposition of 32 calculated structures of IL-1β is shown in Fig. 41 and is based on 3146 experimental restraints comprising 2780 distance and 360 torsion angle restraints. The atomic rms distribution of the individual structures about the mean coordinate positions is 0.41 Å for the backbone atoms, 0.8 Å for all atoms, and 0.5 Å for all atoms of internal residues with a surface accessibility $\leqslant 40\%$. This result, which could only have been achieved through the application of both 3D and 4D heteronuclear NMR techniques, clearly demonstrates that the methodology is now at hand for determining the 3D structures of proteins up to ~ 300 residues at a degree of accuracy and precision that is comparable to the very best results attainable for small proteins. Thus, these new 3D and 4D methods usher in a whole new era of NMR protein structure determination opening the way to studies of a large number of medium sized proteins (15–40 kDa) of biological interest.

Acknowledgements—We thank all our collaborators, past and present, who have contributed to the work carried out in our laboratory. Above all others, we would like to acknowledge Dr Ad Bax with whom we have shared numerous stimulating discussions, fruitful experiments, and a continuous and most enjoyable collaboration in the best of scientific spirits. The work in the authors' laboratory was supported in part by a grant from the AIDS Directed Anti-Viral Program of the Office of the Director of the National Institutes of Health.

REFERENCES

1. G. M. CLORE and A. M. GRONENBORN, *CRC Crit. Rev. Biochem. Mol. Biol.* **24**, 479 (1989).
2. K. WÜTHRICH, *Science* **243**, 45 (1989).
3. K. WÜTHRICH, *Acc. Chem. Res.* **22**, 36 (1989).
4. A. M. GRONENBORN and G. M. CLORE, *Analyt. Chem.* **62**, 2 (1990).
5. A. BAX, *Ann. Rev. Biochem.* **58**, 223 (1989).
6. G. M. CLORE and A. M. GRONENBORN, *Ann. Rev. Biophys. Chem.* **20**, 29 (1991).
7. P. J. KRAULIS, G. M. CLORE, M. NILGES, T. A. JONES, G. PETTERSSON, J. KNOWLES and A. M. GRONENBORN, *Biochemistry* **28**, 7241 (1989).
8. Y. Q. QIAN, M. BILLETER, G. OTTING, M. MÜLLER, W. J. GEHRING, W. J. and K. WÜTHRICH, *Cell* **59**, 573 (1989).
9. G. M. CLORE, E. APPELLA, E. YAMADA, K. MATSUSHIMA, and A. M. GRONENBORN, *Biochemistry* **29**, 1689 (1990).
10. J. OMICHINSKI, G. M. CLORE, E. APPELLA, K. SAKAGUCHI, and A. M. GRONENBORN, *Biochemistry* **29**, 9324 (1990).
11. J. D. FORMAN-KAY, G. M. CLORE, P. T. WINGFIELD and A. M. GRONENBORN, *Biochemistry* **30**, 2685 (1991).
12. P. C. DRISCOLL, G. M. CLORE, D. MARION, P. T. WINGFIELD and A. M. GRONENBORN, *Biochemistry* **29**, 3542 (1990).
13. L. E. KAY, G. M. CLORE, A. BAX and A. M. GRONENBORN, *Science* **249**, 411 (1990).

14. R. R. ERNST, G. BODENHAUSEN and G. WOKAUN, *Principles of Nuclear Magnetic Resonance in One and Two Dimensions*, Clarendon Press, Oxford (1987).
15. C. GRIESINGER, O. W. SØRENSEN and R. R. ERNST, *J. Am. Chem. Soc.* **109**, 7227 (1987).
16. H. OSCHKINAT, C. GRIESINGER, P. J. KRAULIS, O. W. SØRENSEN, R. R. ERNST, A. M. GRONENBORN and G. M. CLORE, *Nature* **332**, 374 (1988).
17. H. OSCHKINAT, C. CIESLAR, A. M. GRONENBORN and G. M. CLORE, *J. Magn. Reson.* **81**, 212 (1989).
18. H. OSCHKINAT, C. CIESLAR, T. A. HOLAK, G. M. CLORE and A. M. GRONENBORN, *J. Magn. Reson.* **83**, 450 (1989).
19. G. W. VUISTER, R. BOELENS and R. KAPTEIN, *J. Magn. Reson.* **80**, 176 (1988).
20. G. W. VUISTER, R. BOELENS, A. PADILLA, G. J. KLEYWEGT and R. KAPTEIN, *Biochemistry* **29**, 1829 (1990).
21. A. BAX, S. W. SPARKS and D. A. TORCHIA, *Methods Enzymol.* **176**, 134 (1989).
22. G. A. MORRIS and R. FREEMAN, *J. Am. Chem. Soc.* **101**, 760 (1979).
23. L. MUELLER, *J. Am. Chem. Soc.* **101**, 4481 (1979).
24. A. BAX, R. G. GRIFFEY and B. L. HAWKINS, *J. Magn. Reson.* **55**, 301 (1983).
25. A. G. REDFIELD, *Chem. Phys. Lett.* **96**, 537 (1987).
26. A. BAX, *J. Magn. Reson.* **53**, 149 (1983).
27. L. E. KAY, M. IKURA and A. BAX, *J. Magn. Reson.*, in press (1991).
28. D. MARION and K. WÜTHRICH, *Biochem. Biophys. Res. Commun.* **113**, 967 (1983).
29. D. MARION, M. IKURA, R. TSCHUDIN and A. BAX, *J. Magn. Reson.* **85**, 393 (1989).
30. D. J. STATES, R. A. HABERKORN and D. J. RUBEN, *J. Magn. Reson.* **48**, 286 (1982).
31. D. MARION and A. BAX, *J. Magn. Reson.* **79**, 352 (1988).
32. A. BAX, M. IKURA, L. E. KAY and G. ZHU, *J. Magn. Reson.*, in press (1991).
33. L. E. KAY, D. MARION and A. BAX, *J. Magn. Reson.* **84**, 72 (1989).
34. A. BAX, G. M. CLORE, P. C. DRISCOLL, A. M. GRONENBORN, M. IKURA and L. E. KAY, *J. Magn. Reson.* **87**, 620 (1990).
35. K. WÜTHRICH, *NMR of Proteins and Nucleic Acids*, John Wiley, New York (1986).
36. A. M. GRONENBORN, A. BAX, P. T. WINGFIELD and G. M. CLORE, *FEBS Lett.* **243**, 93 (1989).
37. A. M. GRONENBORN, P. T. WINGFIELD and G. M. CLORE, *Biochemistry* **28**, 5081 (1989).
38. D. MARION, P. C. DRISCOLL, L. E. KAY, P. T. WINGFIELD, A. BAX, A. M. GRONENBORN and G. M. CLORE, *Biochemistry* **29**, 6150 (1989).
39. M. IKURA, L. E. KAY and A. BAX, *Biochemistry* **29**, 4659 (1990).
40. L. E. KAY, M. IKURA, R. TSCHUDIN and A. BAX, *J. Magn. Reson.* **89**, 496 (1990).
41. G. M. CLORE, A. BAX, P. C. DRISCOLL, P. T. WINGFIELD and A. M. GRONENBORN, *Biochemistry* **29**, 8172 (1990).
42. L. E. KAY, M. IKURA and A. BAX, *J. Am. Chem. Soc.* **112**, 888 (1990).
43. A. BAX, G. M. CLORE and A. M. GRONENBORN, *J. Magn. Reson.* **88**, 425 (1990).
44. S. W. FESIK, H. L. EATON, E. T. OLEJNICZAK, E. R. P. ZUIDERWEG, L. P. MCINTOSH and F. W. DAHLQUIST, *J. Am. Chem. Soc.* **112**, 886 (1990).
45. G. M. CLORE, A. BAX and A. M. GRONENBORN, *J. Biomol. NMR*, in press (1991).
46. A. J. SHAKA, C. J. LEE and A. PINES, *J. Magn. Reson.* **77**, 274 (1988).
47. S. P. RUCKER and A. J. SHAKA, *Mol. Phys* **68**, 509 (1988).
48. J. CAVANAGH, W. J. CHAZIN and M. RANCE, *J. Magn. Reson.* **72**, 540 (1990).
49. G. EICH, G. BODENHAUSEN and R. R. ERNST, *J. Am. Chem. Soc.* **104**, 3731 (1982).
50. A. BAX, *Methods Enzymol.* **176**, 151 (1989).
51. S. W. FESIK and E. R. P. ZUIDERWEG, *J. Magn. Reson.* **78**, 588 (1988).
52. D. MARION, L. E. KAY, S. W. SPARKS, D. A. TORCHIA and A. BAX, *J. Am. Chem. Soc.* **111**, 1515 (1989).
53. E. R. P. ZUIDERWEG and S. W. FESIK, *Biochemistry* **28**, 2387 (1989).
54. P. C. DRISCOLL, A. M. GRONENBORN, P. T. WINGFIELD and G. M. CLORE, *Biochemistry* **29**, 4668 (1990).
55. G. M. CLORE, A. BAX, P. T. WINGFIELD and A. M. GRONENBORN, *Biochemistry* **29**, 5671 (1990).
56. M. IKURA, A. BAX, G. M. CLORE and A. M. GRONENBORN, *J. Am. Chem. Soc.* **112**, 9020 (1990).
57. T. FRENKIEL, C. BAUER, M. D. CARR, B. BRIDSALL and J. FEENEY, *J. Magn. Reson.* **90**, 420 (1990).
58. A. A. BOTHNER-BY, R. L. STEPHENS, J. T. LEE, C. D. WARREN and R. W. JEANLOZ, *J. Am. Chem. Soc.* **106**, 811 (1984).
59. B. A. MESSERLE, G. WIDER, G. OTTING, C. WEBER and K. WÜTHRICH, *J. Magn. Reson.* **85**, 608 (1989).
60. G. OTTING and K. WÜTHRICH, *J. Am. Chem. Soc.* **111**, 1871 (1989).
61. A. A. BOTHNER-BY and J. DADOK, *J. Magn. Reson.* **72**, 540 (1987).
62. M. IKURA, L. E. KAY, R. TSCHUDIN, R. and A. BAX, *J. Magn. Reson.* **86**, 204 (1990).
63. E. R. P. ZUIDERWEG, L. P. MCINTOSH, F. W. DAHLQUIST and S. W. FESIK, *J. Magn. Reson.* **86**, 210 (1990).
64. A. BAX, V. SKLENAR and M. F. SUMMERS, *J. Magn. Reson.* **70**, 327 (1986).
65. C. J. BAUER, T. A. FRENKIEL and A. N. LANE, *J. Magn. Reson.* **87**, 144 (1990).
66. A. BAX and D. G. DAVIS, *J. Magn. Reson.* **63**, 207 (1985).
67. P. C. DRISCOLL, A. M. GRONENBORN, P. T. WINGFIELD and G. M. CLORE, *Biochemistry* **29**, 4668 (1990).
68. G. M. CLORE, P. C. DRISCOLL, P. T. WINGFIELD and A. M. GRONENBORN, *J. Mol. Biol.* **214**, 811 (1990).
69. G. M. CLORE, L. E. KAY, A. BAX and A. M. GRONENBORN, *Biochemistry* **30**, 12 (1991).
70. H. BARKHUIJEN, R. DE BEER, W. M. M. J. BOVEE and D. VAN ORMONDT, *J. Magn. Reson.* **61**, 465 (1985).

71. A. E. SCHUSSHEIM and D. COWBURN, *J. Magn. Reson.* **71**, 378 (1987).
72. L. E. KAY, M. IKURA, G. ZHU and A. BAX, *J. Magn. Reson.* **91**, 422 (1991).
73. E. T. OLEJNICZAK and H. L. EATON, *J. Magn. Reson.* **87**, 682 (1990).
74. W. H. PRESS, B. P. FLANNERY, S. A. TEUKOLSKY and W. T. VETTERLING, *Numerical Recipes in C: The Art of Scientific Computing*, p. 463, Cambridge University Press, Cambridge (1989).
75. G. ZHU and A. BAX, *J. Magn. Reson.* **90**, 405 (1990).
76. M. R. BENDALL, D. M. DODDRELL and D. T. PEGG, *J. Am. Chem. Soc.* **103**, 4603 (1981).
77. G. M. CLORE, P. T. WINGFIELD and A. M. GRONENBORN, *Biochemistry* **30**, 2315 (1991).
78. A. J. SHAKA, P. B. BARKER and R. FREEMAN, *J. Magn. Reson.* **64**, 547 (1985).
79. A. J. SHAKA, J. KEELER, T. FRENKIEL and R. FREEMAN, *J. Magn. Reson.* **52**, 335 (1983).